Contents

Chapter 6

The GlueX Detector in Hall D

6.1 Overview

The goal of the GLUEX experiment is to search for gluonic excitations with masses up to $2.5\ GeV/c^2$. The identification of such states requires knowledge about their production mechanism, the identification of their quantum numbers J^{PC} and their decay modes. The production mechanism and J^{PC} determination require a partial wave analysis which in turn depends on the kinematic identification of exclusive reactions. The decay products of produced mesons must be identified and measured with good resolution and with full acceptance in decay angles. In many cases the decays of mesons involve a chain of particle decays. The GLUEX detector (see Figure 6.1) must therefore be hermetic with 4π coverage and have the capability of measuring directions and energies of photons and momenta of charged particles with good resolution. Particle identification is also required.

The partial wave analysis technique depends on high statistics and in the case of incident photons, also requires linear polarization. The latter is needed to identify the production mechanism. The linear polarization is achieved by the coherent bremsstrahlung technique. The degree of linear polarization and flux of photons in the coherent peak fall dramatically as the photon energy approaches the endpoint energy. On the other hand, it is desirable to have photon energies high enough to produce the required masses with sufficient cross section and with sufficient forward boost for good acceptance. For a fixed incident momentum and a fixed resonance mass, it is also desirable to have a fairly constant $\mid t\mid_{min}$ over the natural width of the resonance. This also requires sufficiently high incident photon energy.

An operating photon energy $9.0\ GeV$ produced from a $12.0\ GeV$ electron beam represents an optimization of beam flux, cross–section and degree of polarization. The GLUEX detector is therefore optimized for this energy range. Figure 6.1 is a schematic representation of the proposed GLUEX detector. The individual subsystems are discussed in more detail below.

6.2 The Target

The main physics program for the GlueX experiment will be conducted with a low-power liquid hydrogen or liquid deuterium target. We propose a design which is very similar to the cryogenic target presently in use in Hall B. This target should fit comfortably into the detector geometry. Solid targets, required for various calibrations, can easily be incorporated into this design.

The maximum power deposited in the target by the beam is 100mW. In such low-power targets, natural convection is sufficient to remove heat from the target cell and a circulation pump is not required. These targets frequently employ mylar target cells. The mylar cell is often mounted on a metal base to provide for liquid entry ports and a reliable means of positioning the cell. The beam enters through a thin window mounted on a reentrant tube at the base of the cell. The diameter of this entrance window must be sufficiently large to allow
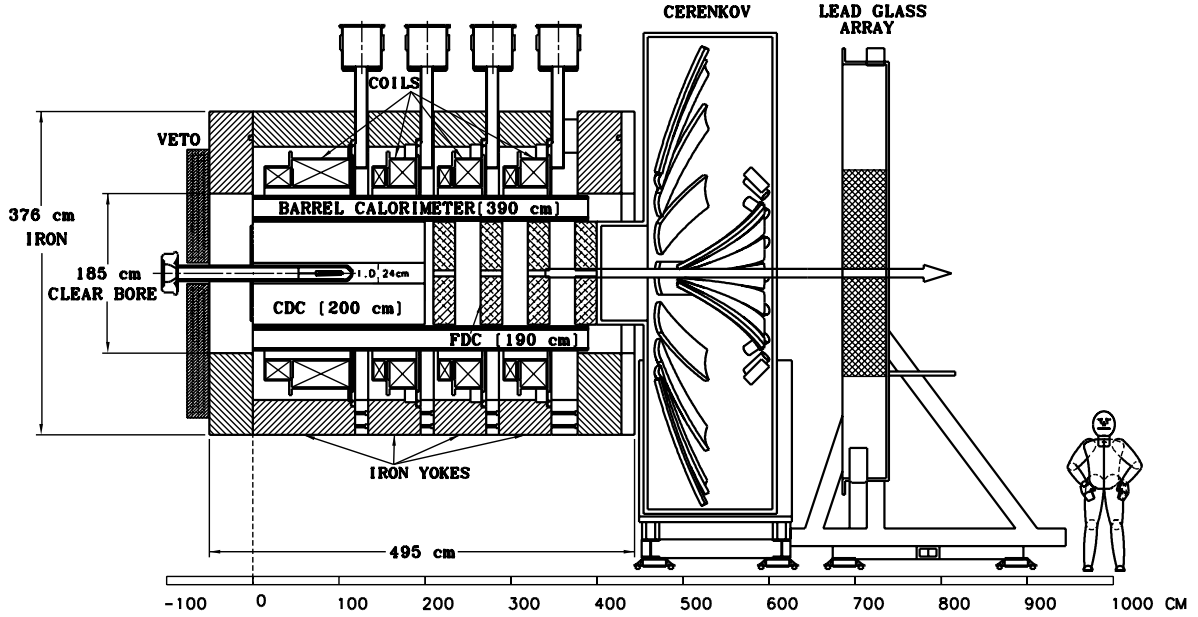
Figure 6.1: An overview of the GLUEX detector. The major subsystems are labeled and are discussed individually in the text.

the beam to enter the cell without scraping; taking into consideration the uncertainties that will be present in aligning the cell. The area between the reentrant window and the outer wall of the cell must be sufficiently large to allow for convection and to prevent bubbles from being trapped. A target cell diameter of three to six centimeters would seem reasonable. A smaller diameter cell would be possible with more stringent alignment requirements. A system such as this, containing a few hundred cm^3 of liquid hydrogen, would be considered "small" by Jefferson laboratory standards and the safety requirements would not place any significant constraints on the target design or operation.

The target cell is connected to a condenser located upstream of the cell. In the Hall B target the condenser is formed by concentric cylindrical shells with the axis of the cylinders lying along the beam line. The heat exchanger should be sized to allow the target to be condensed in a reasonable period of time (a few hours). In some target systems the condenser is cooled by a separate refrigerator. In other systems liquid helium at 4.5K is used as the refrigerant. Because the magnet in Hall D will require liquid helium there seems little reason to operate a separate refrigerator for the target. The standard CEBAF delivery system supplies 5K 3 atmosphere fluid through a 1-3/8" diameter bayonet. This gas is expanded through a JT valve to produce liquid. This system is somewhat cumbersome for small loads. It would be much more convenient to supply the target with low-pressure 4.5K liquid through a small transfer line. It would be possible to draw liquid from the magnet if a port is available. In Hall B it was found convenient to draw liquid helium for the target from a buffer dewar which is filled by a JT valve. To allow for a similar arrangement in Hall D, a 4.5K supply bayonet and a 5K cold return bayonet should be provided.

The extent to which target components shadow the veto counter must be considered. Some shadowing of the veto counter will be unavoidable, since the cell must be supported. As we are relying on convection to remove heat from the target cell it would be favorable to locate the heat exchanger as close to the target cell as possible. This would result in increased shadowing of the veto counter. It is not clear that convection alone would be sufficient if the condenser were located outside the veto detector. This design could easily be tested using the Hall B test cryostat.

The hydrogen cell is located inside of a scattering chamber to provide an isolation vacuum.
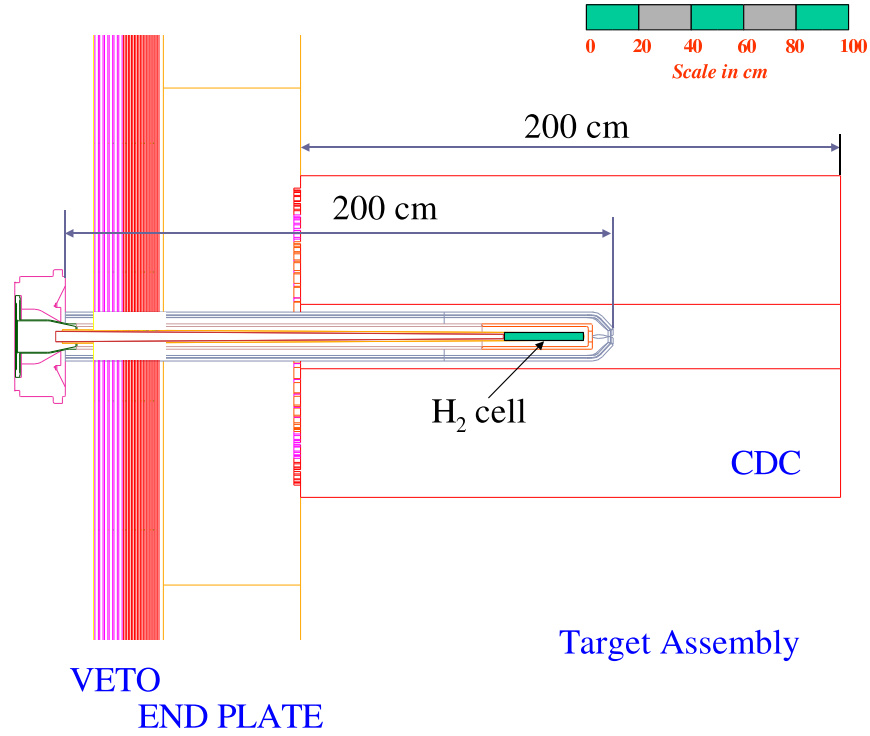
Figure 6.2: Target region including target cell, vacuum scattering chamber, start counter. Sufficient room exists for a vertex detector. Also shown for reference are the CDC and thickness of the magnet iron and upstream veto.

The walls of this chamber should be kept as thin as possible. In Hall B, plastic foam chambers have been used successfully. The target vacuum is likely to be shared with the upstream and downstream beam-lines. The target vacuum chamber would include a service port for the refrigerant, target gas and instrumentation connections.

Solid targets are required for purposes of calibration and studying detector response. It may be desirable to replace the target cell with a multi-foil "optics target" from time to time. Installing the target and bringing it into operation will probably require two days. A mechanism to introduce solid targets either upstream or downstream of the hydrogen cell would be possible. Consideration should be given to the number of different targets required and to their placement.

Attaching the vertex detector and veto counter to the target vacuum chamber will locate those detectors accurately with respect to the vacuum chamber, but may complicate target assembly and disassembly. The cool-down and vacuum motion of the target cell relative to the vacuum chamber will remain major sources of uncertainty in the target cell position. The alignment requirements for this are not severe but should be considered early in the design stage. It is likely that a rail system would be used to position the target inside the magnet, as the insertion cart is used to position the cryogenic target in Hall B. Figure 6.2 illustrates a target cell similar to one which has been used in Hall B positioned inside the GlueX detector. In this design the cell incorporates an extended reentrant window to place all metallic components upstream of the veto detector.

6.3   Calorimetry

6.3.1   Global Design

The electromagnetic (EM) calorimetry for the GLUEX experiment is divided in three parts, each handled by a different detector sub-system.

The very forward angles ($\theta < 14°$) of the HALL D detector will be covered by an existing lead glass detector (LGD) used in the E852 experiment at BNL and re-stacked to meet the geometrical acceptance criteria for HALL D. The approximate polar angular range $14° < \theta < 138°$ will be subtended by the barrel calorimeter. Finally, the upsteam, large-polar angle region ($\theta > 138°$) will be the domain of the upsteam photon veto.

Each of these three sub-systems is treated individually in a dedicated subsection within this chapter.

6.3.2   The Lead-Glass Calorimeter

The most downstream subsystem of the GLUEX experiment is the lead glass detector (LGD), an electromagnetic calorimeter consisting of nearly 2500 lead glass blocks. The purpose of the LGD is to detect and measure forward-going photons from the decays of π^0, η and other mesons. The LGD will also provide a fast energy sum to be used in the level-1 trigger.

Each block has dimensions of $4 \times 4 \times 45$ cm^3 and they are arranged in a nearly circular stack. The radius (≈ 1 m) is matched to the aperture of the GLUEX solenoid magnet. The type of glass used in E852 and RADPHI and proposed for use in GLUEX was produced in Russia and is called type F8-00. Its chemical composition is 45% PbO, 42.8% SiO$_2$, 10.4% K$_2$O and 1.8% Na$_2$O. This glass has an index of refraction of 1.62, a density of 3.6 gm/cm^3, a radiation length of 3.1 cm and a nuclear collision length of 22.5 cm. The blocks were machined to a precision of about 25 microns in transverse dimensions and flatness so stacking the array does not result in gaps. The Cerenkov light from each block is viewed by a FEU-84-3 Russian PMT. The PMT bases are of a Cockcroft-Walton (CW) design [1]. The PMT's will be registered with respect to the glass using a cellular wall that includes soft-iron and μ-metal shielding. The signal from each block will be digitized with an 8-bit 250 MHz FADC. A schematic of the calorimeter is shown in Figure 6.3.

Several of the GLUEX collaborating institutions have been involved in the design, construction and operation of calorimeters of a design similar to that presented here and in the analyses of data from those calorimeters. The first of these calorimeters was a 3000-block calorimeter used in the E852 experiment at Brookhaven Lab (BNL) which used an 18 GeV/c π^- beam and the multiparticle spectrometer (MPS). Details of the design and operation of prototype calorimeters and the one used in E852 have been published [2, 3]. Several physics results based on measurements with the E852 LGD will be discussed here.

An LGD was also used in the RADPHI experiment [4, 5] at JLab that was located downstream of the CLAS detector in HALL B and used in a bremsstrahlung photon beam produced with 5.4 GeV electrons. The goal of RADPHI was a measurement of the radiative decay modes of the ϕ meson resulting in five-photon final states. The experience gained with the RADPHI LGD is extremely valuable for GLUEX. As will be discussed below, the π^0 and η mass resolutions based on measurements from the LGD improve as the distance from the production point of photons (the target) to the LGD increases. The resolutions also improve as the mean photon energy increases and thus as the beam energy increases. Photons produced in RADPHI resulted from interactions of beam photons of energies distributed almost uniformly in the range from 3 to 5.4 GeV and the target to LGD distance was ≈ 1 m. For GLUEX the photon energy is 9 GeV and the target to LGD distance is ≈ 5 m.

Based on the experience with the LGD's used in E852 and RADPHI we expect the GLUEX LGD to provide the granularity and resolution required to carry out the amplitude analysis needed to map the spectrum of gluonic excitations, the goal of this experiment.

In what follows we also address several technical issues regarding the GLUEX LGD including issues of the assessment of the E852 and RADPHI glass and PMT's that will be used in GLUEX,

curing of radiation-damaged glass, electromagnetic backgrounds in the beam region, shielding PMT's from the fringe field of the solenoid, calibration and monitoring.
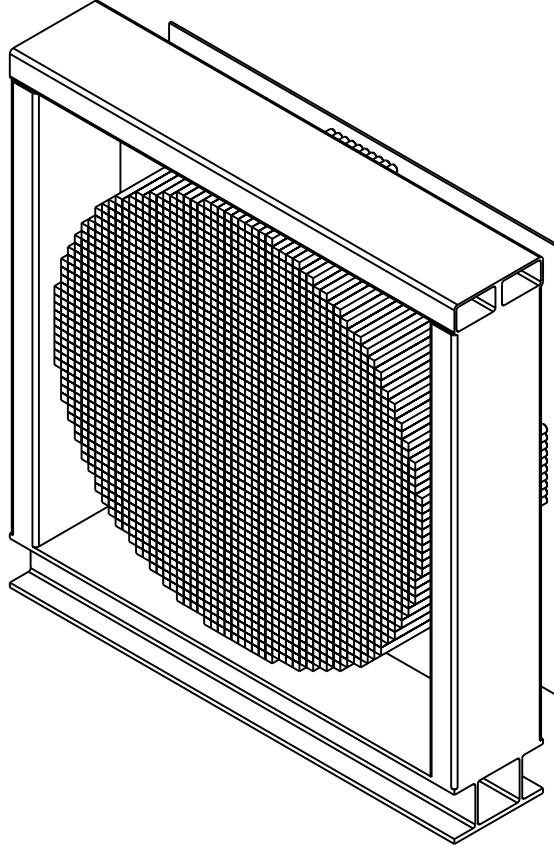

Figure 6.3: The lead glass detector as modified for GlueX . 2500 lead glass blocks will be arranged in a nearly circular stack of radius ≈ 1 m.

The E852 Experience

The goal of E852 was a search for mesons with unusual quantum numbers using the MPS at BNL with a Lead-Glass Calorimeter. The E852 LGD was located 5.4 m from a liquid H_2 target located mid-way inside a large dipole spectrometer magnet. E852 detected and measured both charged particles as well as photons from π^0 and η mesons. The measured mass resolution for π^0 and η mesons was 10 and 25 MeV/c^2 respectively.

Several physics results from amplitude analyses based solely on data from the LGD have been published. Events in which four photons were identified in the all-neutral final state $4\gamma n$ led to and analyses of the $\pi^0\pi^0$ [6, 7] and $\pi^0\eta$ systems [8, 9, 10]. Figure 6.4 shows a scatterplot of one $\gamma\gamma$ effective mass combination versus the other $\gamma\gamma$ effective mass from the reaction $\pi^- p \to 4\gamma n$. Clusters associated with the $\pi^0\pi^0 n$ and $\pi^0\eta n$ final states are clearly observed.

The $\pi^0\pi^0$ effective mass spectrum for the $\pi^- p \to \pi^0\pi^0 n$ reaction is shown in Figure 6.5. The prominent feature in this spectrum is the $f_2(1275)$ tensor meson. The spectrum also shows a sharp dip at ≈ 1 GeV/c^2 that is understood as evidence for the scalar meson $f_0(980)$ interfering with the S-wave background. A partial wave analysis (PWA) of these data set was performed [6, 7] for events in various ranges in momentum transferred from the target proton to the recoil neutron and some of the results for the lowest momentum transfer range are shown in Figure 6.6. Plots show open and filled circles corresponding to mathematically ambiguous solutions with the filled circles indicating the physical solutions based on other criteria. The S-wave shows
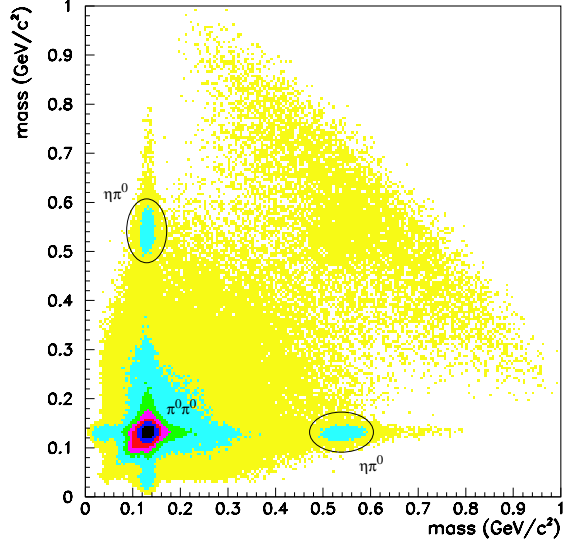
Figure 6.4: Scatterplot of one $\gamma\gamma$ effective mass combination versus the other $\gamma\gamma$ effective mass from the reaction $\pi^- p \rightarrow 4\gamma n$. These measurements were made using the E852 LGD.
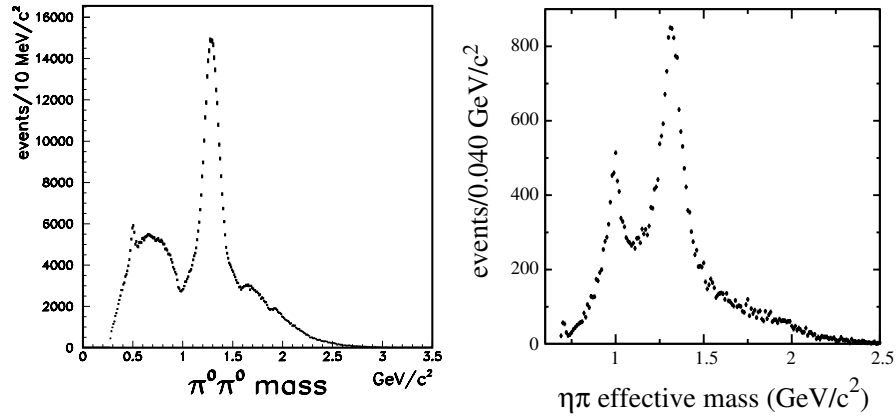

Figure 6.5: left: Distribution of the $\pi^0\pi^0$ effective mass in the E852 reaction $\pi^- p \rightarrow \pi^0\pi^0 n$. right: Distribution of the $\eta\pi^0$ effective mass in the E852 reaction $\pi^- p \rightarrow \eta\pi^0 n$.

evidence for the $f_0(980)$ scalar meson via its interference with a broad background, the D_0-wave shows the $f_2(1275)$ and the phase difference between the S-wave and D_0-waves show the classic motion expected of a resonance.

Figure 6.5 also shows the $\eta\pi^0$ effective mass spectrum for the $\pi^- p \rightarrow \eta\pi^0 n$ reaction. This spectrum features both the scalar $a_0(980)$ and the tensor $a_2(1320)$. A partial wave analysis of this system has also been performed [8, 9, 10].

Figure 6.7 shows the $\eta\pi^+\pi^-$ and $\eta\pi^0\pi^0$ effective mass distributions where well known meson states are clearly observed. The $\eta\pi^0\pi^0$ system requires the reconstruction of six-photons in the LGD. Other analyses involving photons and charged particles have also been published including a study of the $a_0(980)$ in the $\eta\pi^+\pi^-$ and $\eta\pi^0$ spectra [11] and a partial wave analyses of the $\eta\pi^+\pi^-$ [12], $\omega\eta$ [13], $\omega\pi^-$ [14] and $\eta\pi^+\pi^-\pi^-$ [15] systems.

The Radphi Experience

The RADPHI detector is shown schematically in Fig. 6.8. This detector was operated downstream of the CLAS detector in HALL B. The beam was incident on a 2.66-cm diameter, 2.54-cm long
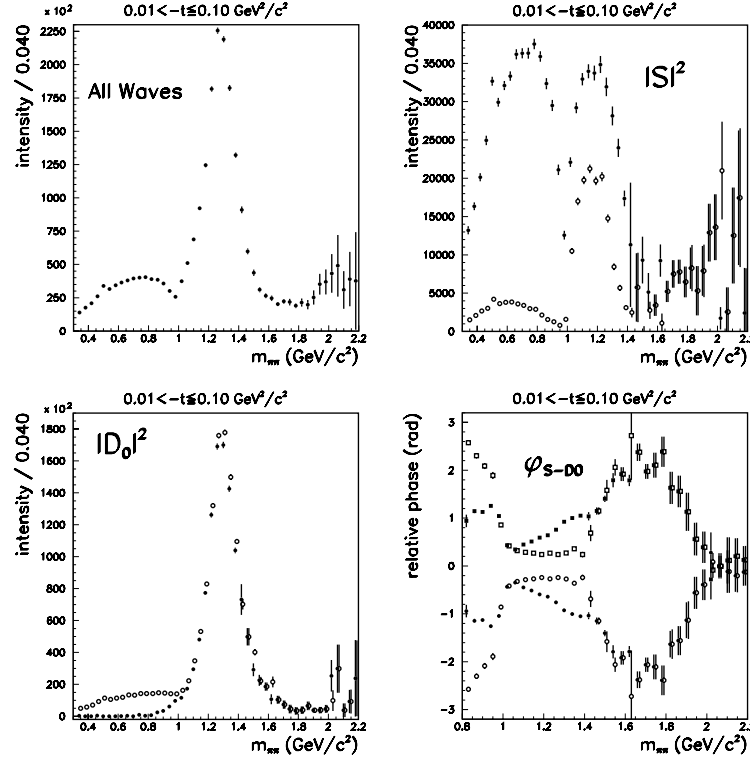
Figure 6.6: Results of a partial wave analysis of the $\pi^0\pi^0$ system in the E852 reaction $\pi^- p \to \pi^0\pi^0 n$ for low momentum transfer events. The sum of all waves (upper left), the S-wave (upper right), the D_0-wave (lower left) and the phase between the S-wave and D_0-wave (lower right) are shown. Plots show open and filled circles corresponding to mathematically ambiguous solutions with the filled circles indicating the physical solutions based on other criteria.
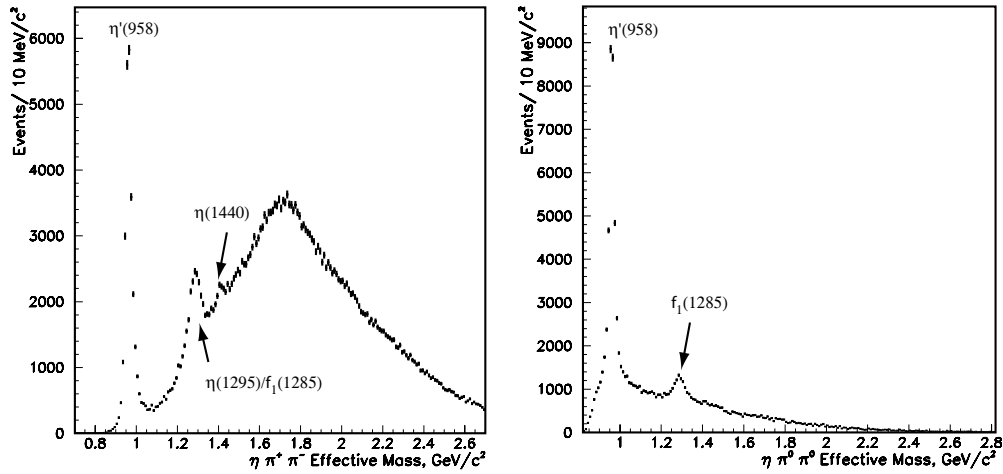
Figure 6.7: left: Distribution of the $\eta\pi^+\pi^-$ and right: $\eta\pi^0\pi^0$ mass distributions observed in E852.

beryllium target. Surrounding the target and extending forward to 30° from the beam axis was a cylindrical scintillator detector (BSD) which provided nearly full angular coverage for recoil protons. Surrounding the BSD was a cylindrical lead-scintillating fiber photon detector (BGD) which served to reject events (off-line) with large angle photons. The primary detector

component was a 620-channel lead-glass wall (LGD) assembled to approximate a circle around the beam line with a $8 \times 8 \text{cm}^2$ central hole for the passage of the beam. The lead-glass detector was positioned 1.07 m downstream of the target and subtended an angle of approximately 27° from the beam line.

The RADPHI experiment provides an opportunity to understand the operation of a lead glass calorimeter in a bremsstrahlung photon beam. Two important issues are understanding the energy and spatial resolution of the detector (relevant for the reconstruction of π^0 and η mesons) and electromagnetic backgrounds.

Lacking a source of electron or photon showers of a well-defined energy, the RADPHI experiment had to rely on the observed width of known mesons to deduce the energy resolution of the lead-glass calorimeter. The observed width of narrow mesons such as the π^0 and η that undergo 2γ decay is determined by the single-shower energy and position resolutions of the LGD. In cases where the spatial contribution can be neglected, the single shower energy resolution was extracted by selecting pairs with one of the two showers in a narrow energy window and examining the energy spectrum of the other, for a given cluster-separation angle. This energy spectrum shows peaks that correspond to the masses of the π^0 and η and whose line-shapes are convolutions of the energy response functions for the two showers plus contributions from uncertainties on the shower centroid positions. The contribution from spatial resolution to the width of the peaks was minimized by focusing first on the η, which is associated with pairs of showers that are well separated on the face of the calorimeter. By analyzing the dependence of the peak width on the energies of the individual showers, the convolution was inverted to obtain the r.m.s. resolution for single showers as a function of shower energy without introducing a model for the energy dependence. Once the energy resolution had been determined in this way, the spatial resolution was then examined by looking at the excess width of the π^0 peak over what was expected based upon energy resolution alone. In the end, a unified analysis including both energy and spatial resolution effects was able to reproduce both the π^0 and η profiles.

Assuming that the spatial resolution is not important for $\eta \to 2\gamma$ decays, the r.m.s. shower energy resolution can be extracted without assuming any functional form for its dependence on shower energy. This model-independent solution was then compared with the standard parametrization [16] of the lead glass energy resolution given in Eq. 6.1.

$$\frac{\sigma_E}{E} = \frac{B}{\sqrt{E}} + A. \tag{6.1}$$

The first term on the right contains the effects of photoelectron statistics, while the second term wraps up all of the systematic block-to-block differences and calibration errors which prevent the width of the response function from collapsing to a delta function in the high-energy limit. In order to describe the π^0 peak with the same parameters it is necessary to introduce a model for the shower spatial resolution, which itself depends upon shower energy. The energy dependence is proportional to $1/\sqrt{E}$ with a proportionality constant that depends on the size of the LGD block [17]. Eq. 6.2 is adopted for showers at normal incidence, with the constant C expected to be around 7 mm·GeV$^{-\frac{1}{2}}$.

$$\sigma_x = \frac{C}{\sqrt{E}}. \tag{6.2}$$

In the RADPHI geometry many of the showers are far from normal incidence and so the shower depth fluctuations of roughly one radiation length also contribute to the centroid position resolution along one of the spatial axes. This was taken into account in the analysis by projecting one radiation length from along the shower axis onto the transverse plane and adding it in quadrature to the base term in Eq. 6.2. The final values for all parameters were determined by simultaneous analysis of the η and π^0 data where all of the above effects are included for both.

Estimating the GlueX π^0 and η Mass Resolutions

The experience with the E852 and RADPHI detectors allows us to reasonably interpolate to expected GLUEX performance. Based on the discussion above and that of reference [18] we
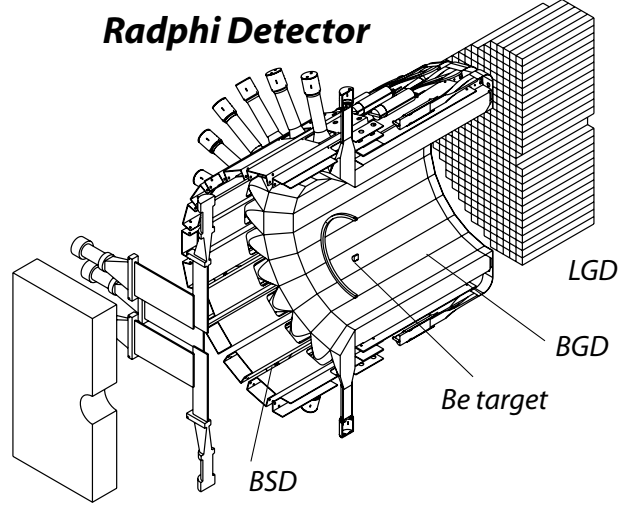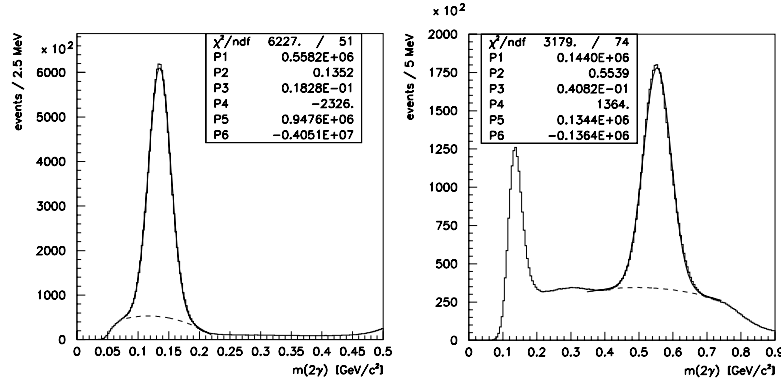
Figure 6.8: The RADPHI detector.

Figure 6.9: Invariant mass distribution of $\pi^0 \to 2\gamma$ (left) and $\eta \to 2\gamma$ (right). The parameters shown are the height (P1), mean (P2) and sigma (P3) of the Gaussian peak fitted to the data over a polynomial background described by parameters P4-P6.

assume the energy resolution given by:

$$\frac{\sigma_E}{E} = 0.036 + \frac{0.073}{\sqrt{E}} \qquad (6.3)$$

and the spatial resolution is given by:

$$\sigma_\rho = \sqrt{\left(\frac{7.1}{\sqrt{E}}\right)^2 + (X_0 \sin\theta)^2} \ mm \qquad (6.4)$$

where ρ locates the shower position in the plane of the LGD measured from the center of the LGD, θ is measured from the normal to the LGD plane, X_0 is the radiation length of glass (31 mm in this case) and E is the photon energy in GeV.

A Monte Carlo simulation of forward π^0 and η production for RADPHI, E852 and GLUEX assumed:

1. A uniform photon beam between 3.0 and 5.4 GeV for RADPHI, 18.0 GeV for E852 and 9 GeV for GlueX;

2. A target to LGD distance of 1.0 m, 5.4 m and 5.0 m for the three experiments respectively.
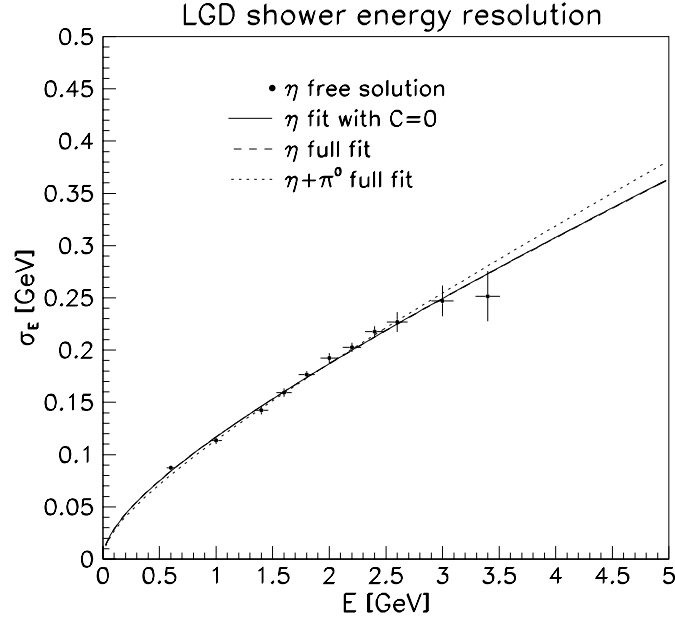
Figure 6.10: Energy resolution of showers in the LGD obtained from analysis of the 2γ sample.

3. Transverse LGD dimensions characterized by circular stacks of radii 0.5 m for RADPHI and 1.0 m for GLUEX and a 1.68 by 2.8 m rectangular stack for E852.

4. A minimum photon energy of 150 MeV and a minimum photon separation of 8 cm.

Simulation results are shown in the plots of Figure 6.11. We obtain π^0 mass resolutions of 16 MeV for RADPHI and 8 MeV for E852 compared to measured resolutions of 18 and 10 MeV. For GLUEX we predict 9 MeV. For the η we obtain mass resolutions of 40 MeV for RADPHI and 27 MeV for E852 compared to measured resolutions of 40 and 25 MeV. For GLUEX we predict 30 MeV.

Electromagnetic Backgrounds

The experience with the RADPHI LGD also allows us to compare estimates of electromagnetic backgrounds as calculated using GEANT with measured rates. Such a comparison is shown in Figure 6.12. The histogram in the figure is the Monte Carlo estimate for the LGD rates arising only from electromagnetic background. Note that for individual blocks, the expected hadronic rate is negligible on this scale. The simulation includes the principal components of the Hall B photon beam line starting at the radiator and including the (empty) CLAS target and downstream yoke aperture. Note that in Figure 6.12 a marked depression appears at small radius, relative to the observed rates. These blocks are in the vicinity of the beam hole and, in addition to suffering from the highest rates, these blocks also suffered from radiation damage. The eight blocks closest to the beam axis (first data point) are the most affected, but some effects can be seen at neighboring points.

Radiation Damage

Online monitoring of the LGD during the RADPHI experiment indicated that the 8 blocks immediately adjacent to the beam hole were becoming progressively reduced in gain as the run progressed. This observation was based upon the laser monitor system, the raw pulse-height distributions, and the channel gains which were periodically recalibrated during the run. A similar effect was seen, but to a lesser degree, for the next layer of blocks once removed from the beam
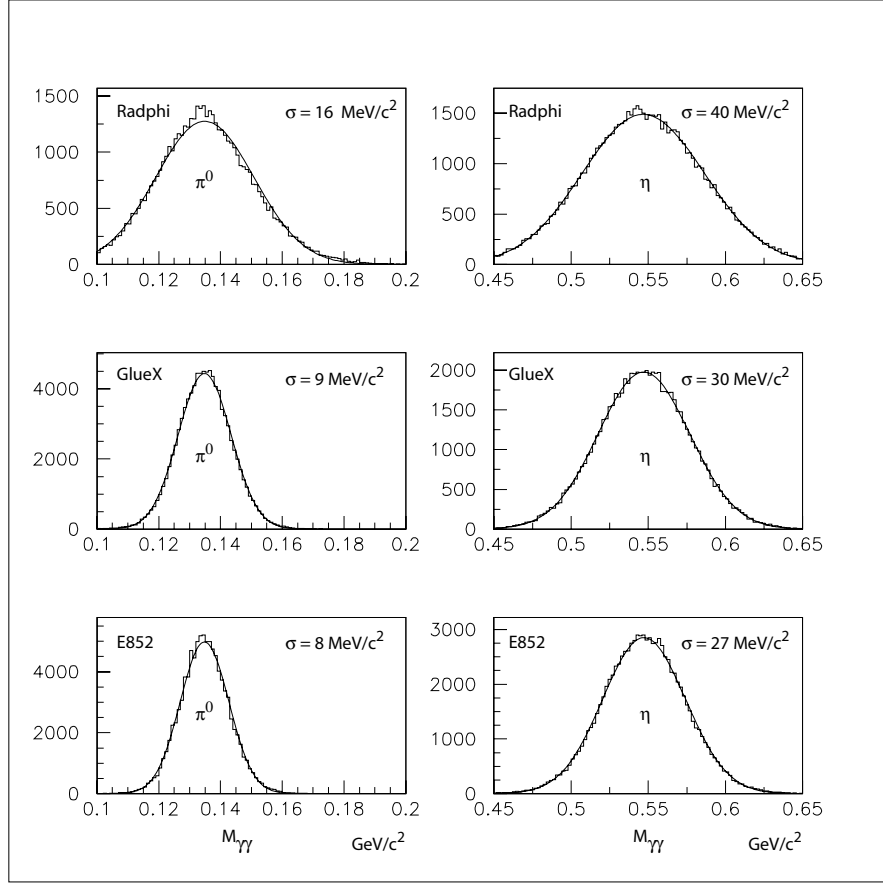
Figure 6.11: Simulated diphoton mass for the π^0 and η using the Radphi, GlueX and E8652 geometry.

hole. During a pause in the experiment, visual inspection of the blocks indicated that the glass was darkening, a well-known effect of radiation damage on lead glass. Figure 6.13 illustrates the gain reduction with beam time (roughly proportional to integrated radiation dose) for a typical block adjacent to the beam hole. It is apparent that the gain change is a gradual, cumulative effect rather than a sudden change which might be characteristic of a beam mis-steering event.

The magnitude of the gain loss (order 40%) was such that it could be compensated by adjustments of the PMT high voltages. This was done periodically during the experiment. The last datum in Figure 6.13 shows the result of one adjustment. However, this is only a partial solution, since the module suffers a loss of photoelectrons due to the radiation damage, and thus a degraded resolution. Thus it was desirable to 'heal' the radiation damage as much as possible.

Radiation damage in lead glass is known to be temporary, and to largely heal itself on the time scale of a few months. The healing can be accelerated by the use of ultraviolet (UV) light. This approach was adopted for the most affected blocks. During an extended down-time in the run, the PMT and base for selected modules were removed and a UV light guide attached to a quartz envelope Mercury vapor lamp was inserted. The output of the lamp was 5 W/cm^2 in the range 300 to 480 nm, with a peak intensity at 365 nm. The affected blocks were each illuminated for periods of 6-8 hours. These blocks showed a gain increase of 30% following this treatment, nearly recovering their initial gains.

It should be noted that the change in the response of the modules due to radiation damage and the gain recovery following UV treatment was even more dramatic in the data from the laser monitoring system (typically a factor of two change). The difference between the shift in the pulser response and that seen in the gain constants from the calibration can be qualitatively
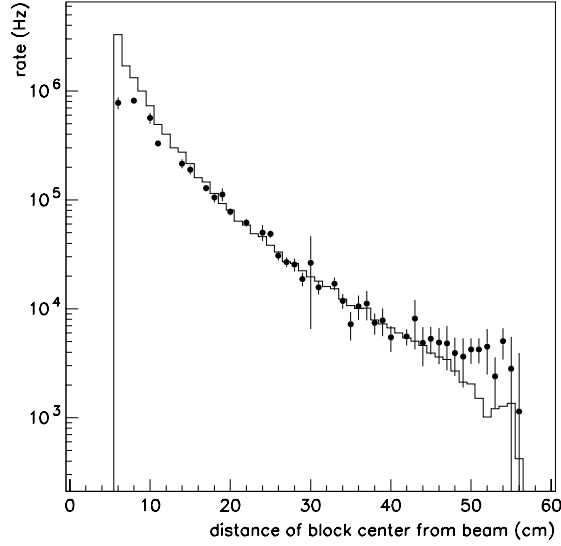
Figure 6.12: Characteristics of unbiased flux observed in individual blocks in the LGD as a function of distance from the beam. The points are derived from data and the histograms from a Monte Carlo simulation of the electromagnetic background coming from the beam and target. All hits over 15 MeV are recorded.

understood by noting that the laser illuminates the front of the block and thus measures the transmission of the entire block, while the showers seen in the calibration data create Cerenkov light throughout the volume of the block, and are therefore less sensitive to attenuation effects in the upstream region of the block. The radiation damage is now known, from measurements, to be within 11 *cm* of the front surface of the detector, and this was confirmed by visual inspection, in qualitative agreement with the difference between the laser monitor data and the calibration data.

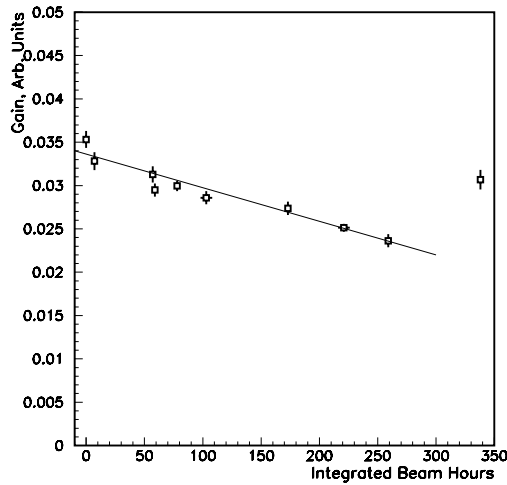Figure 6.13: The effect of radiation damage on the central part of the detector. The last point shows the gain after an adjustment of the PMT high voltage.

Heat Curing of Damaged Blocks   As part of the program to assess the glass used in E852 and RADPHI for use in GLUEX a spectrophotometer (Shimadzu UV-160) was modified to allow a lead glass bar to be automatically moved along its long axis to measure transmission through

the 4 cm thickness. Based on the transmission dependence on wavelength, the transmission of the bar as a function of length was measured at 410 nm. Figure 6.14 shows the dependence of transmission as a function of length along the block for a block that visibly shows radiation damage. An alternative to UV curing, heating blocks in an oven has also been studied. The plot also shows the transmission curve for the same block after heating the block for several hours in an oven at 260 °C.
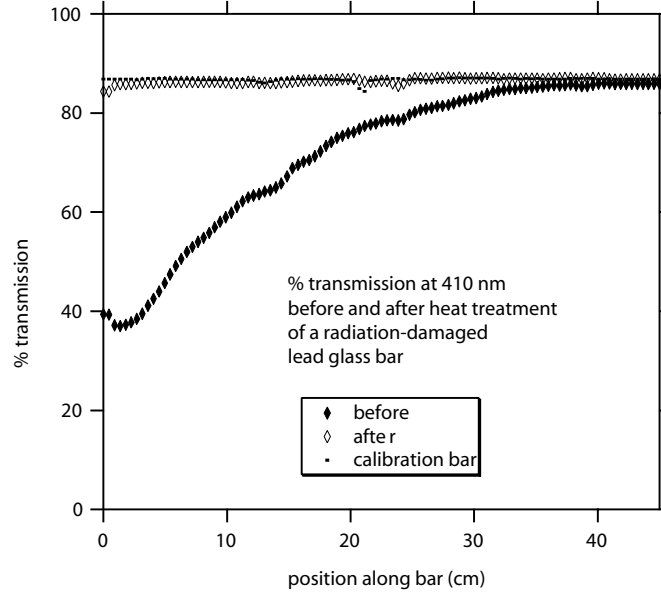

Figure 6.14: The effect of heat curing.

Assessing Lead Glass Blocks and PMT's

Lead glass block evaluation   Some of the lead glass blocks used in the E852 experiment were used in the RADPHI experiment. All of the blocks are being examined for mechanical and radiation damage – the latter bring assessed using the spectrophotometer described above.

The transmission at a wavelength of 410 nm as a function of length along the block will be measured and recorded for each block. The reason for measuring the transmission at this wavelength can be understood from the data presented in FIgure 6.15 where the transmission as a function of wavelength is measured for a block that suffered radiation damage and a block with no damage. The measurement was made approximately 2.5 cm from the upstream end of block where *upstream* refers to the orientation of the damaged block in the beam. At about 410 nm the undamaged glass reaches a transmission plateau.

PMT Evaluation   The PMT's available for GLUEX were used in E852 starting in 1994. There is some concern about the aging of the PMT's so a program of testing the 3200 PMT's (including spares) has already started. A similar process was used prior to constructing the E852 LGD for rating PMT's and is described in reference [2]. For the current test a light-tight box will accommodate 25 PMT's at a time. The tubes will view a diffusing plate that is illuminated by two blues LED's than will be pulsed. Under computer control the gain as a function of high-voltage will be recorded and random noise and correlated noise rate will be measured. The correlated noise rate will be measured within a fixed gate delayed by a few hundred nanoseconds after the LED's are pulsed. Preliminary measurements with a random selection of PMT's indicate that the PMT's performance has not degraded.
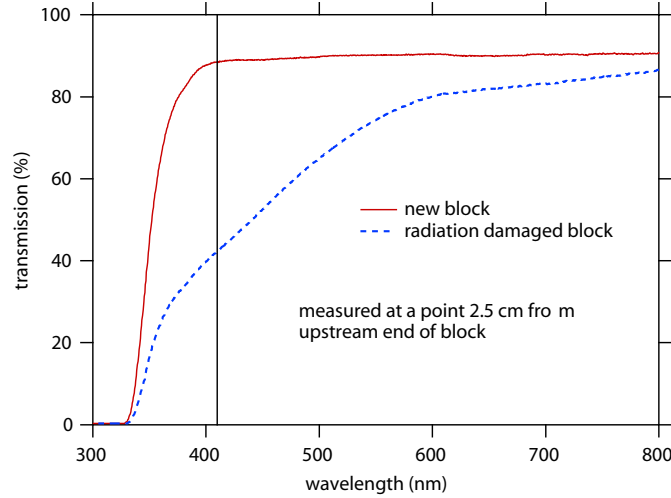
Figure 6.15: Transmission as a function of wavelength for radiation-damaged lead glass and undamaged glass. At about 410 nm the undamaged glass reaches a transmission plateau.

Other Issues

Electromagnetic Rates in the LGD   The RADPHI experience has forced us to deal with the issue of high rates in the central part of the detector and also how to use GEANT to estimate those rates. Those studies are currently underway for the GLUEX arrangement. We are also exploring the option of using another medium in the central region of the LGD, such a radiation hard lead glass, lead tungstate or another material. This will of course impact on shower reconstruction – especially for those showers that cross the boundary between media. Another option under investigation is to place a thin sheet of lead in front of the LGD blocks in danger of damage. The impact this has on resolution is also being studied.

Magnetic Shielding   In E852 a cellular wall was used to register the PMT's to the glass wall. That cellular wall consisted of two aluminum plates with holes into which cylindrical soft iron tubes were squeezed (the tubes were sandwiched between the plates). Epoxy was injected the space between the tubes and between the plates through small holes in the plates. Additional μ-metal shields surrounded individual PMT's before insertion into the soft iron tubes. The PMT's were positioned against the glass blocks with an air gap in between. This entire cellular wall structure was surrounded by a thick iron frame to provide further shielding. The structure is described in reference [3]. A similar wall was used for RADPHI. In E852 the PMT's were shielded from the fringe field of the BNL MPS dipole magnet.

Simulations of the fringe field of the GLUEX solenoid are currently underway for various assumptions about the structure and material in the vicinity of the LGD. More details about magnetic shielding are also discussed in the section on the TOF – the forward time-of-flight system.

For the LGD we plan to have the PMT photocathode recessed inside the iron shielding tube by about the diameter of the photocathode and we plan to study the use of short cylindrical glass segments to couple the lead glass to the PMT with proper index of refraction matching.

Monitoring   The E852 and RADPHI LGD's were monitored [3, 4] by using light from a nitrogen laser illuminating a block of scintillator. The scintillator light was transported by several optical fibers coupled to the sides of a Plexiglass sheet large enough to cover the front face of the glass stack. This system was used for initial gain setting and to monitor gains throughout the run.

Calibration GLUEX will base its LGD calibration system on the extensive experience gained with calibrating the E852 and RADPHI LGD's that is described in references [3] and [4].

Triggering An energy sum trigger was provided by the E852 and RADPHI LGD's [3, 4]. In addition the E852 LGD had a trigger processor that provided an estimate of the total effective mass of photons striking the LGD and this was used in the trigger.

6.3.3 Barrel Calorimetry

The barrel calorimeter (BCAL) will be positioned immediately inside the solenoid, which constrains the outer radius to be 90 cm and results in an outer surface area of approximately 23 m^2. This leaves a 2.7 cm space radially for supports and installation. This device is a key component of a hermetic system, and is crucial for both fully reconstructing all the photons in many physics reactions and providing accurate time-of-flight measurements for charged particles. In addition, it may be possible to get some dE information on charged particles as well. The large size of this device implies that it will be a challenge to build and instrument it at reasonable cost. The main parameters of the BCAL are given in Table 6.1.

A principle goal of GLUEX calorimetry is to detect and to measure photons from the decays of π^0's and η's which, in turn, can come from the decays of produced mesons or possibly from excited baryons (N^* or Δ). The positions and energies of the photons must be determined to sufficient accuracy to allow for a complete kinematic reconstruction of the event. Detailed Monte Carlo studies [19] [20] indicate that the BCAL should be sensitive down to as close to 20 MeV as possible and up to a few GeV in energy. The BCAL is also required to provide timing information for charged particles. The BCAL, in conjunction with dE/dx measurements in the CDC, will be the primary PID device for most of the protons detected in GLUEX. Monte Carlo studies [21] [22] show that in order to carry out this function, the BCAL needs to have close to 200 ps timing resolution. For events with only charged particles, it is essential to be able to veto on neutral missing energy. Here, nearly hermetic coverage is critical. For selected triggers, neutral energy requirements (or vetoes) are relatively easy to implement. A secondary function for this device is to be able to provide dE information to further aid the central tracking system in particle identification.

Table 6.1: Main parameters of the Barrel Calorimeter.

Parameter	Size
Length	390 cm
Inner radius	65 cm
Outer radius	90 cm
Fiber diameter	1 mm
Lead Sheet thickness	0.5 mm
Number of Fibers	1,000,000
Number of Readout Channels	~1000-5000
Weight	35 metric tons

Design Considerations

For the tracking elements inside the magnet to perform optimally, the BCAL must be thin, no more than 25 cm. This and the 4.5 m length of the solenoid lead to a long, narrow, tube-like design. In this geometry, readout is easiest at the ends where space exists. The choice of readout device must bear in mind the considerable magnetic field (22.4 kG) inside the bore and the rapidly varying fringe field at the ends. Conventional photo-multiplier tubes (PMTs) will work only outside of the solenoid and even there considerable attention must be paid to shielding.

While the collaboration initially looked at several potential designs, it was quickly realized that the only viable, cost-effective solution is one which utilizes scintillating fibers embedded in a lead matrix. The Pb/SciFi is used to make a relatively high–resolution sampling calorimeter. This solution is based on proven technology from other experiments.

Unfortunately, the very strong magnetic field in the immediate vicinity of the SciFi ends make the options for readout less clear. We initially looked at hybrid PMT (HPMT) which have been developed for CERN applications.These devices are immune to magnetic fields up to 2 T and their power supplies are very compact due to the fact that they draw virtually no current even under maximum bias. The HPMT's have a fast rise time of 6 ns or less, very good energy resolution, modest timing resolution, but low gain and as such require amplification. An additional drawback is their high cost. After careful study [23], these were rejected as an option because no suitable circuit could be devised to provide adequate pulse amplification and good timing simultaneously.

The option that is currently under investigation involves Silicon photo–multipliers (SIPM's). These devices offer gain and timing resolution comparable to that of a PMT, superior energy resolution, require a simple electronic circuit and are not sensitive to magnetic fields. These are discussed later in this report.

A more conventional option is to use magnetic field resistant PMTs coupled to fiber optic light guides to place the PMTs in regions of reduced field and with an appropriate orientation to further minimize signal loss. This option has the drawback that there is a loss of light associated with the long (probably fiber) light guides, as well as an increased mechanical complexity due to their placement. While this option would certainly work, it is being reserved as a backup.

Pb/SciFi Barrel Calorimeter

Scintillating fibers embedded in a matrix of lead (Pb/SciFi) or other high-Z materials have been used in calorimeter design and operation for more than a decade. The ratio of the active scintillator to the passive high-Z material, as well as the diameter of the fibers, can be tuned to enhance resolution, to determine the radiation length, and to achieve uniformity in the electromagnetic to hadronic response (the e/h ratio).

For high-resolution EM performance, the Jetset detector used such a calorimeter which was developed at Illinois [24]. This was the first detector designed specifically to optimize EM resolution. The recipe produced a detector comparable to lead glass at a considerably lower cost and with approximately half the radiation length. It utilized 1 mm fibers spaced uniformly (close packed) on specially grooved plates of lead. The lead was alloyed with $3 - 6\%$ antimony to provide mechanical stiffness.

Of more relevance to the GLUEX experiment is the calorimeter built for the KLOE experiment at DAΦNE. The KLOE collaboration has taken the development of Pb/SciFi a step further than JetSet. They developed better tooling for the production of long grooved plates, have pushed the technology for excellent fibers with long attenuation lengths [25] and have built a device with larger radius than needed in GLUEX and 4.3 m in length. This device is currently operating and results on its actual performance are available. Like Jetset, the KLOE design utilizes 1 mm diameter scintillating fibers embedded in a lead matrix with a fiber to lead to glue ratio of approximately $48 : 42 : 10$.

Both the JetSet and the KLOE calorimeter exhibit similar energy resolutions. An array of JetSet prototypes subjected to electrons in the range $0.3 - 1.5$ GeV was represented by the function

$$\sigma/E = 6.3\%/\sqrt{E}$$

with E in GeV. The constant term was negligible. In the Jetset Forward Calorimeter, the beam entered nearly parallel to the fiber direction. The energy resolution was also measured with tagged photons below 0.1 GeV and improved to $\approx 5\%/\sqrt{E}$; the detector gave a resolvable signal all the way down to 0.02 GeV. A KLOE prototype modules, 2 m in length was produced with conventional PMT readout at both ends. Such readout was possible due to the lower field

and more favorable field gradient of KLOE compared to GLUEX. An excellent energy resolution parametrization of

$$\sigma/E \approx 4.4\%/\sqrt{E}$$

was extracted. The final energy resolution for KLOE [26] was

$$\frac{\sigma(E)}{E} = \frac{5.4\%}{\sqrt{E(\text{GeV})}} + 0.7\%,$$

and this number serves as a benchmark for the GLUEX Barrel Calorimeter.

Because of the $\sim 4\ m$ module length in KLOE, special efforts needed to be made to develop and test scintillating fibers with very long attenuation lengths. Tested fibers had attenuation lengths in the range from $2.3 < \lambda < 3.2\ m$ which is far superior to the average λ of $1\ m$ for the JetSet fibers. This aspect of the design is critical because there exists a significant coupling between the position of impact (essentially the polar angle, θ) and the interpreted energy. Light collected at each end must be corrected for attenuation length before conversion to energy units.

Another important feature of scintillating fibers is the signal rise time and overall duration. Because fast plastic scintillator is used (Decay times are 2.0–2.5 ns), integrated signal time can be kept below 100 ns, with shorter times possible if deemed necessary for rate considerations. No problems are anticipated at the expected maximum luminosity of GLUEX. With rise times of a few ns, excellent timing can be expected for each of the devices involved in collecting the light from a shower. The time difference from the two ends produces the z coordinate of the hit.

Because we will use an array of such devices on each end (segmented in azimuth and depth), redundant measurements are made of the z coordinate. These measurements of z correspond to different average radii and therefore help to establish the angle of the incoming photon.

The fractional volume of scintillator in the detector naturally makes it efficient for detecting charged hadrons. The mean light collection time of the two readout ends can be used to determine the particle time-of-flight (TOF). TOF coupled with the track length and momentum then yields particle mass. Therefore, this design for a Barrel Calorimeter is expected to play an important role in the overall barrel PID scheme. KLOE achieved an operational time resolution of

$$\sigma_t = \frac{56\ \text{ps}}{\sqrt{E(\text{GeV})}} \oplus 133\ \text{ps},$$

which yields a nearly constant $\sigma_t \approx 180$ ps for photon energies above 150 MeV, and a diverging time resolution for $E_\gamma < 75$ MeV. The first term is the sampling fluctuation term, and can be reduced by improving the calorimeter light collection. The constant term is mostly due to the intrinsic time spread due to the finite length in the z direction of the luminous point. Improvements on this are possible. A similar figure can be expected for GLUEX as long as readout devices and discriminator chains are selected carefully.

The GlueX BCAL

Pb/SciFi calorimeters have been built that satisfy the physics requirements of GLUEX. By using the knowledge gained in the KLOE construction, members of the GLUEX collaboration expect to improve on this for the GLUEX experiment.

For GLUEX, we expect to build 48 modules each $\sim 4\ m$ in length and 20–25 cm deep. The readout scheme takes advantage of the fact that all fibers run parallel to the axis of symmetry of the solenoid and therefore all light piped to the ends of the modules retains its azimuthal and radial information. The polished ends of the detectors will be coupled with multiple independent light guides.

Because the EM showers spread across these azimuthal boundaries, algorithms for finer positioning of the shower are employed. In JetSet, one finds a typical weighted position resolution of $\delta x \approx 5\ mm\ /\sqrt{E}$. For the GLUEX design, this would lead to an azimuthal resolution of ≈ 8.5 mrad. Using the z position resolution of approximately 4 cm obtained from the time

difference leads to a polar angular resolution at 45° of ≈ 7 mrad. As the design of the BCAL is further refined, it will be important to keep these numbers balanced.

The transverse size of each of the 48 modules is approximately 8.5 *cm* at impact. A further subdivision of the readout can reduce this number by half or more. In Figure 6.16, ten (two in width times five in depth) segments per azimuthal slice are shown as a minimal example of the readout subdivision. Each such segment would contain approximately 1200 fibers. In effect, this subdivision could be made smaller whether PMT's or SIPM's are used. The former would require a (clear) fiber-to-fiber mask to carry the light outside the magnetic field, whereas the latter would need a Winston cone with a light mixer or a diffuser, and wavelength shifting fibers (WLSF's) or ordinary fibers to further guide the light to the small surface of each SIPM. The investigation into the optimal readout scheme is now underway and will couple Monte Carlo simulations of the expected light produced to R&D trials in the lab with different geometries using SIPM's and PMT's.
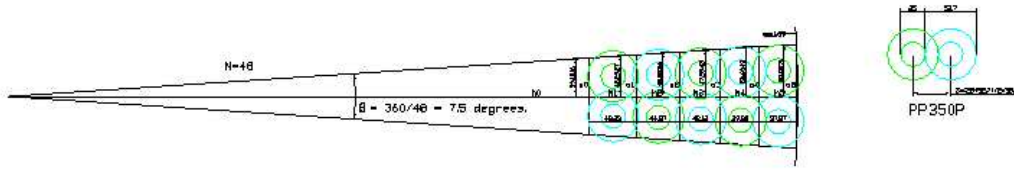

Figure 6.16: Sketch of Barrel Calorimeter readout ends. The subtended angle of each module corresponds to two azimuthal slices. Each slice has five readout devices on either end. As an example, the dimensions of DEP PP00350G HPMTs were used. The outer circles represent the boundary of the devices, assuming a 5.27 *cm* outer diameter. The devices have been closely packed so as to not shield each other's active area, which is indicated by the smaller circles (diameter of 2.5 *cm*). The readouts have been staggered axially to allow the closest packing.

Each channel requires high voltage, a flash ADC, discriminator, TDC and cabling. A calibration system is critical and can be based in part on the use of Nichia blue (or green) LEDs glued directly to a short light guide stub at the end of each module. An LED driver system is also required. The choice of ADC and TDC systems depends on the overall readout coordination for GLUEX.

Construction of Prototype Modules

In order to form grooved plates and construct modules 4 *m* long, we have studied and used the KLOE tooling techniques. GLUEX physicists visited Frascati and Pisa and were trained in the use of the KLOE 15 *cm*-wide lead swaging machine (a.k.a. *Francesca*). In May 2002, the GLUEX physicists successfully swaged 0.5 *mm* thick lead sheets, and glued 10 layers of lead and 1 *mm* optical fibers together, producing the first Pb/SciFi test module with dimensions 100 *cm* x 14 *cm* x 1.25 *cm* at LNF/Frascati. Francesca (total weight of 200 kg) was then moved to Canada on a two–year loan from Frascati, where four prototypes have been built:

1. 1 *m* x 13 *cm* x 5.0 *cm, Baby-0 Module*

2. 2 *m* x 13 *cm* x 17.0 *cm, Module-0*

3. 4 *m* x 13 *cm* x 23.7 *cm, Module-1*

4. 1 *m* x 13 *cm* x 5.0 *cm, Baby-1 Module*

As is reported below, the construction of all modules was met with success, with only minor faults resulting in the uniformity of each of the three matrices. The construction method has been adjusted to avoid these in the production phase. Francesca has been returned to LNF; we will design and build a similar machine for our production phase.

Production of Lead Sheets   The initial stages of construction for the 4m module calorimeter took place in February-April 2004 at the University of Regina. The main focus was to produce the needed lead rolls for the first full–length module (Module-1) of the Barrel Calorimeter at Hall D. A total of 240 rolls were cut, swaged and shipped to the Centre for Subatomic Research (CSR) at the University of Alberta where this module would be constructed.

The lead came from the manufacturer[1] on a giant roll, 27" wide. Five sheets (width-wise) could be extracted from each length of lead. The quality of lead used for this module was superior to that used for the $2\,m$ module. The lead used for Module-1 had a lower percentage of copper than the roll used in the $2\,m$ module (Module-0) and was consequently softer and easier to ply. *Bananas* (curved sheets resulting from uneven pressure of the rollers during the swaging process, or from impurities in the lead itself) were a continuous problem for Module-0. Bananas rarely occurred for the lead used in Module-1: out of 240 sheets there were only three irreversible bananas.

The wide lead sheets were placed under a special cutter that consists of two parallel blades, separated by $12.93\,cm$, attached to a roller on tracks. This cutter greatly reduced the cutting time over the mask and box cutters used in the previous modules. A few improvements in the design (easier exchange of blades, smoother insertion/extraction of lead sheets) are planned for the production phase, as well as a multi–track enhancement to allow cutting of 4-5 sheets at the same time. The lead was then swaged with Francesca to have 96 lengthwise grooves on both sides and trimmed to $404\,cm$.

The time required to cut and swage a sheet of lead, where one sheet contains 4-5 rolls of lead, changed with experience. Once a rhythm was established, on a good day with four workers, the time had reduced to approximately 9 min/roll with a daily total of about 30 rolls. After several trials of methods to lay the fibers in the lead grooves, a detailed method was developed [27]. This lead to the successful construction of Module-1.

Module Construction   During the summer of 2004 the University of Regina sent a team of undergraduates to Edmonton to build a 4m calorimeter module. Composed of 210 alternating layers of lead and scintillating fiber the module measured $4.04\,m$ in length, $12\,cm$ in width and $24\,cm$ high. Over 80 km of fibers and 12 kg of epoxy was used in the four weeks of construction. The process itself was a learning experience, as much of the facility was custom built for the occasion.

The first stage of construction included the machining, assembly and installation of an electro-pneumatic press, used to press the matrix as it is being stacked with alternating layers of lead sheets and fibers. It consisted of steel bed, two tilting pistons that raised/lowered a group of 20 pistons to the top surface of the matrix, and the associated electronics and pneumatics.

The second stage of construction consisted of building the clean room where the module would be constructed. This was a $7\,m$ x $5\,m$ x $3\,m$ room lined with Tyvek sheathing and black polyethylene sheets along its walls, and clear poly and UV filters as its ceiling. The room was ventilated with a variable speed fan and was equipped with an air exhaust. An airlock provided access to the room. The third stage of construction was the building of the $4\ m$ module. A five member crew built this module working two three-hour shifts each day. This resulted in module growth of two centimeters each day. The fourth and final stage of the production was the construction of a one-meter Baby-1 module that was only 5 cm thick. This module is to be used for testing various readout systems.

Most tasks in the construction process are simple ones that are repeated each layer. A comprehensive report (how–to manual) and training video were prepare to simplify the training of personnel during the production phase and to document the methods employed [28].

The optimum size of the construction team turned out to be five people. Accurate documentation of all stages of the construction over a five week period show that just over 300 man hours are needed for each module, or a total of almost 15 thousand man hours for the construction of 48 modules. The construction of a second press and operations with two crews would allow the

---

[1]Vulcan Lead Inc, *http : //www.vulcunlead.com/*

completion of the production phase in well under 24 months.

The Summer 2004 construction was a successful practice of full scale production. There were unanticipated problems and useful discoveries. The full set of recommendations for improving the construction technique is described in [28]. The GLUEX Collaboration believes that all R&D issues on the Pb/SciFi matrix construction have been resolved and that we are ready to proceed to the production phase.

Following the completion of the construction, Module-1 was craned out of the clean area and its ends machined and polished to final dimensions of 400 *cm* x 13 *cm* x 23.7 *cm* and was moved to Regina. A picture of one end of the module is shown in Fig. 6.17. A jump in the tracks of a single fiber layer is visible only on this end; the fibers are sitting properly at the other end. This was a result of having to lift the lead to realign it, something that had to be done several times and only once is resulted in misaligned fibers. This mishap has no effect on the light collection and integration of the module and will be tested for potential delamination. The testing of Module-1 with cosmic rays is underway at Regina and in 2005 the module will be tested in beam conditions at Serpukhov and latter at Jefferson Lab (Hall-B). Baby-1 will be cut into two equal length pieces that will be shipped to CERN and Athens for front end readout tests.
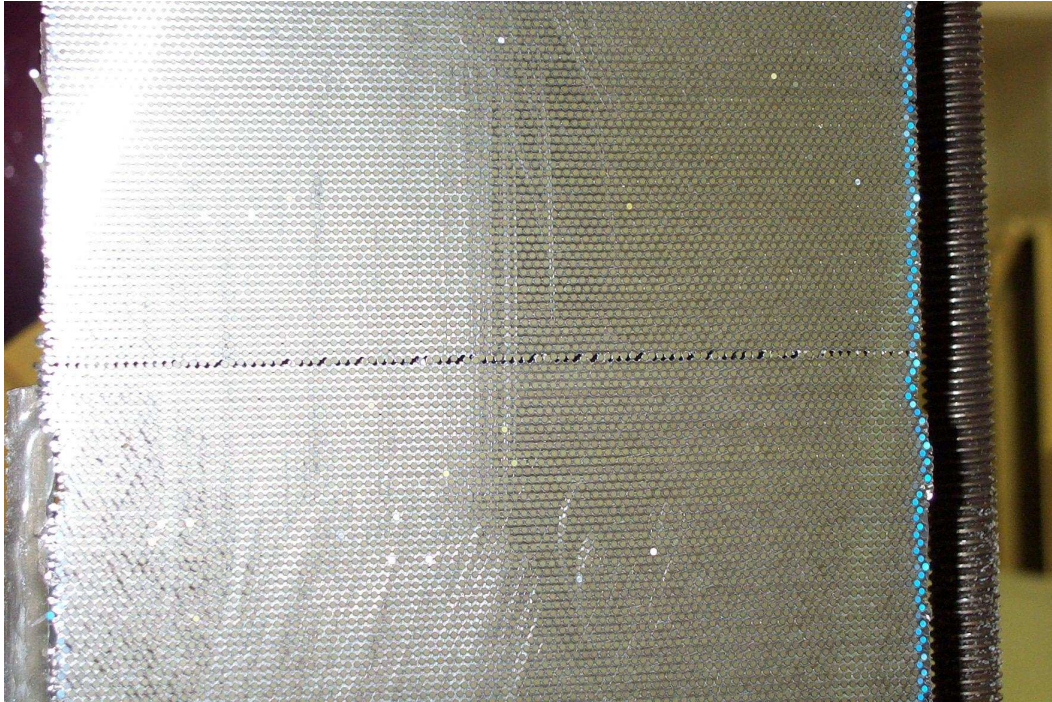

Figure 6.17: Module-1 end. Note the layer that has jumped its tracks. See text for a detailed description.

Scintillating Fiber Tests

Clearly, the inherent properties of scintillating fibers play a crucial role for the Barrel Calorimeter function. The criteria which must be evaluated include:

- Light collection efficiency (cladding),

- Amount of scintillation light produced (doping), and

- Loss of the light as it travels down the fiber (attenuation length) and decomposition of intensity as a function of wavelength.

- UV damage of fibers when exposed to sunlight or fluorescent lights.

To address the first three points, different types of fibers from two different manufacturers were procured and tested first with cosmics and then a pion beam at TRIUMF, Vancouver, in connection to their light attenuation and timing resolution. Specifically, the tested fibers were Kuraray SCSF-81 single–clad[2], Pol.Hi.Tech.0046 single– and multi–clad[3]. All fibers were 1 *mm* in diameter and were procured in the summer of 2000. In addition, a second bundle of single–clad Kuraray fibers was procured in 2001. Beam tests of these fibers are reported in reference [29], whereas tests of newer (2002 batch) Kuraray multi–clad and Pol.Hi.Tech. multi–clad fibers have been conducted using a spectrophotometer and the light output has been analyzed as a function of wavelength.

To evaluate the attenuation length of the various fibers tested, it is necessary to evaluate first the ratio of the means of the left and right PMT ADC values at each position along the beam. To understand this, consider that the attenuation of light as it travels along the fiber is given by

$$I(z) = I_0(z)e^{-z/\lambda} \tag{6.5}$$

where z is the distance from the point of impact of the beam along the fiber to the appropriate PMT, λ is the attenuation length, and $I_0(z)$ is the amount of light produced at the interaction point.

In practice, it is found that the amount of light produced at the interaction point is a function of z. Consequently, the ADC values for the two PMT's in question may be expressed as

$$ADC_{left} = f(z)e^{-z/\lambda} \ and \ ADC_{right} = f(z)e^{z/\lambda}, \tag{6.6}$$

where $f(z)$ is the geometric mean calculated from

$$f(z) = \sqrt{(ADC_{left}ADC_{right})}. \tag{6.7}$$

Thus, a reliable method to extract the attenuation length value is to take the ratio between the two ADC values above:

$$ln(ADC_{left}/ADC_{right}) = -2z/\lambda. \tag{6.8}$$

Plotting the ADC ratio values at different positions on a semi–log scale results in a straight line with a slope of $-2/\lambda$. This is what is shown in Fig. 6.18 for all fiber bundles, where the curves have been shifted along the y-axis for clarity.

It is evident that the attenuation lengths of the Kuraray fibers are quite reproducible between different fiber samples, as well as different geometrical configurations. The Pol.Hi.Tech. multi–clad fibers had an attenuation length of $\lambda = (234 \pm 3)$ cm, considerably shorter that the Kuraray fibers. All the results are in broad agreement with those of KLOE and are presented in Table 6.2. It should be mentioned that the KLOE Collaboration also tested BICRON[4] scintillating fibers, but recent price quotes from BICRON revealed that these are too costly for the HALL D project and so were excluded from testing for this reason.

To determine the timing resolution of the fiber bundles, the software mean time and the left-right timing difference must be computed. These quantities should have constant values at any given point along the fiber. However, there are some uncertainties associated with these values, which arise from inherent timing resolution of PMTs involved and photon statistics.

The timing resolution was determined with two methods that yielded consistent results. Statistically it appears that Kuraray fibers have superior timing resolution to the Pol.Hi.Tech. fibers which implies that the former fibers have better light production and light collection capabilities. All fiber bundles gave $\sigma = 550 - 700 \ ps$. This is consistent with the KLOE results which had $\sigma = 300 \ ps$ for the Pol.Hi.Tech. and Kuraray fibers and $400 \ ps$ for the Bicron fibers,

---

[2]Kuraray Co., Ltd., 3-1-6, Nihonnbashi, Chuo-ku, Tokyo 103-8254, Japan.
[3]Pol.Hi.Tech. s.r.l.0, Carsoli, Italy.
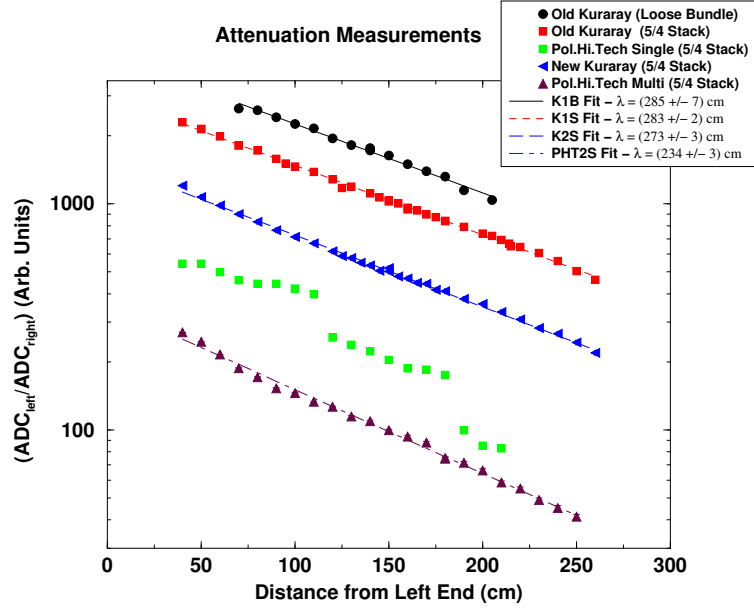[4]BICRON Corporation, Newbury, Ohio, USA.

Figure 6.18: Attenuation length measurements for various fibers. The Pol.Hi.Tech. single–clad fibers appear to have been broken or stressed at the locations where the discontinuities appear in their curve (unconnected squares).

when the number of photo-electrons collected was $N(p.e.) = 30$. These numbers rise to 500-800 ps for $N(p.e.) \leq 10$. From the TRIUMF measurements, fitting of the ADC spectra yielded $N(p.e.) \leq 4$. Thus, the TRIUMF results are consistent, at least qualitatively, with those from KLOE. Additional details can be found in reference [29].

The Kuraray fibers showed a consistently better performance as per the light attenuation coefficient and timing resolution. However, the Pol.Hi.Tech. multi–clad fibers performed better in terms of light yield, based simply on the observation that for the same bias and gain the mean of the ADC spectra for these fibers was higher. These fibers had more than adequate performance for the requirements of the GLUEX experiment and are considerably cheaper (by a factor of 2) than the Kuraray fibers. For this reason, Pol.Hi.Tech. multi–clad fibers have been used in the construction of all prototype modules, except Baby-0.

Fiber Light Transmission Tests

Light-transmission tests of the scintillating fibers have been conducted using a dedicated optical testing system that employs LED light sources with different wavelengths, transport light guide fibers, optical filters, and is coupled to a dual-channel spectrophotometer and ADC. The system is sensitive to wavelengths from 350 nm to 1000 nm, is connected to the USB port of a laptop, and is read out by means of commercial software.

Preliminary tests had indicated that exposing scintillating fibers to UV light caused degradation in transmission intensity. This agreed with test results from KLOE [25]. The next step was to understand the reason for this decrease in light emission. One possibility was that UV exposure created cloudiness in the fiber, causing a decrease in attenuation length. Another theory was that after exposure, the fibers were absorbing light in different regions, shifting the output spectrum away from the PMT's peak efficiency. Using an Ocean Optics Inc. (OOI) [5] SD2000 spectrometer coupled successively to UV (380 nm), Blue (470 nm) and Tungsten ($\lambda = 350 - 1100\,nm$) diodes, scintillating fibers were exposed to UV light emitted from normal fluorescent room lights while periodically measuring the fibers' output spectra.

---

[5] $http://www.oceanoptics.com/$

Batch	Fiber Type (mode)	Attenuation Length (cm)		
		Cosmics	TRIUMF	KLOE
1992	Bicron BCF-12			226 ± 3
1993	Bicron BCF-12			286 ± 8
N/A	Kuraray SCSF-81 single–clad			321 ± 5
1992	Pol.Hi.Tech.0046 single–clad			284 ± 5
1993	Pol.Hi.Tech.0046 single–clad			267 ± 6
2000	Kur.SCSF-81 single–clad (loose)	321 ± 22	285 ± 7	
2000	Kur.SCSF-81 single–clad (5/4)		283 ± 2	
2001	Kur.SCSF-81 single–clad (5/4)		273 ± 3	
2000	P.H.T.0046 single–clad (loose)	259 ± 20		
2000	P.H.T.0046 multi–clad (loose)	247 ± 47		
2000	P.H.T.0046 single–clad (5/4)		Broken	
2000	P.H.T.0046 multi–clad (5/4)		234 ± 3	

Table 6.2: Attenuation length determined using 2" PMT's following the cosmics runs and the TRIUMF beam tests. The results are compared to those from the KLOE Collaboration [25, 30].

Light from the diodes was divided into two channels. The master channel passed through a clear reference fiber that allowed us to monitor the stability of the diode. The sample scintillating fibers were placed into the slave channel. Five scintillating fibers and one Bicron (clear) light-guiding fiber were chosen at random to be tested. The six fibers were placed parallel to each other on a table and irradiated by leaving the room lights on for long periods of time. During the measurement of the output spectra of the fibers, all room lights were turned off and only lamps with UV filters were on.

Data reproducibility was a major concern for our experiment. If the fibers were not coupled into the OOI system in a consistent fashion, it would be impossible to compare recorded spectra from one hour to the next. Furthermore, it had been discovered that small rotations in the reference fiber at the connection point to the spectrometer could change the intensity of the reference spectrum by up to fifty percent.

A method that eliminated coupling as a contributing factor was sought. It was decided to perform the experiment one fiber at a time, leaving it connected to the OOI system even during exposure. One fiber was placed into the system and left unexposed over night. When re-tested in the morning, the results were found to be nearly identical. This gave a degree of confidence in the data to be collected. The light source used was the 470 nm LED. The results are shown in Fig. 6.19. A key observation in this figure is the effective "shift" of the spectra to higher values of λ. This is a result of a significant reduction of spectral strength in the blue region, precisely where PMT's are the most sensitive.

An additional interesting feature of these fibers can be gleaned from measurements of their light output as a function of length. These measurements are shown in Fig. 6.20. The reader is directed to notice the λ=400-480 nm region. Clearly, a reduction in intensity is observed with increasing fiber length. It should be mentioned that these measurements were done on a single fiber, starting with a 410 cm fiber that was successively trimmed to shorter lengths with its cut end being polished each time. As it turns out, such a light response is more suited for collection by SIPM's whose overall efficiency peaks in the yellow-green region. However, this renders yellow-green WLSF's useless when coupled to SIPM's; red WLSF's would have to be used instead and these suffer from poor timing resolution. The effect is pronounced enough to be visible by eye, as displayed in Fig. 6.20.

These measurements were repeated using a UV diode (380 nm) and the results are being analyzed. Several lessons were learned that will help future measurements of the spectral response of scintillating fibers [31]. In the future, the long term effects of cosmic rays on scintillating fibers should be studied to give an idea of the longevity of the Barrel Calorimeter. This can be achieved by placing a select group of fibers into a tube made of UV filter and measuring

Figure 6.19: Degradation of fiber intensity as a function of UV exposure time. These are the final measurements using the 470 nm LED.

the spectra every few months. Due to the extreme length of this investigation, it is not feasible to study one fiber at a time. In this case, plenty of care must be given to ensuring consistent coupling between the fibers and the OOI system.

Silicon Photomultiplier Tests

Although single-pixel Geiger mode devices (Avalanche Photo Diodes - APDs) were developed in the mid sixties, the SIPM is a novel type of APD [32]. It is a promising device for our application in GlueX, since it is insensitive to magnetic fields, has a high gain ($\sim 10^6$), good quantum efficiency, provides excellent timing resolution (~ 120 ns for single photo electron detection) and a fast risetime (sub- ns), achieves good dynamic range ($\sim 10^3/\text{mm}^2$), and does not suffer from nuclear counter effects when operated in Geiger mode. Finally, it has a solid performance at room temperature (in contrast to VLPCs) and does not exhibit any serious radiation damage effects, other than perhaps from neutrons [33].

The SIPM is a multi-pixel photo diode with a large number of micro pixels (500-1500 each with a typical size of $20-30$ μm) joined together on a common substrate and under a common load. The total number of pixels defines the dynamic range of the photodetector. The photodiode has a multi-layer structure with different doping levels. As a result, within the thin depletion region between p^+ and n^+ layers, a very high electric field of about 5×10^5 V/cm is created, with the right conditions for a Geiger discharge mode to take place. The operational bias voltage is $10-20\%$ higher than breakdown voltage, with typical supplied bias voltage of $50-60$ V.

The single pixel gain is approximately 10^6, roughly the same order of magnitude as that of a traditional PMT. While each pixel operates digitally as a binary device – because all SIPM pixels work together on a common load and there is a large number of pixels – the output signal is a sum of the signals from all pixels registering a "hit". Thus, the SiPM, as whole, is an analogue detector that can measure the incident light intensity. The distribution of the voltage across the depletion depth of $4-6$ μm is such that for only a fraction of the depth ($\sim1-2$ μm) the former exceeds a value sufficient for Geiger discharge creation, and therefore, the Geiger discharge is
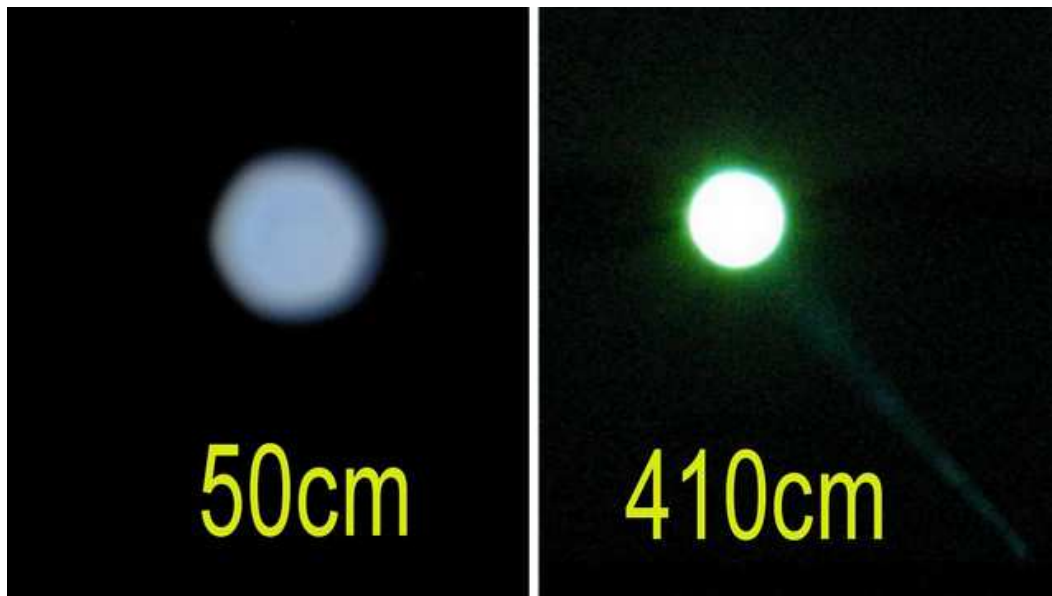
Figure 6.20: Fiber intensity as a function fiber length. These are the final measurements using the 470 *nm* LED. The shift in color from blue to green is evident even visually.

contained within this limited region. As a result, its duration is very short, a few hundreds of ps, resulting in typical rise times of 1 ns.

The SIPM's photon detection efficiency, η, is given by $\eta = QE \cdot \varepsilon$, where η is the photon detection efficiency, QE is the quantum efficiency and ε is a geometrical factor. The latter is a ratio of the sensitive area (as defined by the total active pixel area) to the total area. This value does not depend on wavelength and is a constant for each SIPM. The devices used in our particular tests had geometrical factors of 0.3/1.0 for all SIPM's/PMT's investigated, respectively.

The SIPM's used in our tests were developed and produced by the Moscow Engineering and Physics Institute (MEPHI) in cooperation with a state enterprise (PULSAR). The specific SIPM's had 1000 pixels in each detector covering the 1 mm^2 sensitive area and the supplied bias voltage was $50-60$ V. Although the geometrical factor for these SIPM's was 0.3, efforts are underway at MEPHI/PULSAR to increase this to as much as 0.7. Competitors at the University of Obninsk in cooperation with a private firm (CPTA) [34] claim that their device has 50% higher photon detection efficiency in the green region and fewer constraints on mechanical performance. Moreover, the Obninsk/CPTA is investigating the construction of larger areas by connecting SIPM's in a matrix configuration [34]. We have recently obtained 60 1 mm^2 CPTA units and these are currently undergoing evaluation at Regina. In addition, negotiations are underway with experts at CERN and DESY to allow for future testing of these devices with sophisticated setups and for testing with beam.

Tests of the MEPHI SIPM's were conducted in order to investigate their use as front-end detectors for the Barrel Calorimeter readout system. The results of this work have been accepted for publication in Nuclear Instruments and Methods. Specifically the SIPM's were investigated under the following two conditions: a) detection of incident light of high flux intensity, where about $200-500$ SIPM pixels registered a hit but the signal was not saturated, and b) Detection of light of lower photon flux intensity in which case only few pixels registered a hit. This regime corresponds to a few-photon-counting condition.

An Optitron nanosecond broad spectrum optical pulse radiator (Model NR-1A) with a Nitrogen Plasma Discharge Tube[6] was used as a source of light for the SIPM investigation under high photon flux conditions. The light pulses had a 1 ns rise time and a few ns pulse duration, and were measured with the SIPM as well as with a 2" Burle PMT (model 8575). A clear, pure fused silica fiber of 5 m length was used to transport the light from the Optitron plasma discharge tube to the sensitive surface of the SIPM. The light intensity emitted from was monitored by the PMT.

Pulses from the SIPM and the PMT were measured with a Tektronix TDS-5104 digital oscilloscope. The detected signal amplitude for the SIPM was $\sim$300 mV, corresponding to $\sim$200$-$300 pixels registering a hit. Whereas the timing distributions have a similar structure with risetimes of 1 ns and 4 ns for the SIPM and PMT, respectively, the former has a σ that is less than half of the latter's: $\sigma = 140$ ps vs. 375 ps.

In order to investigate the energy resolution of the SIPM, we measured the pulse amplitude distribution under low photon flux conditions employing the Optitron unit and a neutral-density attenuation filter that reduced the light to 1% of its initial value. The amplitude of the signals in the SIPM, in this case, was $5-10$ mV, and this necessitated the use of a fast amplifier (LeCroy 612A). Under such conditions it was not possible to eliminate completely the noise pick-up from electronic equipment present in the area. Nevertheless, the pulse amplitude distribution shown in Fig. 6.21 exhibits five well separated peaks corresponding to single photon detection and good separation for emission of up to five photoelectrons.

Next, we evaluated the performance of the SIPM used as a front-end detector for light signals produced by minimum ionization particles traversing a 4-m-long Kuraray SCSF-81 single-clad SciFi. Fibers with similar parameters will be used in the Barrel Calorimeter for GLUEX detector system.

Kuraray SCSF-81 SciFi's have an emission spectrum range of $400-550$ nm, peaking at 437 nm, with a 2.4 ns scintillation decay time and an attenuation length of $\sim$3.5 m. The

---

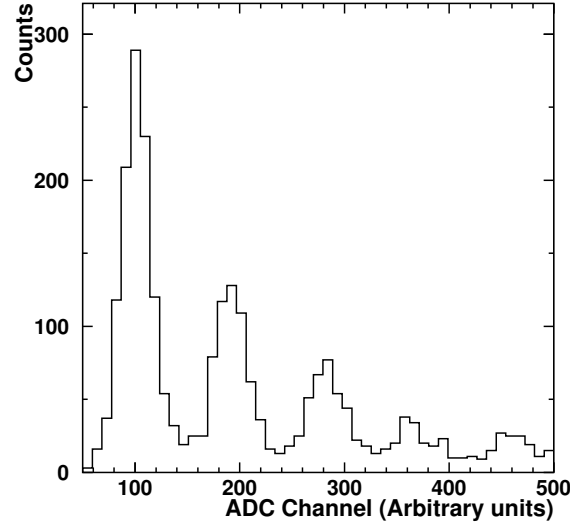[6]Optitron Inc. 23206 Normandie Ave. #8, Torrance, CA 90502, USA.

Figure 6.21: SIPM pulse height spectrum for low intensity light pulses.

fiber was in direct contact with the surface of the PMT window, while it had a 0.3−0.5 mm air gap between the end of the fiber and the sensitive surface of the SIPM in order to prevent damage to the SIPM. It should be noted that the Burle 8575 PMT has a 25% efficiency at the peak of the Kuraray emission wavelength while the SIPM's efficiency for that region is about 15%. As a result, for the the same light intensity from the scintillating fiber, the SIPM exhibits a photon detection efficiency that is 60% of the PMT's. The comparison in efficiency between the two devices is summarized in Table 6.3.

λ	Device	ϵ	QE	η
550 nm	SIPM	0.3	60%	20%
	PMT	1.0	5%	5%
437 nm	SIPM	0.3	45%	15%
	PMT	1.0	25%	25%

Table 6.3: Detection efficiency, $\eta = QE \cdot \varepsilon$, for the SIPM's and PMT's.

The scintillating fiber was excited using a ^{90}Sr(^{90}Y) beta source that has a 2280 keV maximal and 935 keV average energy of beta particles. The difference in the distributions of ionization energy loss in the scintillating-fiber core, as calculated by a Monte-Carlo simulation for the triggering beta particles and compared to the minimum ionization particles, is only a few percent on average [35]. The TDC and ADC spectra were accumulated and analyzed to extract the dependence of the detected light and timing resolution as a function of distance of the source from the respective readout end of the fiber. The mean values of the distributions were used in the calculation of the attenuation length.

The experimental data were fit with an exponential curve, $y = I \cdot \exp(-x/L)$, where I is the amount of light produced at the interaction point, L is the attenuation length and x is the distance to the ionization source. The ratios of the mean values for the two identical positions of an ionization source are larger for the PMT in comparison with the SIPM. As a result, two different

Time resolution for PMT and SiPM
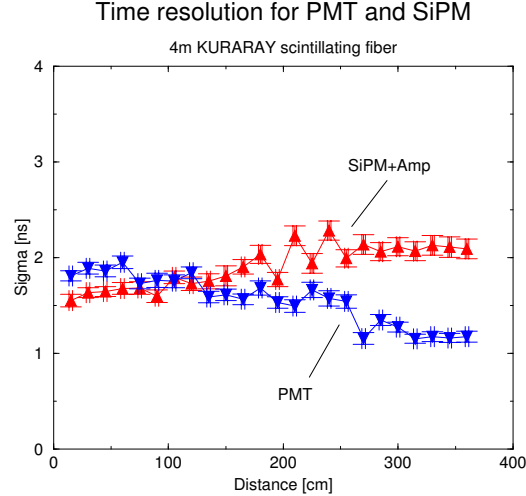
Figure 6.22: The timing resolution as a function of the distance from the v detector.

attenuation lengths were obtained for the same fiber, $L_{SiPM} = 251$ cm and $L_{PMT} = 146$ cm for the SIPM and the PMT data, respectively, stemming from the difference in the spectral sensitivity of these two devices. The SIPM is more sensitive to longer values of λ where the transmission loss for the Kuraray fiber is lower. Therefore, the SIPM "realizes" a longer attenuation length compared to the PMT. Obviously, the SIPM-fiber combination provides a clear advantage over the PMT-fiber one, in applications where long fibers must be used.

The TDC peak location (the mean value of the Gaussian fit) was plotted versus the distance from the front-end detector. The slopes of the linear fits for the SIPM and the PMT agree with each other within the error of measurement, and are equal to 1.32±0.01 ch/cm and 1.33±0.01 ch/cm for the v and the PMT experimental data, respectively. The TDC conversion factor was 47 ps/ch. The calculation of the velocity of light propagation gives $v = (1.60 \pm 0.03) \times 10^8$ m/s, a value that agrees with the Kuraray SciFi specifications sheet.

The timing resolution is presented in Fig. 6.22 as a function of the distance of the ionization source from each front-end detector. The data presented in Fig. 6.22 have not been corrected for the time jitter of the trigger detector or the jitter connected with the LeCroy 612 amplifier. The smallest values of sigma were 1.5 ns and 1.1 ns for the SIPM and the PMT, respectively, corresponding to the minimal distance between the ionization source and the front-end detector. Finally, the timing resolution depends on the number of detected photoelectrons. The average number of photoelectrons detected for the closest position of the ionization source from each front-end detector was ∼3−5 for the SIPM and ∼5−8 for the PMT. The resultant timing resolutions for the SIPM and for the PMT were comparable.

The properties of a SIPM working in Geiger limited mode have been measured and compared with a standard 2" vacuum PMT. The measurement with the nitrogen plasma discharge unit shows that the SIPM can achieve better time and energy resolutions under high photon flux. To evaluate the possibility of using the SIPM as a front-end detector for an electromagnetic calorimeter readout system, we measured the ADC/TDC spectra from the SIPM for $4\,m$ scintillating fiber irradiated by ^{90}Sr beta source. Coupled to the performance attributes of SIPM's, the results of these investigations demonstrated that SIPM's satisfy the basic requirements for such an application.

Although SIPM's appear to satisfy all the performance criteria of timing and energy resolutions - and they also eliminate the need for high voltage supplies and associated cabling - one serious issue remains, namely their small active areas. Conventional coupling methods between the polished area of the fiber-lead composite and the SIPM's are not possible. Embedded wave shifting fibers in plexiglas light-guides or tiles will not suffice either, due to the loss scintillation

light of low λ. One solution under investigation is the use of small light guides to collect the light from an area of the read-out face of the modules, a Winston cone to increase the light density and embedded clear fibers viewed head-on to collect the light to a number of SIPM's. Preliminary calculations indicate an adequate amount of light collected by each SIPM and a matrix of a number of them will combine into one output. We expect to have the first matrix of 16 SIPM's with common voltage supply and output within a few months and testing to begin.

6.3.4   Upstream Photon Veto

Studies of the photon angular distribution for the GLUEX experiment have shown the need for photon detection in the backward or upstream direction [19]. Several exclusive reactions, listed below, contain photons in the final state originating from both the meson and baryon decay vertexes, and were simulated to study the emission angles of the decay particles within the HALL D detector. These reactions were simulated using the GENR8 [36] phase space event generator assuming a photon beam energy of 9 GeV and a t dependence of $e^{-5|t|}$. The Monte Carlo events were then tracked through a simulation of the detector assuming the production and decay vertex coincided with the center of the target region, and analyzed for three different detector regions: the lead glass detector, barrel calorimeter, and the backward region upstream of the target (see Figure 6.23).

$$\gamma p \to N^*(1500)\pi^+ \to (n\eta)\pi^+ \to n\pi^+\gamma\gamma$$

$$\gamma p \to X^+(1600)\Delta^o \to (\pi^+\pi^+\pi^-)(n\pi^o) \to \pi^+\pi^+\pi^- n\gamma\gamma$$

$$\gamma p \to X^+(1600)n \to (\eta\pi^+)n \to n\pi^+\gamma\gamma$$

$$\gamma p \to X(1600)p \to (\pi^+\pi^-\pi^o)p \to p\pi^+\pi^-\gamma\gamma$$

In addition to the importance of keeping the energy threshold of the barrel calorimeter and the lead glass as low as possible, it was found that the reactions with photons emanating from the baryon decay vertex have shown that approximately 10% of the photons miss detection by either the barrel calorimeter or the lead glass detector. These photons go undetected by escaping out the upstream hole, which corresponds to emission angles greater than 117°.
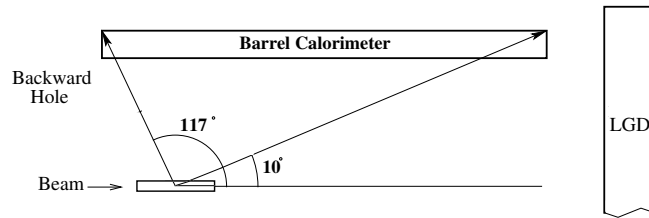
Figure 6.23: Angular distribution, in degrees, from the center of the target to various reference points, for various simulated reaction channels. Tracks more forward than 10° miss the barrel calorimeter and will hit the LGD. Between 10° and 117° the photons will enter the barrel calorimeter. Photons produced at angles larger than 117° miss both calorimeter detectors, and necessitate the construction of an upstream veto detector to achieve near hermeticity.

Figure 6.24 displays where these lost photons hit the plane at the upstream end of the solenoid. The ring at 117° is the current barrel calorimeter limit. Several rings are shown

at other angles, indicating the geometrical losses from each. In order to detect the escaping backward photons and provide nearly hermetic photon coverage it is necessary to implement an Upstream Photon Veto counter (UPV).
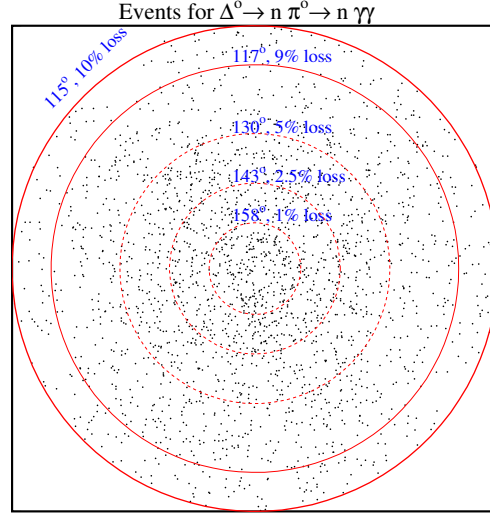

Figure 6.24: The tracked photon intersections on the x-y plane at the upstream end of the barrel calorimeter. The 117° circle is the end of the barrel calorimeter. Various other photon-loss percentages, and their corresponding angles are plotted as well.

Design Considerations

The UPV is a lead scintillator sampling veto calorimeter located directly upstream of the CDC and in place of the solenoid's original field-shaping mirror plate. In the current GLUEX design, this mirror plate is modified by removing all of the soft iron within the inner solenoid radius. This modification effectively removes the upstream mirror plate leaving only a soft iron annulus the size of the magnet coils. This modification has several benefits. First, it allows for upstream access to the target region, cylindrical drift chamber, and the upstream end of the barrel calorimeter. More importantly, it allows for the addition of an upstream photon veto.

The UPV is designed to detect soft photons of energy 20 MeV and greater emerging from the target region. The counter is able to detect multiple photons with fast detection and with timing information that may be utilized at the trigger level.

As shown in Figure 6.25, the UPV consists of 18 layers of 1 cm thick scintillator alternating with first 12 layers 0.185 cm thick lead sheets ($0.36X_0$ each) then 6 layers of 0.370 cm thick lead sheets ($0.72X_0$ each). This design was simulated using the GEANT 4 package to study the expected performance of the UPV calorimeter. The study uses a photon beam of various energies incident normal to the detector face. The results, summarized in Figure 6.26, ignore quantum fluctuations and express an optimal resolution of $\frac{\sigma}{E} = 5\% + \frac{8\%}{\sqrt{E(GeV)}}$.

Each scintillator layer consists of seven 34 $cm \times$ 238 cm paddles forming a plane. The central paddle has a 10 cm hole to allow for the passage of the beam. The effective area of each plane is approximately 238 $cm \times$ 238 cm. The total counter thickness is 22.4 cm or $8.91X_0$. The layers are arranged into three alternating orientations: x, u, and v ($\pm45°$, respectively) as shown in Figure 6.25.

The scintillation light collection is realized at one end of each paddle only. The opposite end is coated with an opaque material to eliminate reflections. For each orientation, the light
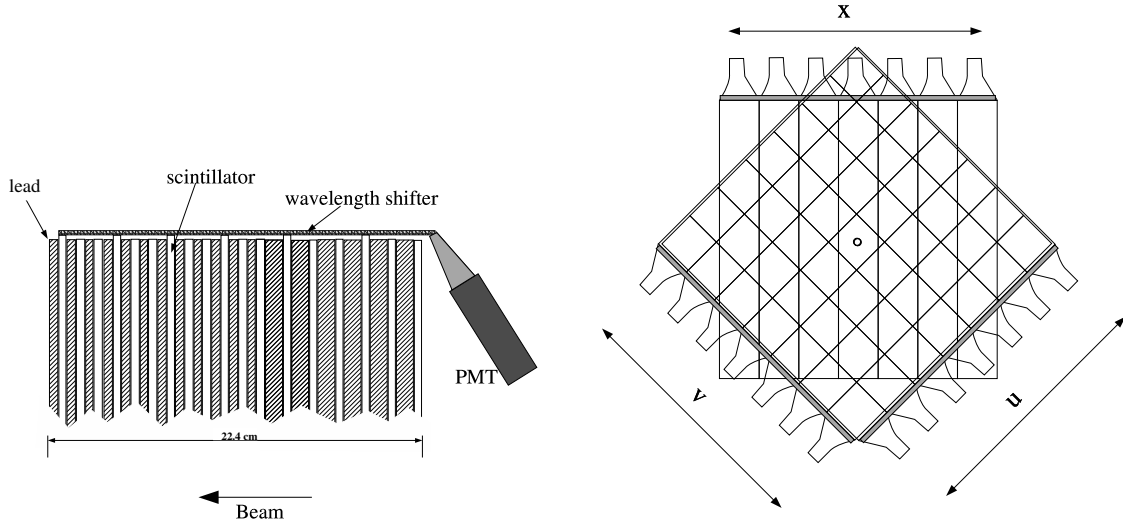
Figure 6.25: The left-hand figure is a sketch of a UPV segment. The 18 scintillator layers are arranged into 3 alternating orientations: x, u, and v. Shown is the light collection for one such orientation. The light-collecting ends of the scintillators are joined together via a wavelength shifter which is oriented perpendicular to the scintillators. The wavelength shifter is used to redirect the light through 90° and out the upstream end of the solenoid to PMTs. The right-hand figure is a sketch of an upstream photon veto counter orientation. The layers are arranged into three alternating orientations: x vertical, u +45° and v −45° layers.
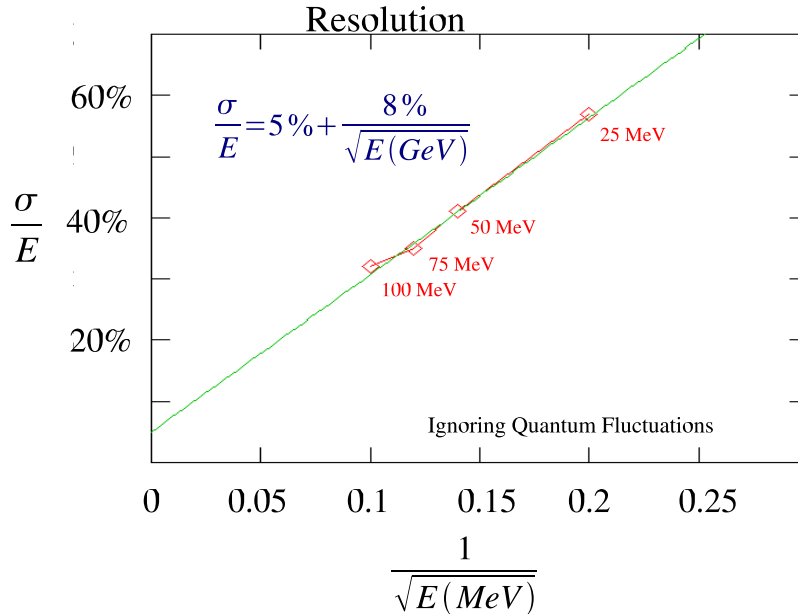
Figure 6.26: Simulation using the GEANT 4 package to study the expected performance of the UPV calorimeter. The study uses a photon beam of various energies incident normal to the detector face. The results, ignoring quantum fluctuations, express an optimal resolution of $\frac{\sigma}{E} = 5\% + \frac{8\%}{\sqrt{E(GeV)}}$.

collecting ends of the scintillators are join together via a wavelength shifter which is oriented perpendicular to the scintillators. The wavelength shifter is used to redirect the light through 90° and out the upstream end of the solenoid to photo-multipliers tubes (PMT). Each PMT is protected from any fringe magnetic field with soft steel casing and mu-metal shield.

6.4 Charged Particle Tracking

The system of tracking chambers in the GLUEX detector must cover as close to a 4π solid angle as possible over a wide range of particle momenta and must have sufficient momentum resolution to be able to identify missing particles. All tracking devices are located inside the barrel calorimeter which is in turn inside the $2.24\,T$ solenoid. The barrel calorimeter defines a maximum keep–out radius of about 65 cm. The physical radius of all chambers has been limited to 59 cm. This provides 6 cm of space for support and installation rails, and cables and gas feeds for the forward chamber packages. In the forward region, the chambers need to extend as close to the beam line as possible. In the initial detector design, there is no vertex chamber around the liquid hydrogen target. A possible upgrade to the system would be the addition of a device which could achieve sub-100 μm resolution. Very accurate vertex information from such a device could be important in identifying secondary vertexes from decaying particles (e.g. K_S, Λ, Σ, ...). In the forward region, it is important to be able to reconstruct fast, small-angle particles (down to nearly 0°). Finally, there is a small hole in the particle identification for particles that spiral and do not reach the barrel calorimeter. It is necessary that in the central region, the tracking should have sufficient dE/dx information to aid in the separation of π's, K's and p's up to momenta of about 0.45 GeV/c — a regime where dE/dx measurements work extremely well.

6.4.1 Design Considerations

In order to achieve the desired goals in the GLUEX tracking, the LASS detector [37] design was used as our starting point. This device used several different tracking elements each optimized for a particular region in the detector. Figure 6.27 shows the GLUEX tracking regions. Surrounding the target is a cylindrical straw-tube drift chamber (CDC) which provides very good $r - \phi$ and good z resolution. In addition, it is necessary for this detector to provide some dE/dx information. In the forward region, round planar drift chambers (FDC) will be arranged in four identical tracking packages. There are still background studies underway to determine exactly how to handle the beam-line region. One option is to have the chambers physically fill the space, but to deaden the active elements that are in the beam line. This could be accomplished by placing Styrofoam around them. An alternative would be to add small support structures around the beam hole and physically remove all material. The final decision will be based on the results of background studies. A summary of the tracking chamber parameters are given in Table 6.4.

System	Radius		Length		Resolution	
	$r_{\min}$	$r_{\max}$	$z_{\min}$	$z_{\max}$	$\sigma_{r-\phi}$	σ_z
CDC	13.0 cm	59.0 cm	10 cm	210 cm	150 μm	1.5 mm
FDC	3.5 cm	59.0 cm	230 cm	400 cm	150 μm	fixed

Table 6.4: A summary of the tracking chamber parameters. The z values under *Length* indicate the smallest and largest z of the combined system. The z origin is at the upstream end of the magnet. The z resolution for the CDC comes from ±6° stereo layers. The z resolution of the planar chambers is assumed to be given by their position in space.

The charged-particle system within the solenoid must be optimized for both overall acceptance and momentum resolution. A detailed study using the *HDFast* framework has been performed to examine this [38]. The results of this study indicate that the above combination
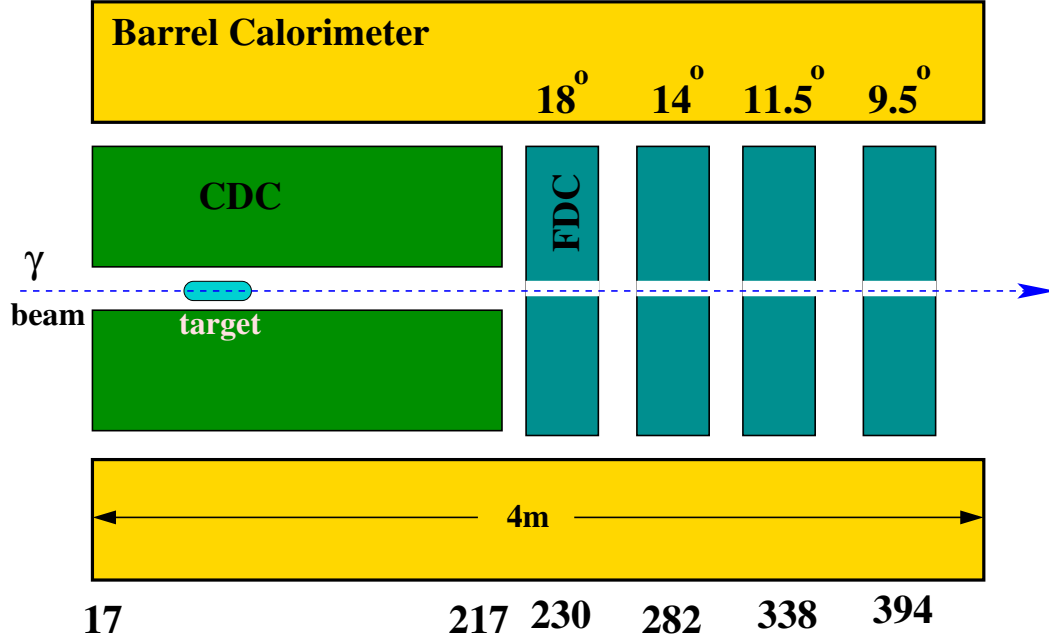
Figure 6.27: The GLUEX detector. The tracking is composed of two elements: a straw-tube chamber called the cylindrical drift chamber (CDC) and circularly-shaped planar chambers designated as the forward drift chambers (FDC). The small gap indicated in the middle of the FDCs is due to wires that will not be instrumented. If background studies merit, we could also consider a physical hole. The distances labeled along the bottom of the figure are the z coordinate of the upstream and downstream ends of the CDC, and the center of each FDC package. The angles labeled above the FDC packages are from the center of the target to the center of the outer edge of the chamber.

of the straw-tube chamber and planar drift chambers with typical $r - \phi$ position resolutions of $150\,\mu m$ will satisfy our requirements. A plot of resolution as a function of angle is shown in Fig 6.28 where we have zoomed in on the forward angles in the left panel of the figure. Note that the current Monte Carlo does not fully deal with the degradation in resolution as the tracks become parallel to the CDC wires. A couple of features of these plots are worth commenting on. The rapid degradation in resolution as one goes to very forward angles is driven by the distance (in z) between the first and fourth FDC packages. The most forward numbers can be decreased by about 0.01 for each additional 25 cm of length. Unfortunately, moving the fourth FDC package further down-stream moves it into a non-uniform field region. This tends to cancel the improved resolution due to the larger length. The degradation in resolution from about 10° to 20° corresponds to the transition region from mixed FDC-CDC tracks to all CDC tracks. It is due to the successive loss of FDC packages being linked to the tracks. It is possible to somewhat shorten the CDC and move the first FDC package upstream. However, if the CDC is shortened by as much as 50 cm, then the transition region degrades significantly. An optimum length for the CDC is between 170 and 200 cm and is currently understudy. Such a small perturbation in length has little effect on construction of the chamber.

The 22.4 kG solenoid field determines the physically measurable quantities, and hence, the momentum resolution. The transverse momentum, $p_\perp$ and the dip–angle, λ, $(\lambda = \frac{\pi}{2} - \theta)$ are measured from the curvature of the tracks and their initial direction. The total momentum and the longitudinal momentum are then obtained from these as $p_{total} = p_\perp \sec \lambda$ and $p_\parallel = p_\perp \tan \lambda$. The accuracy of the $p_\perp$ measurement is completely dominated by the $r - \phi$ resolution of the tracking chambers, while the λ measurement relies on an accurate measurement of both z and the distance traveled.
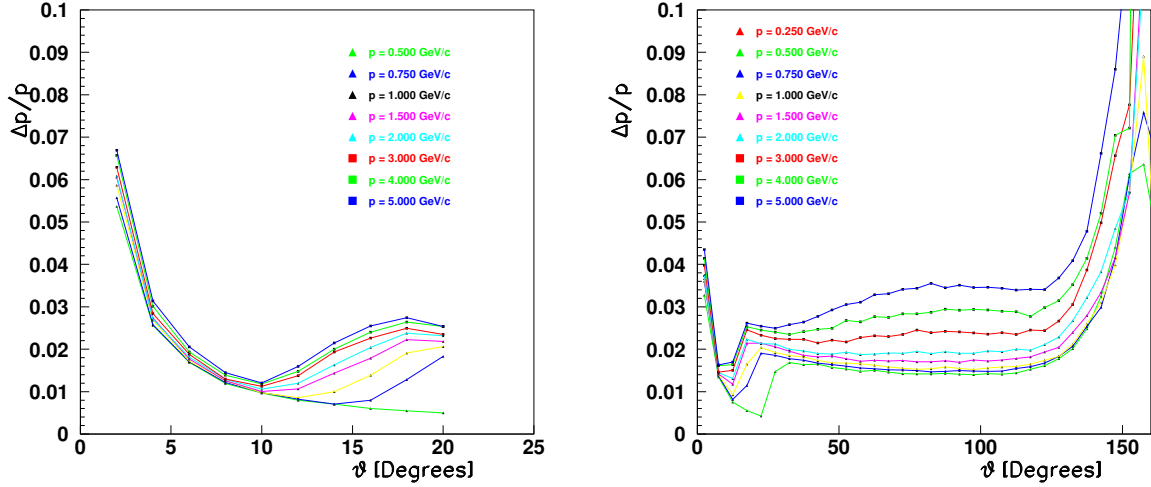
Figure 6.28: The resolution as a function of angle is plotted for several total momenta. The plots correspond to the detector design shown in Figure 6.27. For polar angles larger than 70°, the maximum detected momentum will be well under $1 GeV/c$ so even though the resolution for high-momentum tracks is poor in this large-angle region, it will not affect the overall tracking of physics events.

6.4.2   Track Reconstruction

Track reconstruction effects play a very important role in the design of the combined system. In particular, track matching between different detectors and the associated inter–calibration problems often limit the ultimate resolution. In addition, the high magnetic field strength of $22.4\,kG$ means that tracks may spiral significant distances between measurement planes in the forward direction. This means that one would like as much information as possible from each measured hit in the detector. Other complicating issues are that the magnetic field is non-uniform near the ends of the magnet, and in the region between the end of the solenoid and the forward calorimeter. However, particle identification will require projecting charged tracks forward through this non-uniform field region. Tracking near the end of the solenoid needs to be as good as possible.

An example showing the typical charged particle momentum that needs to be measured comes from reaction 6.9. This final state consisting entirely of charged particles is fairly typical of the typical exotic-hybrid channel that will be studied.

$$\gamma p \rightarrow \eta_1(1800)p \rightarrow \pi^+\pi^-\pi^+\pi^-p \tag{6.9}$$

The exotic spin-one $\eta_1(1800)$ is produced with a mass of 1.8 GeV/c^2 and a typical t distribution. The incident photon energy is $9\,GeV/c^2$. Figure 6.29 shows the transverse and longitudinal components of momentum from the π's in this reaction while Figure 6.30 shows the same distributions for the protons.

From the two sets of plots, several important features can be seen. The charged pions from the decay of the meson system are fairly forward peaked. Once θ_π is larger than about 40°, there are almost no pions with a momentum larger than about 1 GeV/c. Additionally, there are almost no pions with θ larger than 100°. The protons almost all fall withing the angular range of 20° to 60° degrees. This is almost entirely covered by the CDC. Many of these protons will need to be identified by either time-of-flight for the BCAL or using dE/dx in the CDC. Good tracking resolution for high–momentum particles in the backward angle region is not required,
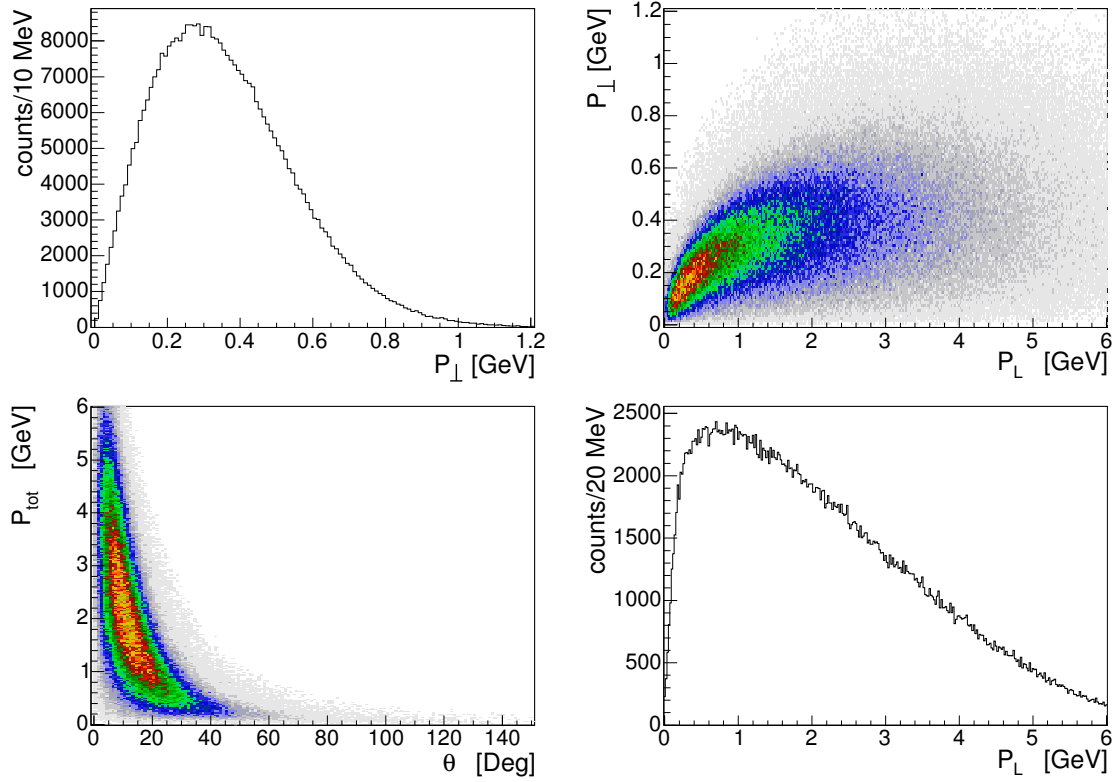
Figure 6.29: The momentum distribution of charged pions from the reaction $\gamma p \to \eta_1(1800)p \to 2\pi^+2\pi^-p$. The upper left-hand figure shows the momentum perpendicular to the beam direction. The upper right-hand figure shows the perpendicular versus the longitudinal momentum. The lower left-hand figure shows the total momentum versus the polar angle θ and the lower right-hand figure shows the momentum along the beam direction.

so the rapid degradation of momentum resolution for these large angles as seen in Figure 6.28 is not a real issue for the detector's overall performance. In addition, most events have at least one particle moving in the forward direction at high momentum. The momentum versus angle for all particles in each event is displayed in Figure 6.29. Good tracking will be needed as close to the beam line as possible, hopefully extending down to $2°$.

Another tracking issue is that many of the charged particles in GLUEX will produce spiraling tracks in the solenoid. Figure 6.31 shows the p versus θ plane for tracks in the solenoid. Tracks which fall above the hyperbolic curve cannot spiral in the $59\,cm$ radius region containing the tracking chambers. Below the hyperbola are a series of approximately horizontal lines. Tracks below these lines spiral the number of times indicated. Based on the p versus θ distributions in Figures 6.29 and 6.30, it is clear that most tracks at angles larger than $50°$ will always spiral at least once in the detector.

Pattern recognition is an important part of track reconstruction as well. This process requires finding local clusters of hits and associating them into small track segments that can be combined into larger tracks. In order for this procedure to work well, it is desirable to have sufficient hits in close proximity such that they will be easily associated. One useful comment on this issue is when the LASS experiment ran in similar conditions, they had severe pattern recognition issues due to the large magnetic field. They resolved it by building chambers with both anodes and cathodes which were read out, with the cathodes and anodes being arranged such that together they provided a 3-dimensional point. The GLUEX detector is trying to build on this experience by reading out both cathodes and anodes in the forward direction. We are also planning packages that consist of six closely spaced planes. Such packages will allow local identification of track
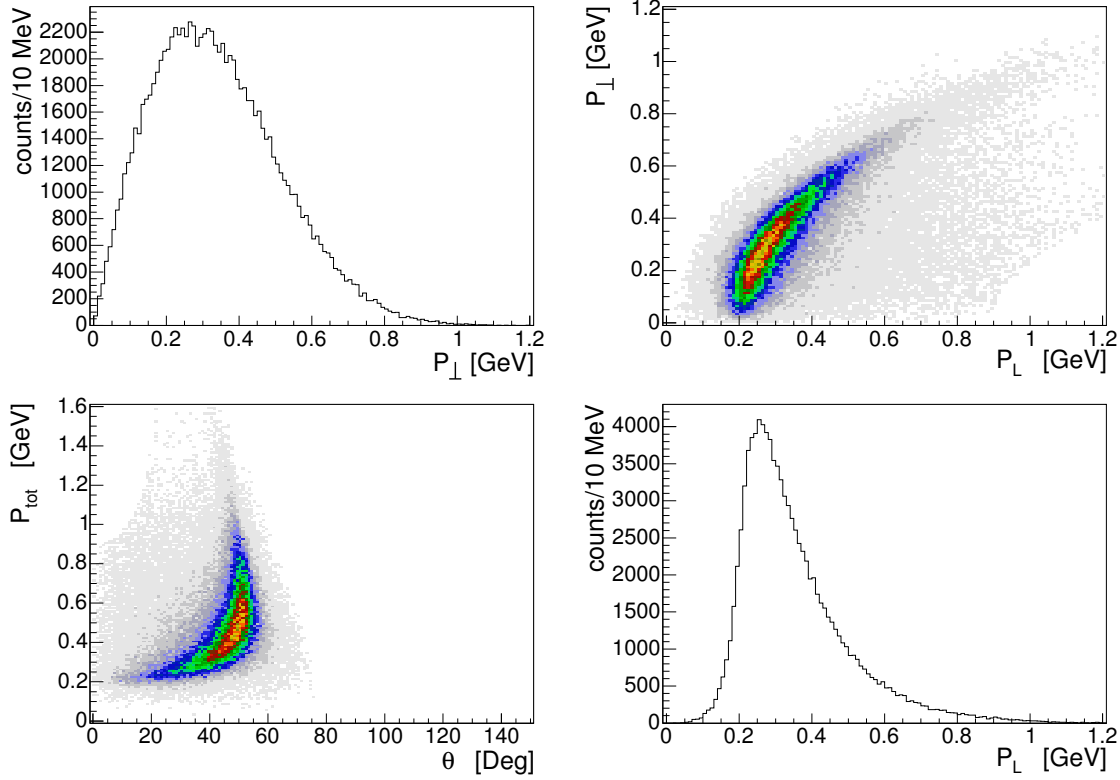
Figure 6.30: The momentum distribution of protons from the reaction $\gamma p \rightarrow \eta_1(1800)p \rightarrow 2\pi^+2\pi^-p$. The upper left-hand figure shows the momentum perpendicular to the beam direction. The upper right-hand figure shows the perpendicular versus the longitudinal momentum. The lower left-hand figure shows the total momentum versus the polar angle θ and the lower right-hand figure shows the momentum along the beam direction.

segments with a reasonable measure of curvature. This has then been repeated four times to provide sufficient segments for high efficiency track-segment linking. In the CDC, the pattern recognition issue is dealt with by creating three sections containing several adjacent straight tube. These are then interleaved with two sets of crossed stereo layers.

The resolution necessary in the photon beam energy has been matched to the expected momentum resolution in the tracking elements of the GLUEX detector. This has been done by looking at the missing mass resolution. As an example, consider reaction 6.10.

$$\gamma p \rightarrow K^+K^-\pi^+\pi^-\pi^0 p \tag{6.10}$$

It is also assumed that the π^0 in 6.10 is not detected. Using the reconstructed charged tracks, the known beam energy, and the assumption that the reaction took place on a proton target, the square of the missing mass is computed and shown in Figure 6.32(a) for a nominal 0.1% beam energy resolution. The distribution is centered at the square of the π mass, but it has a non–negligible width. In Figure 6.32(b) the width of the peak in (a) is plotted as a function of the beam energy resolution. For this particular reaction with a missing π^0, a beam energy resolution of 0.1 to 0.2% is well matched to the $200\,\mu m$ resolution of the tracking system.

6.4.3   Straw-tube Drift Chamber

The straw-tube drift chamber (CDC) is used to track particles coming from the GLUEX target with polar angles between 6° and 155° with optimal coverage from about 20° to 140°, (see
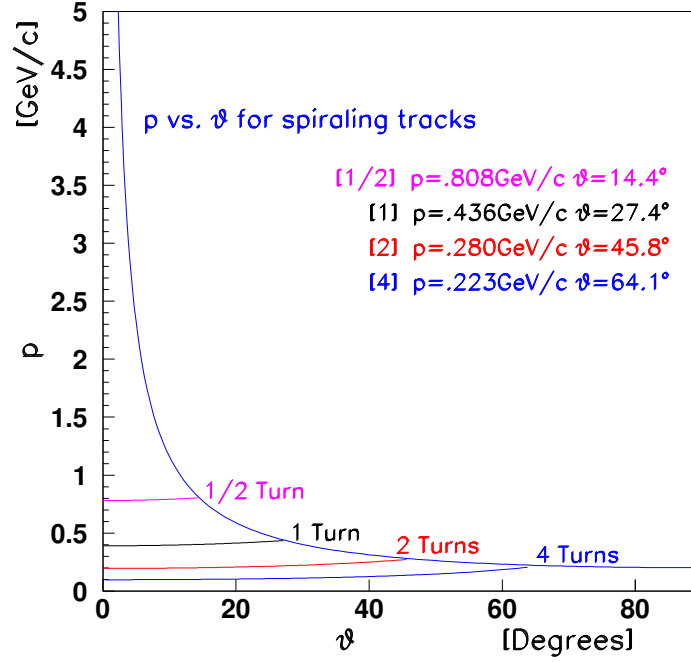
Figure 6.31: This figure shows the number of full circles made by charged particles in the magnetic field. The limit line corresponds to $p_\perp = 0.2\ GeV/c$ tracks. The approximately horizontal lines indicate when the particle can make the indicated number of turns without leaving the magnet.
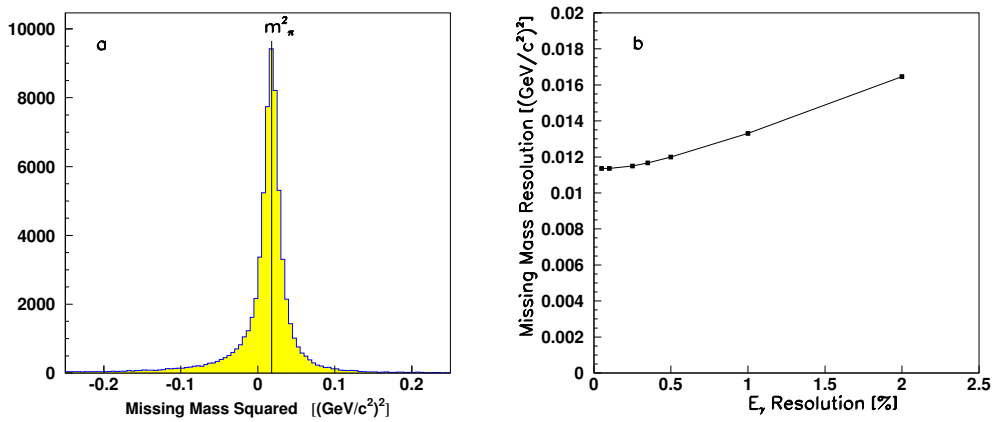

Figure 6.32: Missing mass squared from the reaction 6.10 where the π^0 is assumed missing. (a) is for 0.1% beam energy resolution, while (b) is a plot of the missing mass resolution as a function of the beam energy resolution.

Figure 6.33). Tracks moving more forward than about 20° will be tracked by both the CDC and the FDC systems. These tracks will need to travel through the downstream end plates of the

CDC, so minimizing the material in these plates is extremely desirable. The use of a straw-tube chamber in this region allows us to accomplish this goal as the straws can easily support the $\sim 50\,g$ of tension on each of the 3240 anode wires in the chamber. If one were to go with a wire-cage geometry using field wires, one would need to support about $3000\,kg$ of tension between the the end plates. This would require thick end plates as well as thick shell material at both the inner and outer radius of the chamber. In addition to minimizing material, the straw-tube designs also allows for an extremely well defined electric field through which the ionization drifts. This is especially important given the 2.24 T magnetic field. With straw-tubes, the time-to-radius relation is extremely simple, (see Figure 6.36). In the case of field wires, there are always regions between the field wires where the field is poorly defined. This in turn leads to a significant deterioration in resolution for tracks passing near the edge of such cells.
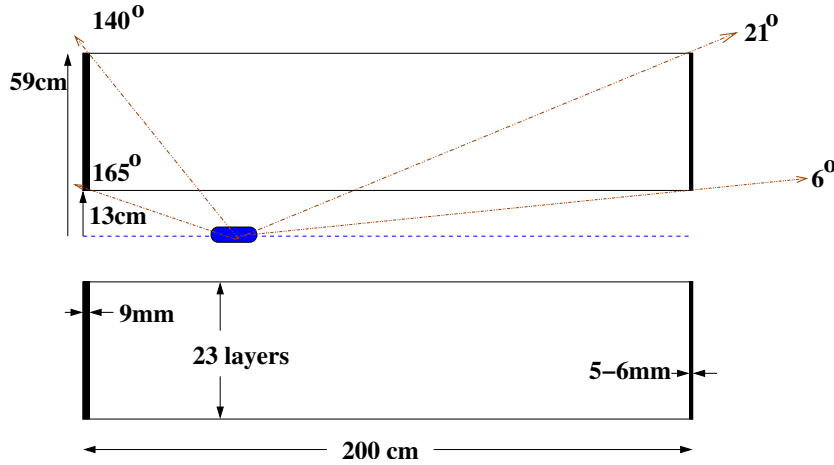
Figure 6.33: A side view sketch of the CDC.
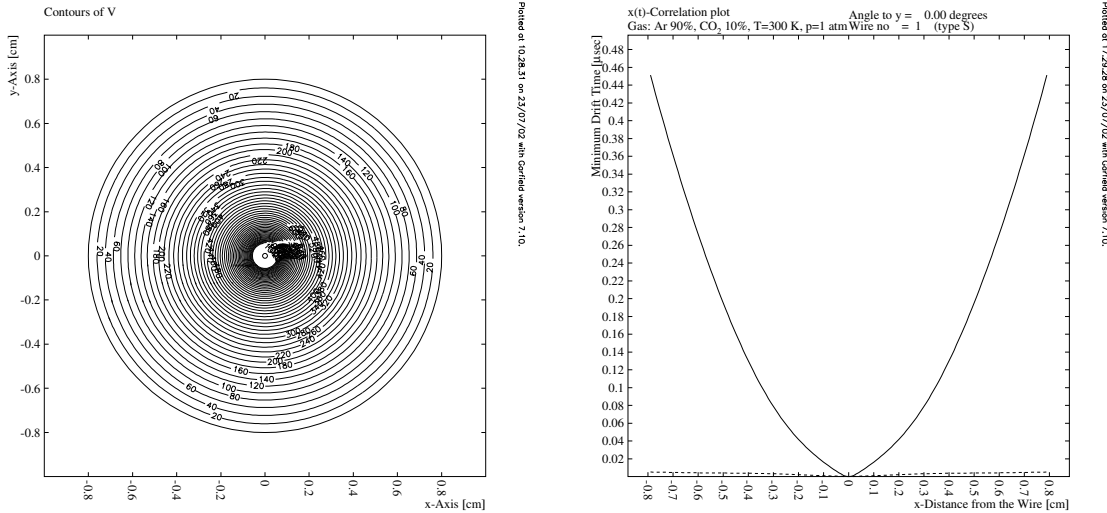
Figure 6.34: The left-hand plot shows a GARFIELD [39] calculation of the electric field in the straw tube. The right-hand figure shows a typical time-to-distance plot calculated for the straw-tube geometry in the 2.24 T magnetic field.

The major disadvantage of a straw-tube design is that it adds additional material in the tracking region. However, by careful use of thin straws, this material can be minimized. An

additional concern is the measurement of dE/dx using straw-tube chambers. This has been done once [40], but is typically not something that straw-tube chambers are asked to do. In order to do this, one has to be able to accurately compute the tracks path length within the ionization volume. Fortunately, the particles for which the dE/dx measurements are to separate πs, Ks and ps whose total momentum is under 0.45 GeV/c. A region where dE/dx does not need to be particularly good to have a big impact.

Table 6.5 lists the material type and approximate thickness of all materials used in the CDC. The upstream end plate is about 9 mm thick aluminum. However, the down stream will be either $5 - 6$ mm thick aluminum or 9 mm thick G10. The minimum thickness of the downstream end plate is controlled by machining that needs to be done to support the stereo layers. However, in addition to the end plate themselves, the feed throughs in the down stream end do not need to be conductive. The use of plastic (DELRIN) will help to minimize the material. The exact choice between aluminum and G10 will be based of structural studies that are currently underway. It is anticipated that in the CDC, the amount of material in the down-stream end plate will be between $\frac{1}{3}$ and $\frac{1}{2}$ of that in the up-stream plate.

Part	Material	Thickness	
		r	z
Upstream End plate	Al		9 mm
Downstream End plate	Al		5-6 mm
	G10		9 mm
Inner Shell	Carbon Fiber	0.7 mm	
Outer Shell	Fiberglass	6 mm	
Upstream Feed Through	Al		1.5 cm
Downstream Feed Through	Delrin		1.0 cm
Wire	Au-W	20 μm	
Straw Tubes	Kapton	100 μm	
	Al	15 μm	
Upstream Gas Plenum	Lucite		5 mm
Downstream Gas Penum	Lucite		3 mm

Table 6.5: The anticipated material to be used to build the CDC. See the text for discussion.

The CDC will contain 3240 straws, each of which is 1.6 cm in diameter and 2 m long. The straws are arranged in 23 layers (see table 6.6). Eight of the 23 layers will be stereo, tilted by ±6° from the straight tubes. The tubes are assumed to have an $r - \phi$ resolution of 150 μm, while resolution along the wire length will be obtained using the 8 stereo layers. This will yield a resolution along the length of the wire of about 150 $\mu m / \sin(6°)$ or about 1.4 mm. The straws will be at ground potential, while the 20 μm diameter gold-plated tungsten wire will be at a positive high voltage between 1.5 and 2.5 kV such that they provide a gain of about 10^4. The exact voltage will depend on the final choice of gas mixture. The wires will be read out only at the upstream end of the detector. This will also minimize material between the CDC and FDC chambers and improve the overall momentum resolution.

We are also considering the possibility of of connecting pairs of wires together on the down stream end and using the effective two-ended readout to provide a charge division measurement. While the resulting z-resolution would be on order of 10 cm, this may be useful in pattern recognition. It would also provide a hardware measurement of the transit time correction in the anode wire. A final decision awaits both completion of the prototype and initial work on pattern recognition software. However, the only impact in chamber design is in the choice of anode wires. A second small design change that may also improve pattern recognition is the arrangement of stereo layers. Table 6.6 shows the two stereo super-layers containing both +6° and −6° layers. Changing them so that all of one super layer of +6° and the other −6° is likely to make track finding in these groups easier. The major concern with this is the mechanical torques extorted by the stereo layers will no longer be completely balanced. A careful engineering study needs

to be done to determine how to prevent an induced twist in the chamber.

Layer	No. of Tubes	Radius cm		Stereo Radians
		Center	Plate	
1	58	14.777	14.777	0.000
2	65	16.559	16.559	0.000
3	72	18.340	18.340	0.000
4	79	20.122	20.122	0.000
5	86	21.905	24.295	0.105
6	93	23.687	25.913	0.105
7	100	25.469	27.552	-0.105
8	107	27.251	29.207	-0.105
9	121	30.816	30.816	0.000
10	128	32.598	32.598	0.000
11	135	34.381	34.381	0.000
12	142	36.163	36.163	0.000
13	149	37.945	37.945	0.000
14	156	39.728	41.094	0.105
15	163	41.510	42.820	0.105
16	170	43.293	44.550	-0.105
17	177	45.075	46.284	-0.105
18	189	48.131	48.131	0.000
19	196	49.913	49.913	0.000
20	203	51.696	51.696	0.000
21	210	53.478	53.478	0.000
22	217	55.261	55.261	0.000
23	224	57.043	57.043	0.000

Table 6.6: Geometrical data about the CDC. There are a total of 3240 straw tubes in the CDC. The listed radii are at the center (length-wise) of the chamber and at the end plates. It should be noted that the stereo wires have a smaller radius at the center than at the end plates.

The choice of gas also plays a significant role in the chamber's performance due to the 2.24 T magnetic field. In order to study this, the GARFIELD program [39] has been used to compute electrostatic properties of the straw tubes, both with and without the magnetic field. The results of this work can be are summarized in reference [41]. Figure 6.34 shows an electrostatic calculation for a tube with the wire well-centered in it. Figure 6.35 shows GARFIELD calculations for two tracks going through a straw tube in three different gas mixtures. The three gas mixtures are Ar(30%)-C_2H_5(20%)-CO_2(50%), Ar(90%)-CO_2(10%) and Ar(50%)-C_2H_5(50%). While in all three cases the time-to-distance relationship is well defined, the longer drift distances of the spiraling tracks introduce a large diffusion contribution to the total resolution. The diffusion resolution, σ_L is also dependent on the gas. Pure argon has an extremely poor resolution, while pure carbon dioxide has a very good resolution. Finally, it is desirable to collect the electrons as quickly as possible. A slow gas, or a very long drift distance can easily push the collection time over a micro second. For this reason, the Argon-Ethane mixture shown in the lower two plots of Figure 6.35 is an inappropriate mixture. Investigations are ongoing to identify mixtures that will satisfy the all of the requirements. To indicate the advantage of good electrostatics, Figure 6.36 shows what happens to the time-to-distance relation as one goes from zero magnetic field to full magnetic field.

In order to achieve the desired 150 μm resolution in the CDC, we need to account for all possible contributions to the resolution. Table 6.7 summarizes these. Clearly the most important is the diffusion term, which depends on the gas. In order to achieve this, a gas mixture that contributes about 120 μm for an average 5 mm drift in a $\sim 2.5\,kV/cm$ electric field needs to be used. Many gas mixtures satisfy this requirement. The next largest contribution is the
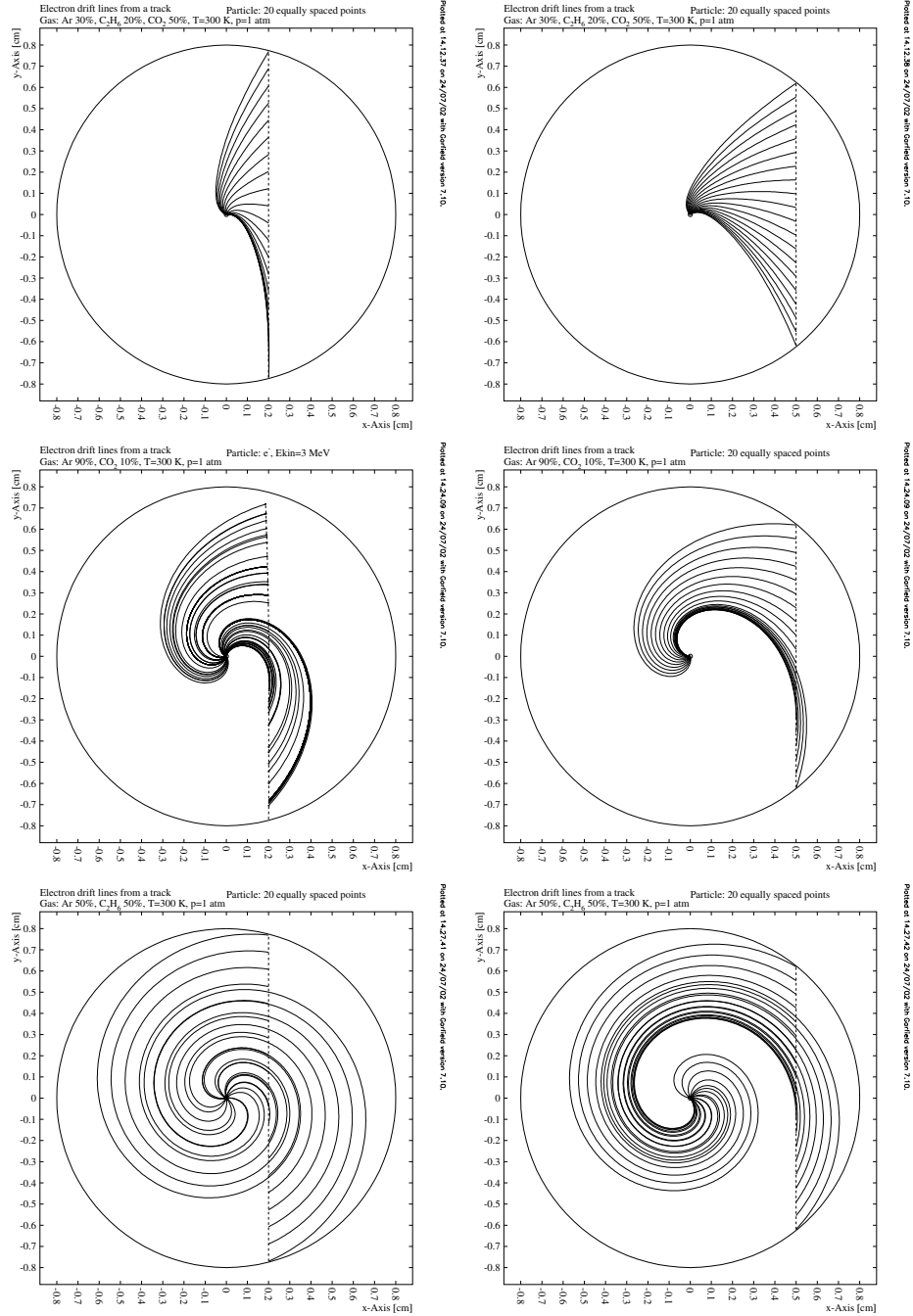
Figure 6.35: Garfield simulations of electrons drifting through a straw tube in the CDC. The curved shape of the tracks is due to the Lorentz angle induced by the 2.25 T magnetic field.

gravitational sag. This scales with the length squared, and will go down if the chamber is shorter than 2 m. The timing resolution of 45 μm assumes that the signal is digitized using 125 MHz flash ADCs and that a timing algorithm that yields times to about $\frac{1}{3}$ of the digitization are used. Time fitting algorithms that are matched to the pulse shape in chambers usually yield intrinsic time resolutions around 20% of the time bin width.

In the construction of the straw-tube chamber, the most technically difficult part involves the stereo layers. Several aspects contribute to this. The holes for these layers need to be drilled
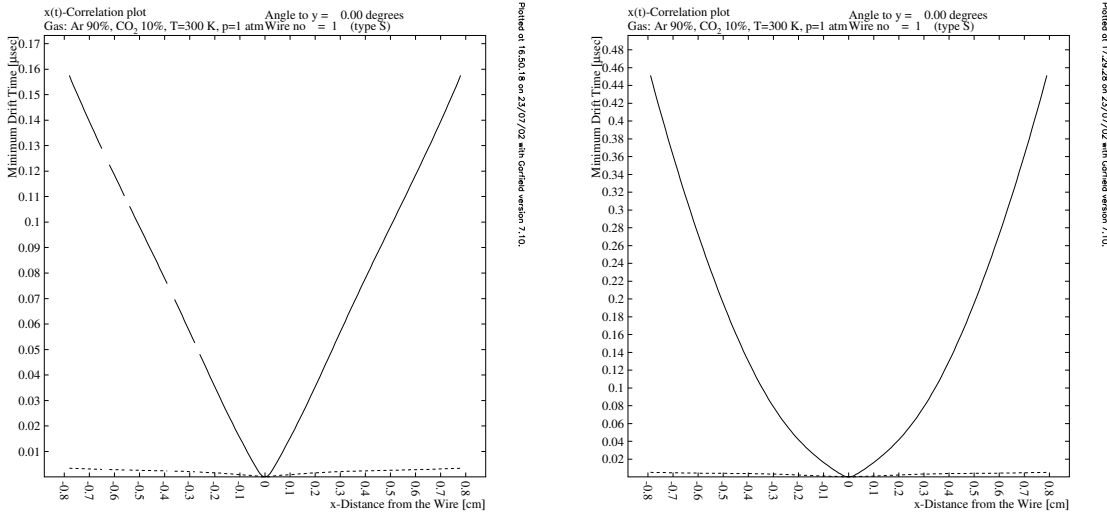
Figure 6.36: Calculated time versus distance in 90% Argon, 10% Carbon Dioxide mixture. **left**: No magnetic field, **right**: full magnetic field.

Effect	Resolution μm
Diffusion σ_L	50 to 200 μm
Geometrical Precision	40 μm
Gravitational Sag	56 μm
Electrostatic Deflection	10 μm
Timing Resolution	45 μm
Quadrature Total	96 to 216 μm
Design Resolution	150 μm

Table 6.7: The estimated contributions to the ultimate chamber resolution from various known effects. These numbers are based on 2 m long, 20 μm diameter, Au-W wires under 50 g tension.

at a layer-dependent compound angle. The outside of the tube inserts need to rest flush against the end plates as shown in Figure 6.37 for both the straight-through and the stereo tubes. Such work either requires a multi-axis CNC machine, or a rotary table stacked on top of three sine plates. This machining also limits the minimum thickness of a plate.

There are also difficulties in mounting the straw tubes for the stereo layers. In the final chamber, the tubes are glued to adjacent tubes in the same layer, and adjacent layers are glued together. In order to do this gluing, clam-shell holders need to be built that match the spacing in each layer and hold the tubes in position while they are glued. For the stereo layer, these clam shells need to be built with the same compound angles as the end plates.

In order to understand the issues involved in the building and operating the straw-tube chamber, the Carnegie Mellon (CMU) group has gone through several steps in prototyping the chamber. They are currently completing a full-scale prototype of $\frac{1}{4}$ of the chamber.

To study the behavior of straw tube chambers, a 2 m long chamber with 2 cm diameter tubes has been acquired from the EVA experiment at Brookhaven [42]. A setup which reads out four tubes in the chamber using a 4-channel digital oscilloscope, and then transfers the data to a local computer for analysis has been built. Signals are produced from a $^{44}Ru_{106}$ source, (see Figure 6.38). The β's from the source are collimated through a 1 mm diameter, 1 cm long tube. The source is placed about 30 cm below the chamber and aligned as shown in the figure. The system is triggered on a signal in the upper tube, and events with signals in all four tubes are read out. Gas mixtures can be varied using a locally built three-component gas-mixing system.
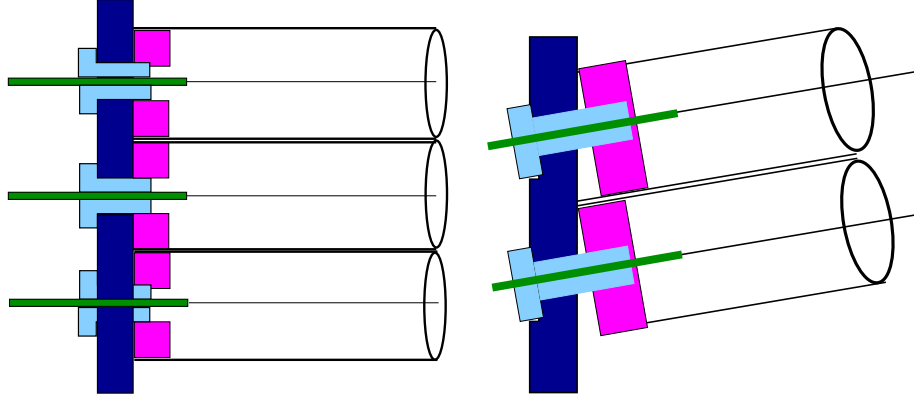
Figure 6.37: Schematic drawings of the feed throughs for both the normal (**left**) and stereo (**right**) wires.

This allows for detailed studies of the chamber performance in different gas mixtures [43].
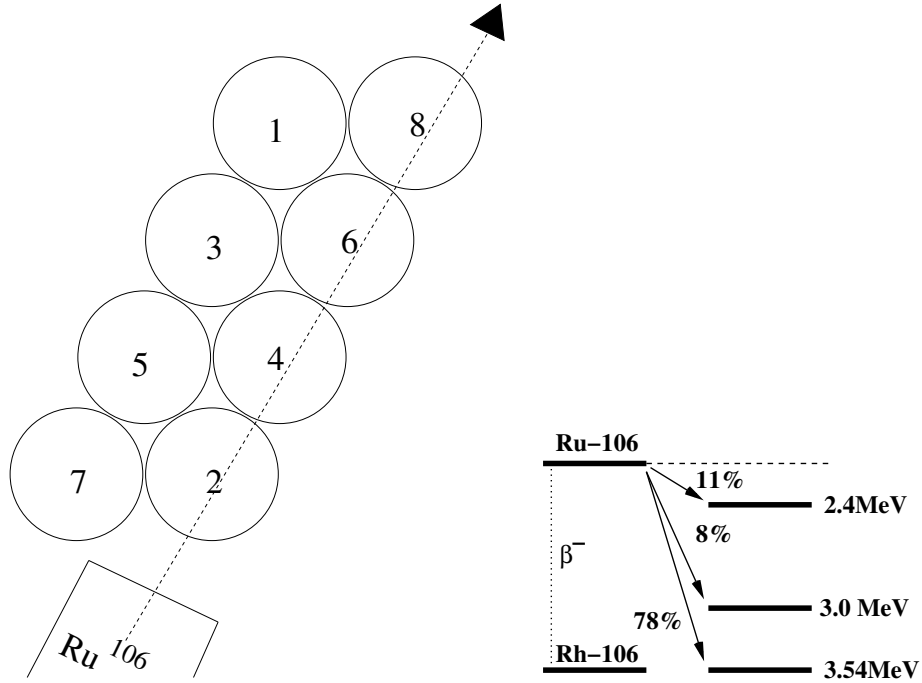

Figure 6.38: Setup of the straw-tube prototype chamber used in studying signals and gas properties. Note the ^{106}Ru source emits primarily 3.54 MeV electrons but there are also up to 1.14 MeV photons.

Figure 6.39 shows signals measured in two different gas mixtures. Currently, there is no way of applying a large magnetic field to the straw tubes. This makes detailed studies of the Lorentz angle only possible through simulation which is currently underway using the GARFIELD [39] program.

In order to build the full-scale prototype, software was written that computes the necessary compound angles at each end plates, and then turns them into machining instructions. An example of the visual output of this program is shown in Figure 6.40 which shows the drilling pattern for the down-stream end plate. Due to the mills available at CMU, two end plate sections each representing $\frac{1}{8}$ of the chamber were made. These were then connected together
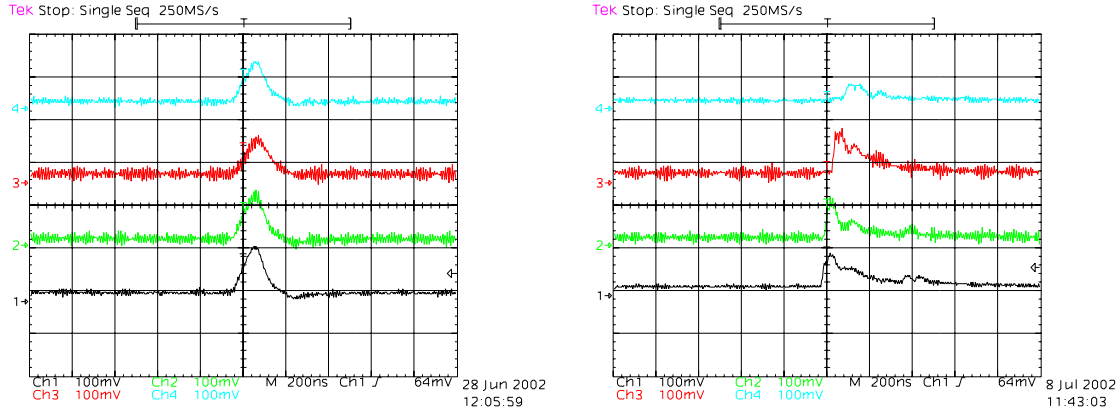
Figure 6.39: Signals observed in the straw-tube chamber for two different gas mixtures. **left**: 50% Argon, 50% Ethane at $2050\,V$ **right**: 90% Argon, 10% Carbondioxide at $1800\,V$.

and the resulting quarter-end-plate sections were sent to JLab to be measured [44]. While this process led to a number of improvements in the construction technique, it was finally concluded that maintaining sufficient accuracy over eight sections that needed to be connected together would probably not be possible, and it would make more sense to contract out the end plate fabrication to industry.
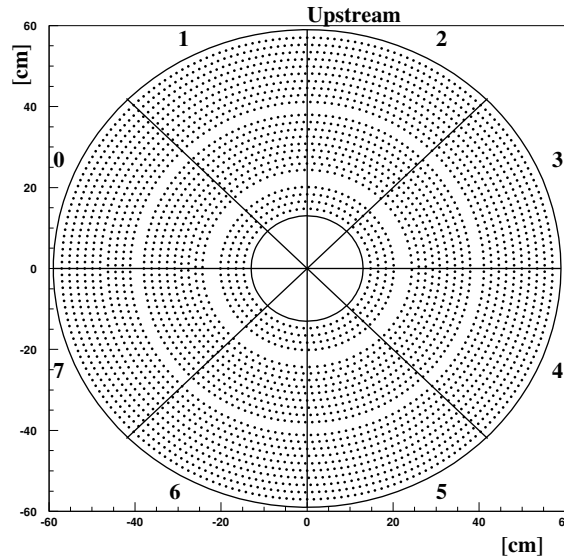
Figure 6.40: The position of the 3240 holes that need to be drilled in the downstream end plate of the CDC. The gaps in radius after layers 4 and 13 are due to the layers just beyond these being stereo wires.

An problematic issue that is common with straw-tube chambers is the conductive glue joints that both hold the straws to the feed throughs as well as the feed throughs to the chamber end plates. Careful examination of an existing straw tube chamber from the Brookhaven EVA experiment showed that all of these joints tend to develop leaks over time. In order to try to alleviate this leak problem, a detailed study of many conducting and non-conducting epoxies was carried out to see if a good glue could be found. The conclusion of this work was that the particular choice of glue did not matter. Instead, the act of inserting one part of a feed through

into another part tended to scrape much of the epoxy off the contact surface. This led to a joint with many weak spots that over a short period of time, developed leaks.

Upon careful study of this, it was decided that the only way to guarantee a good glue connection was to develop a system in which one is certain the the glue is actually making solid contact with both surfaces. The result of this is a feed through system as shown in Figure 6.41. The *donut* is a small tube with a small *glue trough* machined into its perimeter. From one end of the donut, a small *glue port* is drilled from the outside to the *glue trough*. Once the donut has been inserted into the straw tube, a known amount of conducting epoxy can be injected through the *glue port* into the *glue trough*. The strength of the resulting glue joint is solid, independent of the tested epoxies. In fact several test sells have maintained several psi overpressure for nearly nine months without leaking.

Into the donut, it is necessary to glue the insert that both holds the straw tube the chamber end plate and holds the crimp pin. In order to guarantee a good glue joint between the donut and the insert, a small *glue lip* has been machined on the tip of the insert. If a uniform coat of glue is applied to the outside of the *insert*, then when it is inserted into the donut, the epoxy tends to collect in both the *glue lip* and between the *insert* and the chamber end plate. Exactly where we need it to guarantee a good epoxy seal. Using these specially designed feed through systems, we are able to obtain a conducting gas-tight joint with all conducting epoxies that we have tried.
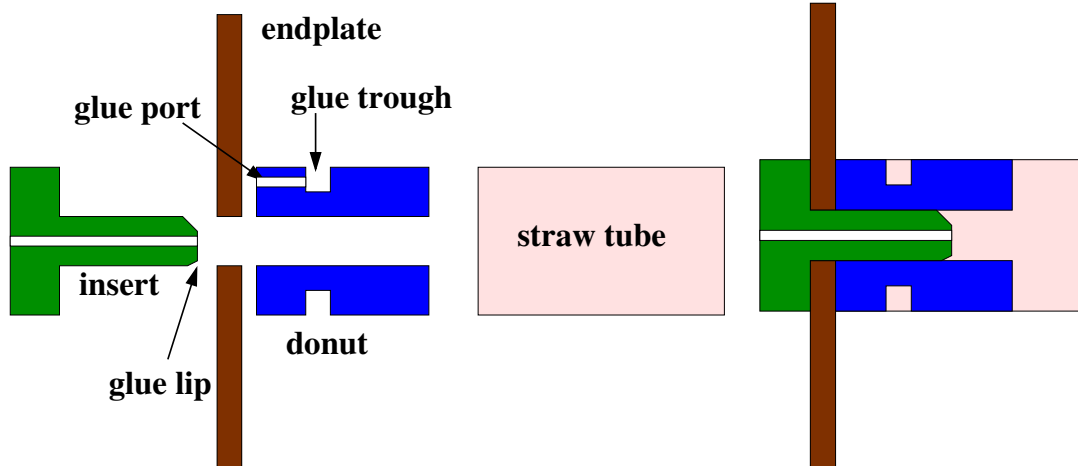
Figure 6.41: The CMU designed feed throughs which provide a solid glue joint between the straw-tube and the end plate. The left-hand figure shows an expanded view, while the right-hand shows the feed throughs in the chamber end plates.

Figure 6.42 shows several photographs of the prototype straw-tube chamber being built at CMU. Four tubes per layer are being put into this chamber, with particular emphasis on making sure that we have both the transition from straight to stereo and from stereo back to straight layers. During construction, wire tension has been carefully monitored. Summaries of tests that have been performed during the construction of the CDC can be found in reference [45].

6.4.4   Forward Drift Chambers

The Forward Drift Chamber system (FDC) is used to track charged particles coming from the GLUEX target with polar angles up to 30°. Tracks at angles greater than 10° also pass through the CDC detector and its associated downstream endplate. Due to the spiraling trajectories of the charged particles and the high multiplicity of charged tracks passing through the FDC, it is crucial for this system to be able to provide a sufficient number of measurements with appropriate redundancy to enable linking of the hits from the different tracks with high accuracy, while providing good spatial resolution with reasonable direction information. Current studies
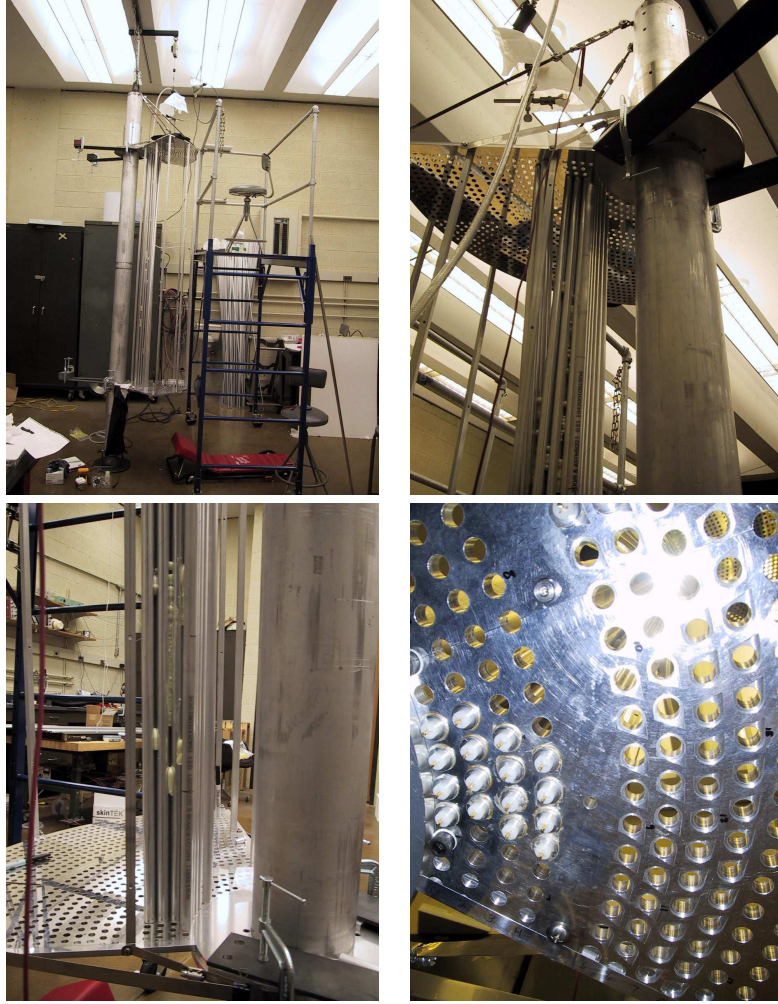
Figure 6.42: The upper-left picture shows the prototype chamber suspended and in position to string wires. The upper-right picture shows several partial layers of tubes glued into the prototype CDC. The lower-left picture shows the same tubes at the lower plate. The lower-right picture is taken from under the lower plate showing several crimped wires in the chamber.

with the *HDFast* Monte Carlo program indicate that track hit coordinates should be measured to an accuracy of 150 μm in order to achieve the desired momentum resolution for the charged tracks in the final state.

In the current detector design, the FDCs include four separate but identical disk-shaped planar drift chambers (MWDC's) as shown in Fig. 6.27. Each package will include six layers of alternating anode and field-shaping wires sandwiched between planes of cathode strips. The total thickness of each package is estimated to be roughly 0.15 gm/cm^2. Neighboring wire planes will be rotated by 60° with respect to each other in order to improve track reconstruction decisions on the corresponding anode wire left/right ambiguities, hence improving the overall resolution. By charge interpolation of the electron avalanche image charge in the cathode strip readout, spatial resolutions at the cathode planes are expected of better than 150 μm.

The orientation of the cathode strips on either side of the wires has yet to be decided. The optimal resolution of the hit coordinate along the wire direction is obtained when the cathode strips are perpendicular to the anode wires. In this configuration there is no quantization of the position measurement resulting from the discrete nature of the anode wires (i.e. the cathode measurement in the coordinate perpendicular to the wires simply locates the wire position). The

issue of the optimal electrode configuration for the FDC chambers will ultimately be answered for GLueX from studies of a prototype cathode readout chamber that is currently being tested at Jefferson Laboratory (discussed later in this section). In the current FDC system design, the cathode strips on either side of the anode plane are arranged in a U and V geometry at $\pm45°$ with respect to the wires. This technique of employing a stereo angle may prove valuable in separating and assigning multiple hits within a chamber to the different tracks.

The basic chamber element is a disk of outer radius 60 cm, where the wires are strung as cords across the chamber as shown in Fig. 6.43. With a wire-to-wire spacing of 5.0 mm, each chamber plane will contain 119 anode wires. In addition, there will be double this number of cathode strips on each cathode plane. This amounts to 595 channels per FDC chamber element and 3570 channels per FDC chamber package.

The cathode readout as presently planned will employ 125 *ps* F1 TDCs for the anode wire drift time readout and 125 MHz FADCs for the cathode readout. This would enable commonality with the readout electronics planned for the other GLueX detector subsystems. Note that with a clock rate of 125 MHz on the FADCs, time fitting algorithms matched to the chamber pulse shape can be employed to provide a time resolution of ∼2 ns (amounting to ∼40% of the time bin width). This timing information from the cathode signals would aid in pattern recognition of multiple tracks passing through the chamber volume. We are also exploring options with FADCs with slower clock rates. This could in principle reduce the electronics costs significantly if we can accept the poorer time resolution.
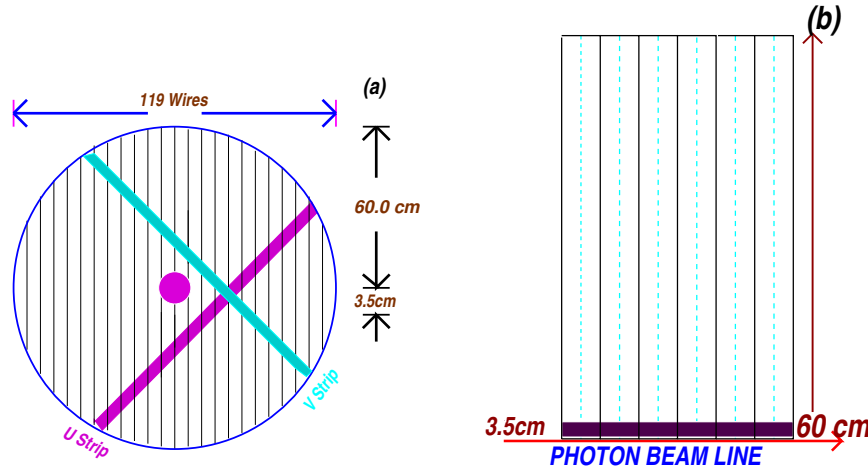
Figure 6.43: A front (a) and side (b) sketch of an FDC package. In (a) the wires are schematically indicated as the vertical lines. The U cathode strips are in front of the wires and the V cathode strips are behind the wires. The field-shaping wires are not shown. In (b) a side view of the upper half of a six-chamber package is shown. The wire planes are shown as the dashed lines, while the cathode planes are shown as the solid line. Ground planes between adjacent chambers are not shown.

The wires that cross through the beam line require special treatment to handle the otherwise unmanageable rates. Several possibilities are currently being considered. The first is to deaden the wires out to a radius of ∼3.5 cm by placing a material such as Styrofoam around them or to include support structures around the beam line to remove the wires entirely from this vicinity. The final decision will be based on background and design studies.

The primary development issues associated with the FDCs that must be addressed are factors affecting the intrinsic resolution of the chambers, along with the mechanical and electronics layout. The goal is to construct a tracking detector that meets the required design specifications and has a long life time, a uniform and predictable response, a high efficiency, and is serviceable

in case of component failure.

FDC Monte Carlo Studies

The initial specifications for the layout of the FDC system have been studied within the framework of the *HDFast* Monte Carlo. The goals of these studies were to consider the basic number of FDC chamber packages within the solenoid and to consider the number of wire planes per package.

For these studies, pions with momenta between 0.25 and 4.0 GeV and angles from 5-10° were generated and the momentum uncertainty in the form of $\delta P/P$ was studied as a function of momentum. Fig. 6.44(a) shows results comparing a 3-package vs. a 4-package configuration (with packages equally spaced along the beam line). Here the preliminary results make it apparent that the single track resolution, if all cathode and anode positions can be resolved to 150 μm, is improved by roughly a factor of 2 (for pion momenta above 2 GeV/c) with the 4-package configuration. Although the resolution decreases with increasing momentum, it worsens at a noticeably slower rate for the 4-package configuration. The tracking system design parameters can be met with such a 4-package configuration. However, it is the redundancy that the fourth package provides that will be crucial in disentangling multiple charge particle hits and background within the readout time window.

Fig. 6.44(b) shows results for a 4-package FDC system with each package containing either 4, 5, or 6 wire planes. Here the 4-layer design yields a resolution about 20% worse than for the 5 and 6-layer designs. Although the resolution of the 5 and 6-layer packages are about the same, the 6-layer design has been shown to improve pattern recognition for multiple hits within a chamber.
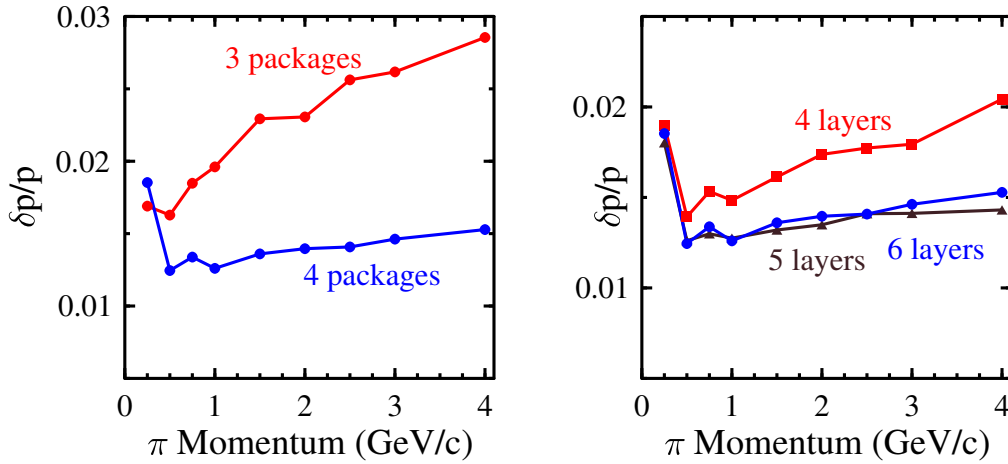
Figure 6.44: Monte Carlo studies comparing the FDC resolution in (a) a configuration with three packages vs. four packages and (b) a 4-package configuration with 4, 5, and 6 wire planes per package.

At the present time the Monte Carlo work is proceeding in earnest to perform detailed systematic studies of the FDC design with realistic backgrounds in the chambers. This will enable final decisions to be made regarding the number of chamber packages, the number of wire planes, the optimal rotation between neighboring planes, the number of cathode strips and their segmentation, and the optimal z-positions of the chambers. Also note that as discussed in Section 6.4.1 for the CDC, the final z-extent of the straw tube chamber has not been finalized. In this case and others, the design of the CDC and FDC systems must be considered in concert. Of course the final resolution for charged tracks is firmly connected to the design and performance of *both* the CDC and the FDC tracking packages.
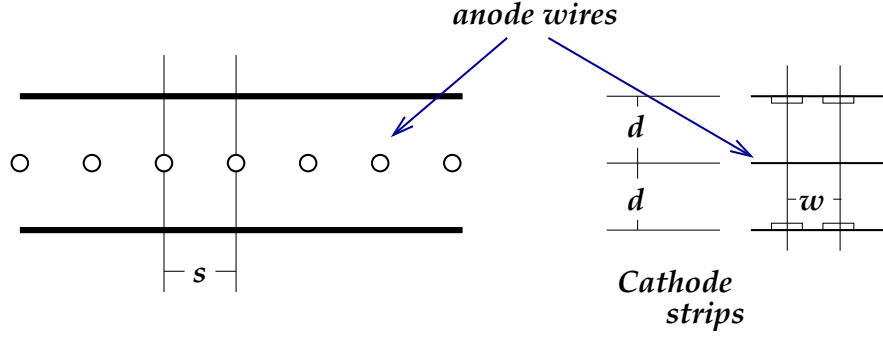
Figure 6.45: Schematic diagram of a typical cathode strip chamber.

Cathode Strip Chambers

Cathode strip chambers (CSC) are typically multiwire proportional chambers (MWPCs) with a symmetric drift cell in which the anode-cathode spacing d is equal to the anode wire pitch s (see Fig. 6.45). In these chambers the spatial resolution of the anode readout is limited to roughly $s/\sqrt{12}$ (RMS). In a CSC the precision coordinate is obtained by measuring the charge induced on a segmented cathode by the electron avalanche formed on the anode wire as shown in Fig. 6.46(a). For the case of multiple tracks, a second segmented cathode rotated at an angle with respect to the first cathode can also help to reduce multi-hit ambiguities as shown in Fig. 6.46(b). The stereo technique is superior to the alternative of reading out only one cathode plane and a hit wire number in that multiple hits on a single wire may be resolved.

The optimum cathode readout pitch w is determined by the width of the induced charge distribution. It has been shown by several groups that minimal differential non-linearity ($\sim$1%) is achieved when $w/d \approx 1$ (e.g. [46]). This ratio is employed in the current FDC design, although optimization studies are underway with our prototype cathode chamber. Other groups [47] have been able to construct cathode chambers with larger w/d ratios while maintaining acceptable resolution and minimal differential non-linearity by using intermediate strips between cathode readout nodes that are capacitively coupled to their adjacent readout strips as shown in Fig. 6.47. This option, which can significantly reduce the associated readout costs, is also being considered in the FDC design studies.

Simulations from Ref. [46] have shown that resolutions of 25 μm for the precision coordinate in a CSC could be achieved for minimum-ionizing tracks if the electronics and readout could be provided with noise and inter-channel gain variations of less than 0.5% of the nominal pulse height. The primary factor limiting the spatial resolution of a cathode chamber is the electronic noise of the preamplifier. Other factors such as the uncertainty in the gain calibrations and cathode plane distortions should also be considered as well. The precision in the determination of the position of the induced charge depends linearly on the signal-to-noise ratio. Note that preamplifier noise is dominated by the input capacitance and that optimal capacitive coupling requires that the inter-strip capacitance be much larger than the capacitance of a strip to ground [47]. Operation within a realistic experimental environment will result in resolutions much closer to our design goal of 150 μm.

An interesting question regarding cathode chambers is the change in system resolution when they are also employed as drift chambers (MWDCs), specifically horizontal drift chambers. The principles of operation of a MWDC are such that the best position resolution is achieved when the first electrons that reach the anode wire drift along field lines in the plane of the wires. If we consider a GARFIELD calculation [39] of the field lines for such a chamber (see Fig. 6.48(a)), the first electrons to reach the anode wire will most certainly arise from other locations within the drift cell. This gives rise to non-linearities in the space-time correlation that strongly degrade the position resolution. In order to improve the field configuration for the MWDC operation, field-shaping wires can be included within the anode plane between each anode wire. This can
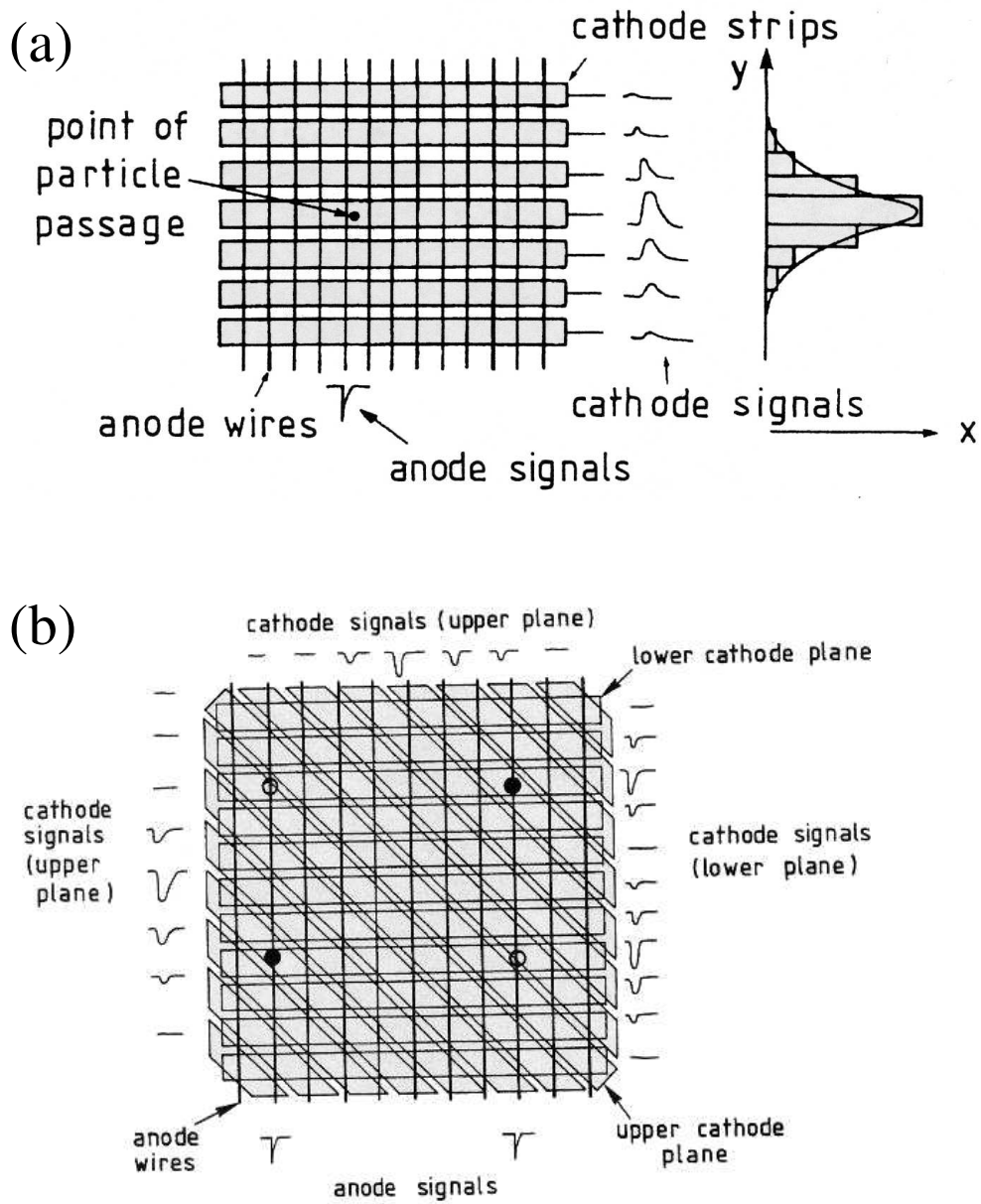
Figure 6.46: Illustration within a typical MWPC of (a) the cathode readout and (b) the resolution of ambiguities within a CSC for two particle hits.
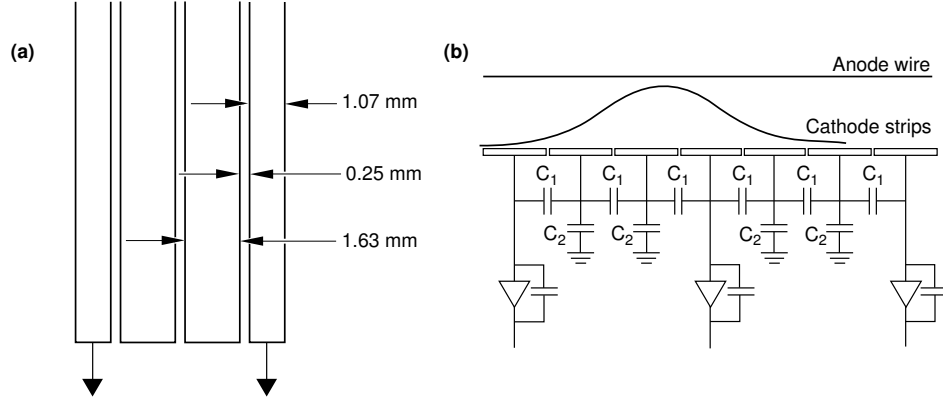
Figure 6.47: (a). CSC layout with a modified cathode strip layout using readout and intermediate strips (from the ATLAS detector). (b) The equivalent circuit highlighting the capacitive interpolation using the two intermediate strips.

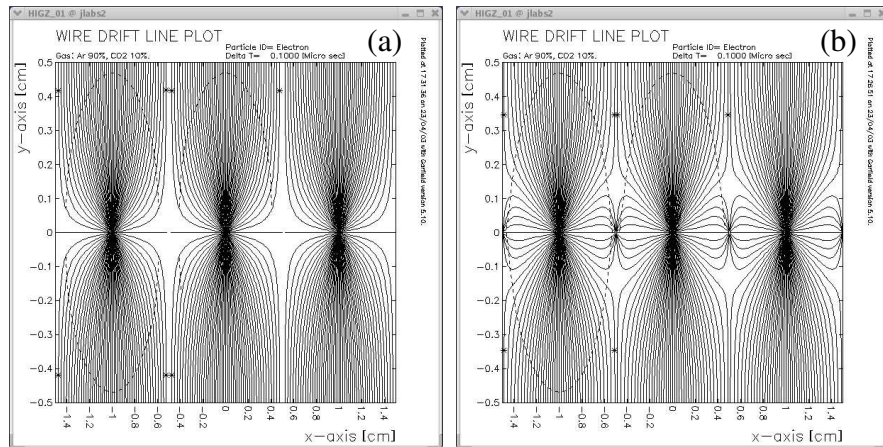clearly improve the field configuration as shown in Fig. 6.48(b).

Figure 6.48: GARFIELD calculations of electric field lines (for a $B = 0$ field configuration) within a square drift cell for a 90% argon - 10% CO_2 gas mixture for electrode configurations without (a) and with (b) field-shaping wires.

It is not known at the current time how inclusion of field-shaping wires will affect the cathode position resolution. One of the central questions that we are investigating through our R&D program for the FDC system regards the optimal electrode structure in our cathode chambers. Specifically we are seeking to fully understand the trade-offs between timing resolution from the wire planes and spatial resolution from the cathode planes. However, with inclusion of the field-shaping wires and maintaining a square drift cell, in order to achieve optimal resolution, the number of cathode strips on each cathode plane increases by a factor of two relative to an anode wire only plane design.

The basic algorithm to determine the cathode position of the charged track is to fit the charge distribution across the cathode plane. This amounts to determining the position of the center of gravity using the ratio of the first and second moments of the charge distribution on the plane of the strips from [47]:

$$x_{c.g.} = \frac{\sum_{i=1}^{N} x_i q_i}{\sum_{i=1}^{N} q_i}, \qquad (6.11)$$

where N is the number of strips involved, $x_i = iw$ is the strip coordinate, and w is the pitch of the cathode readout. If the charges q_i on each strip are measured with an RMS error of σ, then with $Q = \sum_i q_i$, the uncertainty in $x_{c.g.}$ is given by:

$$\sigma_{c.g.} = \frac{\sigma}{Q}\sqrt{2\sum_i x_i^2} \tag{6.12}$$

or

$$\sigma_{c.g.} = \frac{\sigma}{Q}\sqrt{2w^2 + 2(4w^2) + 2(9w^2) + \ldots} \tag{6.13}$$

Therefore the resolution depends on the number of strips used. Monte Carlo simulations and operational experience from different groups have shown that the optimum number lies between three and five strips. The position resolution is poor when only one or two strips are present as there is not enough information, while it increases slowly when more than five strips are used. The resolution function in this case also includes the additional electronic noise from each strip. Here there must be an optimization of chamber resolution factoring in the desire to minimize the number of readout channels to contain costs.

Resolution Effects

Resolution degradation of cathode chambers comes primarily from two sources, tracks inclined from the normal to the face of the chamber and Lorentz angle effects. In both cases the spatial resolution is degraded because the avalanche charge is distributed non-uniformly along the anode wire due to the energy loss fluctuations in the gas. The cathode position resolution is optimum when the avalanche is formed at a single point along the wire. A finite spatial extent of the anode charge results in a resolution degradation $\mathcal{D}$. Studies of the PHENIX cathode chamber [48] have shown that $\mathcal{D}$ goes as:

$$\mathcal{D} = 0.16d\tan\theta, \tag{6.14}$$

where d is the anode-to-cathode spacing and θ is the angle from the normal to the face of the chamber.

Skewed or non-local charge distributions along the anode wire can also be caused by a Lorentz force along the anode wire from the presence of magnetic field components that are not collinear with the electric field of the chambers. The Lorentz effect itself does not result in a systematic shift of the measured coordinate in the cathode plane. It simply results in a degradation of the resolution because of the spread of the charge along the wire.

Gas Considerations

There are several basic requirements that need to be met by the chamber gas that will be used for the FDC system. These include a high drift velocity (50-60 μm/ns), low Lorentz angle ($< 10°$), and for safety, we much prefer a non-flammable mixture. It is important to understand that the performance of a cathode chamber in terms of cathode position resolution is reasonably insensitive to the exact values of the gas parameters. Here variations of the drift velocity or non-uniform drift velocities as a function of E/p (i.e. electric field/pressure) are relatively unimportant. For the same reason, the cathode readout operation is immune to modest variations of temperature and pressure. Variations in gas gain on the order of 20% do not strongly affect the cathode resolution since a relative charge measurement in adjacent strips is involved.

However, the gas mixture and its control are essential to consider carefully for the operation of the MWDC. In order to enable accurate calibrations of the drift times, it is essential that the gas mixture is stable, which amounts to constructing a gas handling system that carefully controls the gas mixture, as well as hall controls to fix the temperature and relative humidity as much as possible.

Detailed studies of chamber performance will be performed with our prototype cathode chamber employing various gas mixtures. A number of gas mixtures have been studied by various groups that have proven suitable for cathode chambers. Most of these gases contain CF_4 in combination with isobutane (C_4H_{10}) or CO_2. The Lorentz angle is similar for each gas and is about 5° at 0.5 T magnetic field. One chamber-safe gas mixture that has worked well with the PHENIX cathode chambers consists of 30% argon, 50% CO_2, and 20% CF_4 [48].

Readout Electronics

The primary design issue for the front-end electronics for the FDC system is to maintain a signal-to-noise ratio of better than 100:1 in the presence of a large detector capacitance. Capacitance measurements in detectors are very important because they serve to determine the performance of the detector in terms of the charges induced on the cathodes, gain variations, detector efficiency, etc. They also play an important role in determining the characteristics of the readout electronics. For the FDC chambers the dominant contribution to the capacitance seen by the preamplifiers will be the strip-to-strip capacitance. The capacitance between adjacent strips is given approximately by [48]:

$$C(pF/cm) = 0.12t/w + 0.09(1+k)log_{10}(1 + 2w/s + w^2/s^2), \qquad (6.15)$$

where t is the strip thickness, w is the strip width, s is the strip separation, and k is the dielectric constant of the backing material (here it is envisioned to be kapton). For the FDC design that is presently considered, this capacitance is roughly 1 pF/cm. Accounting for the total capacitance of the system then forms a basic requirement for the input capacitance for the front-end electronics performance. An additional concern for this design is the coupling of the signals between adjacent strips. Studies of the PHENIX CSCs have shown that appropriate setting of the integration times of the electronics is important to decrease sensitivity to distortions in the induced charge distribution due to inter-strip coupling.

The chamber-mounted electronics for the cathode strip readout will consist of a charge-sensitive preamplifier that drives a pulse-shaping amplifier. The pulse shape will be chosen as a compromise between noise and pileup, both of which degrade the resolution. The electronics must also be designed to minimize cross-talk, particularly to non-adjacent channels. R&D efforts related to selection of the preamplifier and pulse-shaper are just now beginning. However we expect to develop contacts with outside groups who have more experience. We will also work with the Fast Electronics group at Jefferson Laboratory to explore potential options. The preamplifier circuits employed for the prototype cathode chamber employ the same preamplifiers used with the CLAS drift chambers. This choice was made mainly for convenience, and their performance will provide a benchmark for comparison.

FDC Cathode Chamber Prototype

The FDC prototype cathode chamber has been designed primarily to provide us experience with cathode strip chambers. Through detailed study of this prototype we hope to be able to better understand which electrode structure and layout will fulfill the design requirements for the final FDC chambers. The prototype will also provide important insights into the mechanical design, tolerances, construction and assembly techniques, noise immunity, and calibrations that will be important for the final FDC detector design. Some of the elements of the FDC prototype design have descended from the cathode chambers employed in the original LASS spectrometer [49].

A schematic of the FDC prototype chamber is shown in an exploded view in Fig. 6.49. The basic chamber layout consists of two cathode planes with strips oriented at ±45° sandwiching a single wire plane. The gas volume is defined by two outer aluminum frames that each include an aluminized mylar window. The active area of the prototype chamber is roughly 20 cm × 20 cm, and the chamber is about 8 cm thick.

The test chamber has purposefully been designed to act as a test bed for any number of electrode configurations. So far we have wound wire planes consisting only of anode wires
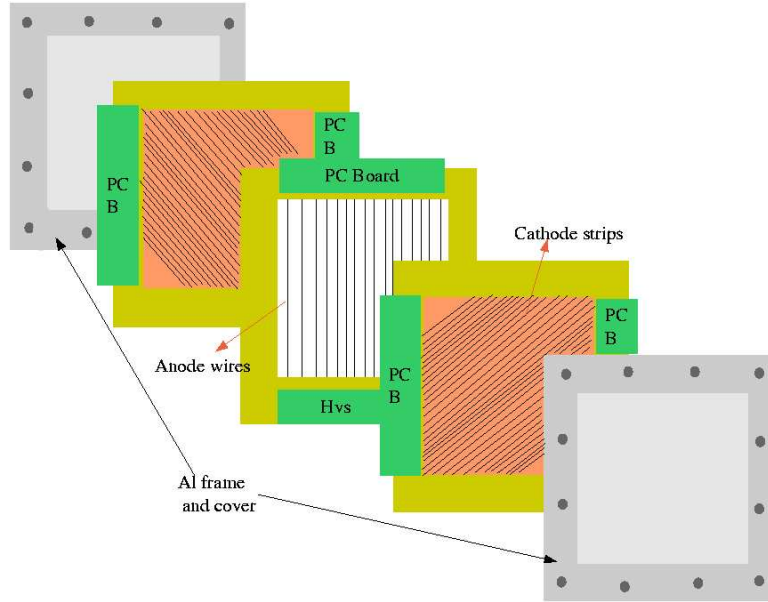
Figure 6.49: Schematic representation of the FDC prototype chamber in an exploded view showing the wire plane, two cathode planes, and the two aluminum window frames.

and planes consisting of alternating anode and field-shaping wires. We have also designed cathode planes of varying rotation angle, varying cathode strip pitch, and varying cathode strip separations. Ultimately each configuration will be studied in order to come to an understanding of the optimal electrode structure for our purposes.

The U and V cathode planes are mirror symmetric with respect to each other. The cathode planes are copper-clad kapton sheets (~ 2 mil thickness) mounted onto 5-mm thick G10 frames. The chamber is designed to operate with the anode wires at positive high voltage, the field wires at negative high voltage, and the cathode strips at ground.

The printed circuit board for the wires was designed to capacitively decouple high voltage from the signals and to route the signals to the output connector. The printed circuit board for the cathodes routes the signals directly to the output connector. The basic circuits on the boards are shown in Fig. 6.50. Small signal routing circuit boards attach to the output connectors on the wire and cathode circuit boards and contain the preamplifiers for each readout channel. The output connects to a shielded twisted-pair line that routes the signals to the readout electronics (FASTBUS 1877 TDCs and 1881 ADCs). The signal readout boards used for the cathodes are essentially the same as those used for the anode wire readout. The only difference in the design is a polarity switch of the cathode signals before sending the signals to the amplifier and the ADC.

Each readout channel has its own associated "SIP" preamplifier. These single-channel transimpedance preamplifiers were originally designed for the Hall B CLAS detector. They have complementary outputs designed to amplify signals by a factor of 2.25 mV/μA. Besides high gain, characteristics of the SIPs include: fast rise and fall times (3 to 4 ns), wide frequency bandwidth, wide dynamic range, and low noise and power dissipation (65 mW).

In total the prototype chamber includes 16 20-μm diameter sense wires alternated with 80-μm diameter field wires, with a wire-to-wire separation of 5 mm and a strip-to-strip separation of 1 mm. The cathode planes are located 5 mm away from the wire plane. They each include 32 copper strips with a pitch of 5 mm. Three different sets of U and V cathode planes have been designed with strip separations of 0.25 mm, 0.50 mm, and 1.0 mm to allow for the optimal configuration to be determined. Presently the chamber is operating with a 90% argon - 10% CO_2 gas mixture. Photographs of the prototype cathode chamber and the cathode plane itself
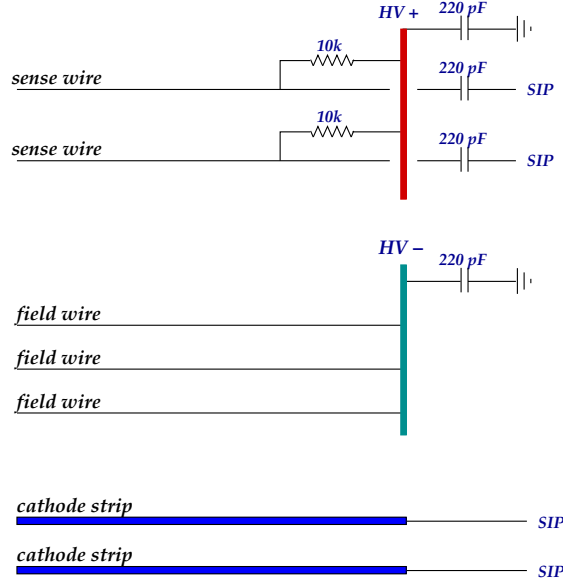
Figure 6.50: Circuit board electronics for the sense and field wires, along with the cathode strips.

are shown in Fig. 6.51.

A set of 19 wire chambers have been borrowed from IUCF in order to assemble a cosmic ray test stand at Jefferson Laboratory. This test stand is being used to define tracks through the FDC prototype chamber. A schematic drawing of the layout of the cosmic ray test stand is shown in Fig. 6.52. This system employs multiple layers of drift chambers above and below the FDC prototype chamber to precisely define the trajectory of an incident charged particle track that can be used to compare against the position measured in the FDC prototype. The configuration of the test stand includes two X layers and two Y layers above the FDC prototype and a matching set of four layers below. This system, once properly calibrated, should be capable of defining a track to roughly 200 μm at the location of the FDC prototype. A photograph of the test setup is shown in Fig. 6.53.

At the present time the cosmic ray test stand has been crudely calibrated and we have succeeded in getting readout of the cathode chamber. A look at the first anode and cathode signals from this chamber is shown in Fig. 6.54. So far the detector is operating quite nicely and an initial characterization of its performance and resolution is in progress.

Based on the results of studies of the first cathode chamber prototype, as well as continued Monte Carlo studies of both the detector and the physics, we will begin working on the design for a second prototype for the FDC system. One of the primary purposes of the second prototype chamber will be to test mechanical support designs for the full-scale chamber and wire planes. This is necessary to avoid electrostatic instabilities and non-uniformities that are known to affect resolution. To illustrate the issue at hand, the gain $\mathcal{G}$ in a proportional counter is given in general by:

$$\mathcal{G} = Ke^{CV}. \tag{6.16}$$

For an operational voltage V, the gain is dependent on the capacitance of the detector C. Thus any variation on the flatness of the cathode plane changes the capacitance of the detector and hence the gain. It also creates field non-uniformities that affect the cathode position resolution. For gain variations of less than 5%, a rough calculation shows that the cathode plane must have less than a ± 5 mil flatness variation.

Various schemes have been employed by different groups to provide mechanical support for the cathode planes in large area chambers. For example, in the so-called *Plug Chambers* used
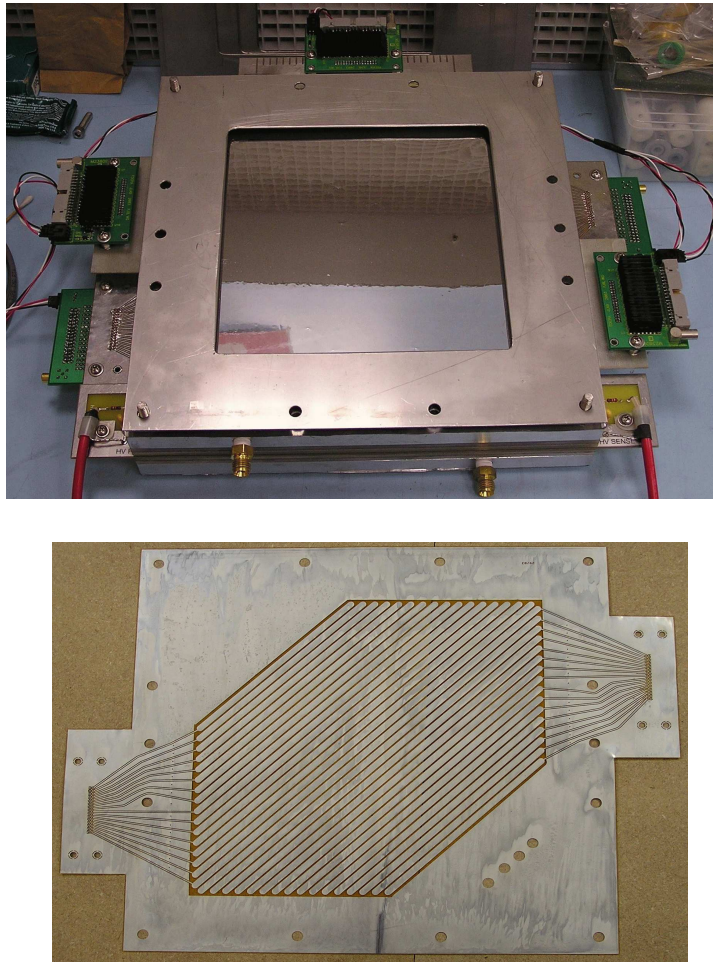
Figure 6.51: (Top) Photograph of the prototype FDC cathode chamber constructed to optimize chamber electrode structures. (Bottom) Photograph of a cathode plane showing the cathode strips.
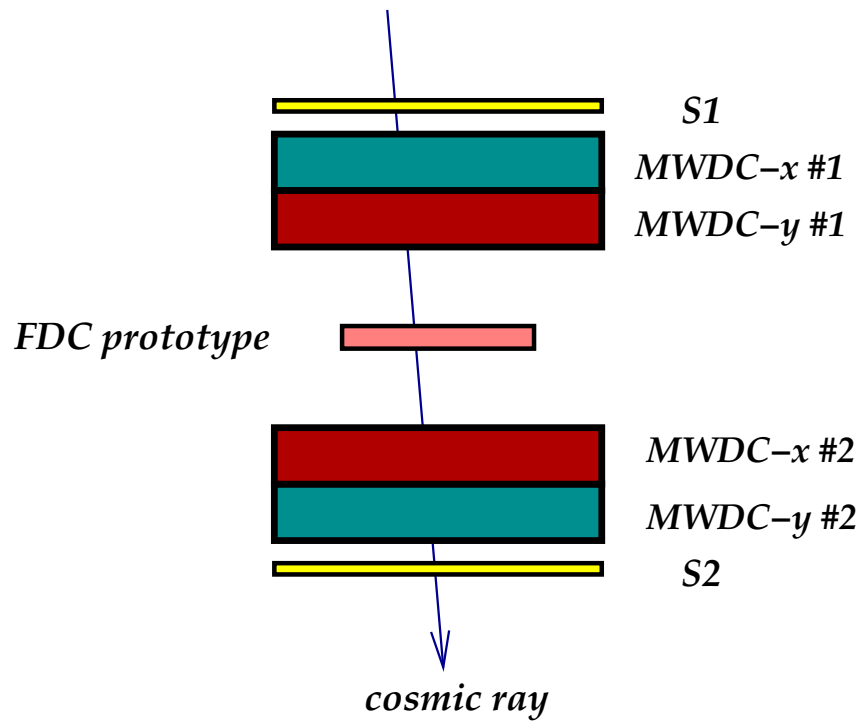
Figure 6.52: Schematic drawing of the cosmic-ray telescope used for FDC prototype resolution studies.

Figure 6.53: Photograph of the cosmic ray test stand set up at Jefferson Laboratory to study resolution characteristics of the cathode strip chambers.
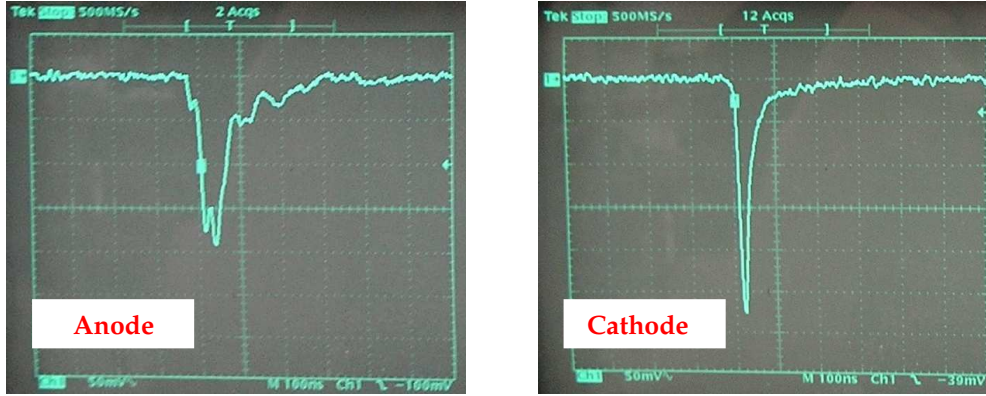
Figure 6.54: Anode (left) and cathode (right) signals from our prototype cathode strip chamber. The electrode structure and layout of this prototype is expected to be very similar to the final FDC design.

in the LASS experiment [49], polyurethane spacers were epoxied onto the cathodes to fix the anode-cathode gap spacing. This and other options are currently being explored.

Another important role for the second prototype chamber is to give us a design test bed for the circuit boards associated with both the cathode and wire planes. We will again seek out contacts with other groups who have constructed chambers of similar design as well as work with the Fast Electronics Group at Jefferson Laboratory in order to minimize R&D lead times.

6.4.5 The Start Counter

The START counter will provide a fast signal which is used in the level–1 trigger of the experiment. For this purpose the time resolution cannot be worse than 4 - 5 ns. As an element of the level–1 trigger, this detector needs an excellent solid angle coverage and a high degree of segmentation for background rejection. Using tracking information the start counter will be able to provide a time resolution of better than 0.5 ns thus allowing us to identify the electron beam pulse associated with the event.

The start counter will consist of a cylindrical array of 40 scintillator paddles (see figure 6.55). The scintillators have a thickness of 5 mm. This will provide a good light output and therefore a good timing signal. The downstream side of the scintillators will be bent toward the beam line in order to increase the solid angle coverage while minimizing multiple scattering.

Each paddle will be coupled at the upstream end to a light guide leading out of the very high magnetic field region. Photo-tubes which can be operated in magnet fields of the order of one to two kilo gauss will be used for readout. Tests with the Hamamatsu system H6614 have shown that the required time resolution can be achieved routinely. As scintillation material we plan to use Eljen Technology EJ200 which is fast and has a large absorption length. The time resolution (σ) for a EL204 scintillator bar, directly coupled to a H6614-01 system, is shown in figure 6.56 as a function of distance from the PMT.This detector is similar to the start detector currently used in CLAS in HALL B at Jefferson Lab.

6.5 Particle Identification

6.5.1 Overview

Particle identification in the GLUEX detector (i.e., the separation of pions, kaons, and protons) will incorporate information from at least four different subsystems – two subsystems in the central region and two in the forward region.
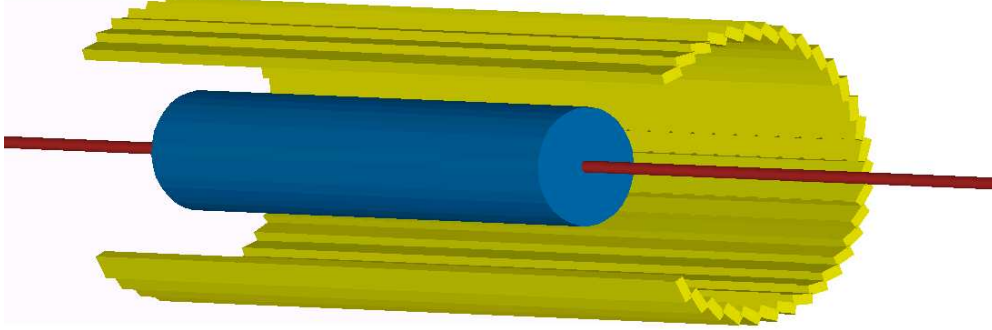
Figure 6.55: C........... design of the start counter surrounding the target with ....lindrical array of scint...........
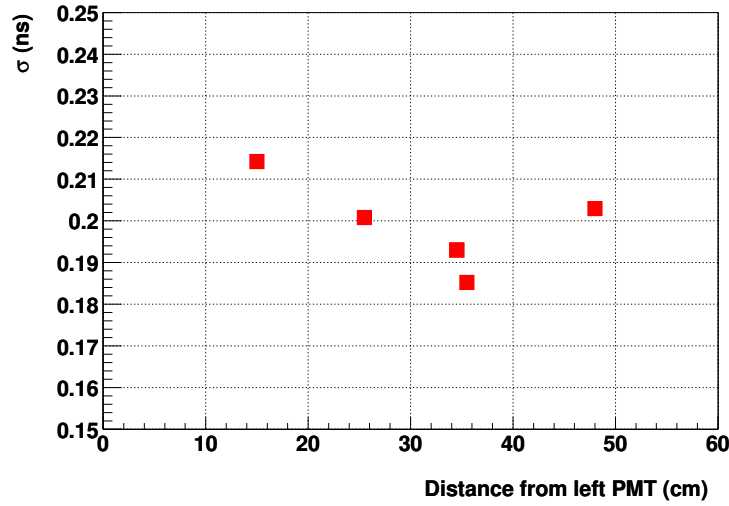

Figure 6.56: The Start Counter time resolution (σ) as a function particle trajectory position along a EJ204 bar with the dimensions $0.5 \times 3 \times 70cm^3$.

1. Low momentum central tracks will be identified using dE/dx measurements from the Central Drift Chamber (CDC).

2. A time of flight measurement from the barrel calorimeter (BCAL) will also provide identification information for central tracks. The CDC and the BCAL working in conjunction will provide an excellent means for identifying recoiling protons from the target.

3. Higher momentum forward-going kaons and pions will be distinguished using a Cerenkov detector. Two possibilities for this detector exist – a threshold gas option (CKOV) using C_4F_{10}, and a Quartz-based DIRC option; each will be discussed in detail in a later section.

4. Time of Flight (TOF) information for forward-going tracks with momenta less than around 2.5 GeV/c will be provided by a scintillator wall 500 cm downstream of the target.

Once information is gathered from each of these four elements, the information will be combined into likelihoods in order to provide a unified way of making a particle indentification decision. The likelihood method will be discussed in section 6.5.4.

To illustrate the overall features of the particle identification, consider the reaction $\gamma p \rightarrow K^*\bar{K}^*p$. This reaction has kinematics that are typical of the reactions to be studied by the GlueX experiment. The $K^*\bar{K}^*$ system is produced peripherally with a t dependence of e^{-10t}. The proton recoils predominantly in the central region with a momentum below 2 GeV/c. The central kaons from the K^* decays range in momentum up to 5 GeV/c; central pions range up to 3.5 GeV/c. Forward kaons and pions have higher momenta, in general, than those in the central region, kaons ranging up to 7 GeV/c, and pions up to 5 GeV/c.

$$\gamma p \rightarrow K^*K^*p \rightarrow K^+K^-\pi^+\pi^-p$$
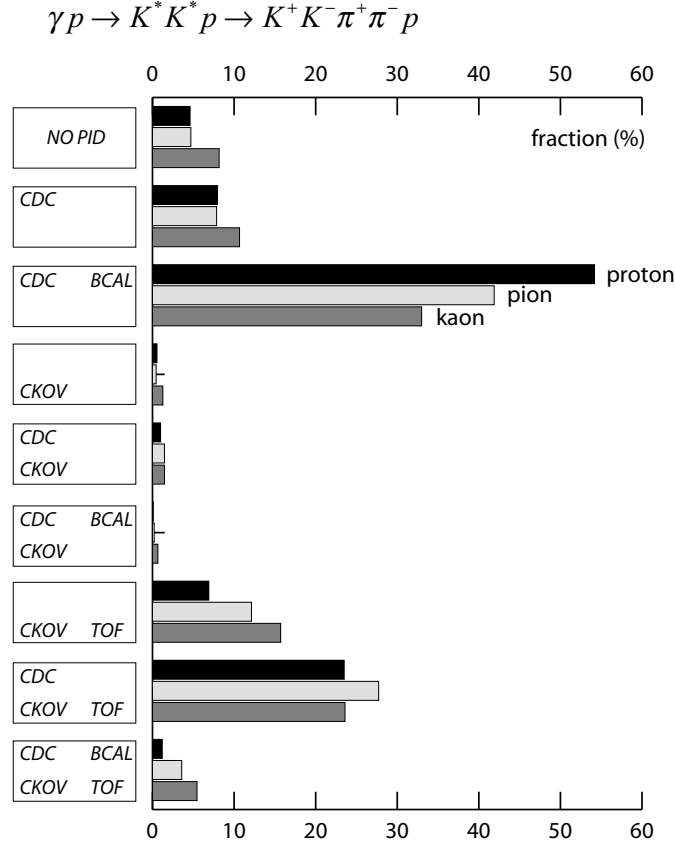
Figure 6.57: The fraction of tracks from the reaction $\gamma p \rightarrow K^*\bar{K}^*p$ detected by different combinations of particle identification elements.

Each of the five tracks in the final state can be categorized according to the particle identification elements it encounters. Figure 6.57 shows the percentage of tracks from $\gamma p \rightarrow K^*\bar{K}^*p$ encountering each of the eight possible combinations of PID detectors. Cases 1 (CDC) and 2 (CDC,BCAL) are purely central tracks; cases 6 (CKOV,TOF) and 7 (CDC,CKOV,TOF) are the dominantly forward tracks. Notice that the proton usually lands in the central region, and larger fractions of the pions and kaons go forward.

In the central region, the CDC and BCAL effectively work together to identify the recoiling proton. Figure 6.58 shows the momentum spectrum of the central protons from $\gamma p \rightarrow K^*\bar{K}^*p$ overlayed with K/p and π/p separations from the CDC and BCAL. For the dE/dx measurements from the CDC, an Argon-based gas was assumed and the resolution was estimated to be 10%. A 250 ps time resolution was assumed for the BCAL, and a typical path length of 2 m was used for the figure. The entire range of the central proton momentum spectrum is well covered. Protons in the forward region also have low momenta and are easily identified by the TOF wall.

Central Proton Identification
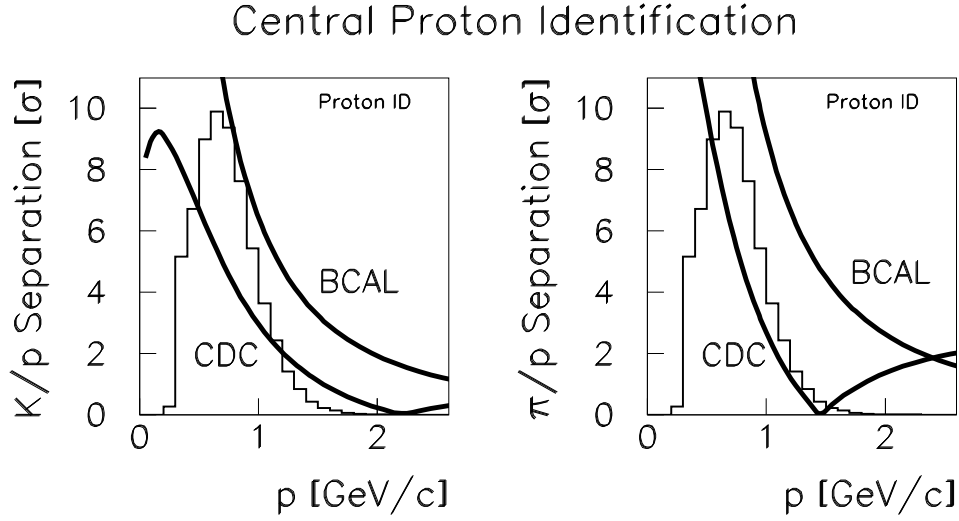
Figure 6.58: Identifying protons in the central region of the detector. The left plot shows K/p separation; the right shows π/p. The histogram in each is the momentum distribution for central protons from the reaction $\gamma p \to K^* \bar{K}^* p$. The curves are estimates of the separating power (in numbers of sigma) of the CDC dE/dx and the BCAL time of flight measurements.
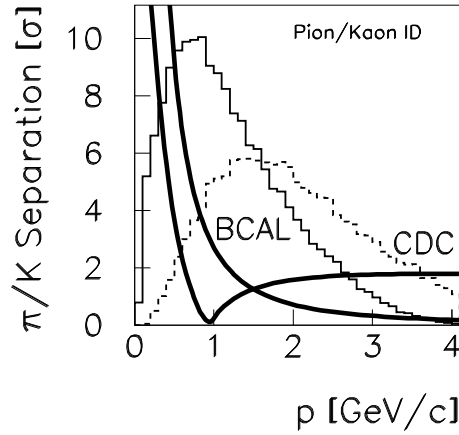
Central Pion/Kaon Identification

Figure 6.59: Identifying pions and kaons in the central region of the detector. The solid histogram is the central pion momentum spectrum; the dashed histogram is the momentum spectrum of central kaons. The curves are estimates of the separating power (in numbers of sigma) of the CDC dE/dx and the BCAL time of flight measurements.

In addition to the recoiling proton, however, a fraction of the pions and kaons in the reaction $\gamma p \to K^* \bar{K}^* p$ end up in the central region. Figure 6.59 shows estimated π/K separation curves (using the same detector parameters as above) overlayed on the pion and kaon momentum
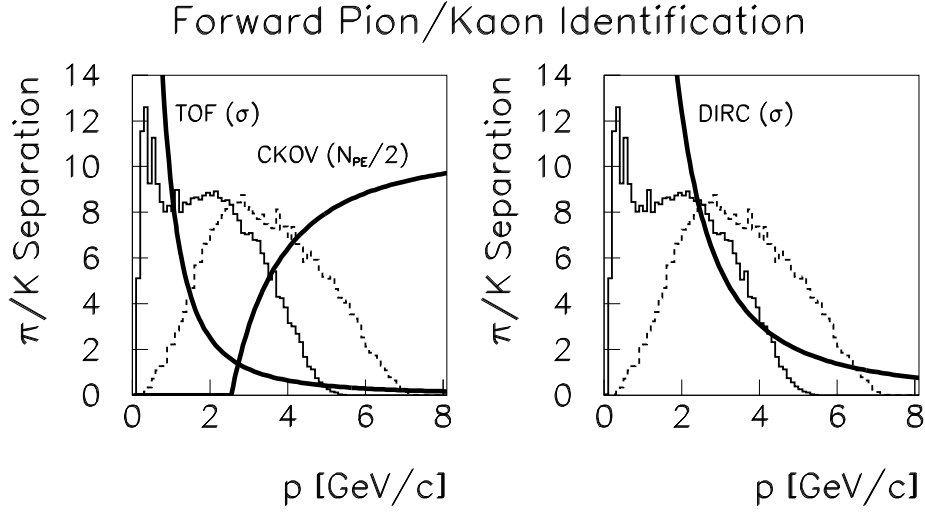
Figure 6.60: Identifying pions and kaons in the forward region of the detector. The left plot shows the gas Cerenkov option; the right plot is for the DIRC option. In each case, the solid histogram is the forward pion momentum distribution; the dashed is the forward kaon distribution. The curves of the left plot are the estimated π/K separations of the TOF and CKOV systems. The TOF π/K separation is expressed in numbers of sigma; the CKOV performance is plotted as the number of expected photoelectrons divided by two. The right plot shows the DIRC π/K separation in numbers of sigma. (Note the TOF will be used in conjunction with either option but is shown only in the left plot.)

distributions. Some fraction of the higher momentum tracks cannot be identified, but the strong separations in the forward region compensate.

The momentum spectra of forward-going pions and kaons from the $\gamma p \to K^* \bar{K}^* p$ reaction are shown in Figure 6.60. These will be identified by a time of flight measurement from the forward TOF wall in conjunction with either a gas Cerenkov system (CKOV) or a DIRC. The expected π/K separations from each option are overlayed on the momentum spectra. Typical TOF parameters were used in generating the time separation: a detector time resolution of 70 ps, a typical flight length of 5.0 m, and a conservative momentum resolution of 1% and length resolution of 1% added on when projecting different particle hypotheses to the wall.

The performance of the gas Cerenkov system is expressed in terms of the average number of photoelectrons, N_{pe}, for π mesons traversing 80 cm of C_4F_{10} gas with index of refraction $n = 1.0015$. The momentum threshold for π and K mesons are 2.5 and 9.0 GeV/c respectively and the light yield per radiator length is given by:

$$\frac{dN_{pe}}{dx} = N_o \cdot \sin^2 \theta_c = N_o \cdot \left(1 - \frac{1}{\beta^2 n^2} \right) \tag{6.17}$$

and since $n \approx 1$, in the relativistic limit $\beta \to 1$:

$$\frac{dN_{pe}}{dx} \approx N_o \cdot 2 \left(n - 1 \right) \tag{6.18}$$

N_o is the figure of merit of a Čerenkov counter taking into account all efficiencies in the system and for a counter of reasonably good design $N_o \approx 90 \; cm^{-1}$. Based on this, the average photoelectron yield for the Čerenkov counter will be about 21 in the relativistic limit.

The gas Cerenkov option leaves a significant gap in momentum where the π/K separation is restricted. The TOF separating power falls below 3 σ at a momentum near 2 GeV/c, while the pion threshold in the C_4F_{10} gas is 2.5 GeV/c.

The DIRC option, on the other hand, will use a higher index of refraction (Quartz) to make a measurement of the Cerenkov opening angle:

$$\cos\theta = \frac{1}{\beta n} \qquad (6.19)$$

The estimated π/K separation of figure 6.60 assumed a resolution on the opening angle measurement of 2.1 mrad. More details on the DIRC will be given in a later section.

Required Design Parameters For the Čerenkov counter, assuming that the inefficiency for detection is given by $e^{-N_{pe}}$, then the efficiency for detecting pions exceeds 95% when the π momentum is above 3 GeV/c. At this momentum the TOF difference is about 210 ps. For 95% (3σ) efficiency to separate pions and kaons with the TOF at this momentum, the time resolution, σ_t should be less than about 70 ps.

dE/dx in the chambers

As described above, there is a subset of the low momentum charged particles which will not reach a time of flight counter, or will reach them after spiraling so many times in the magnet that the TOF information will be very difficult to use. For these particles, dE/dx information from the CDC chamber will be the primary source of identification. Fortunately, these particles all have momenta smaller than about 450 MeV, which is exactly where dE/dx will work the best. This detector has been discussed in an earlier section.

6.5.2 The Time-of-flight System

Barrel Time-of-flight Measurement

The design of the barrel calorimeter is dictated primarily by the available space inside the magnet and the method chosen for photon conversion. Charged particles emitted at large angles to the beam often have low velocity so even moderate time resolution is sufficient to distinguish pions from kaons. The lead/fiber design of the barrel calorimeter provides a large number of scintillator samples as a particle traverses the individual fibers. The KLOE collaboration has demonstrated [50] an RMS time resolution of 252 ps for minimum ionizing particles traversing 19 layers of lead and fiber. This value will be used as an estimate of the performance that can be achieved in the TOF measurement from the calorimeter in HALL D. This detector has been discussed in an earlier section of this report.

The Lead Glass Forward Calorimeter

Located just upstream of the forward electromagnetic calorimeter. the LGD, and downstream of the Čerenkov counter will be the forward time-of-flight system, the TOF. The goal of the forward TOF is to separate $K^{\pm}$ from $\pi^{\pm}$ among forward-going charged particles. The TOF will also provide a forward multiplicity count to be used in the level-one trigger.

Assuming a momentum resolution of about 1% and a particle path length resolution of 1% an overall TOF time resolution of 80 ps should allow for K/π separation at the 3σ level up to a momentum of 2.5 GeV/c. The TOF will consist of two planes of scintillation counters, each 2.5 m long, 6 cm wide and 1.25 cm thick. Each counter will be read out at both ends. The counters in one wall will be oriented perpendicular to the other wall. The the total module count is 84 modules and the total channel count is 168 for the number of FADC's, constant fraction discriminators and TDC's.

The scintillator bars need to be 2.5 m long to cover the active regions of the Čerenkov counter. The 6 cm width of the bars is set by the requirement that the overlap of charged particles from the same event at the TOF in any one bar be acceptably small ($< 2\%$). From Monte Carlo simulations of $\gamma p \to K^* \bar{K}^* p$ it was found that a 6 cm width satisfies the occupancy requirement. (We studied four reactions, but are most vulnerable to this one because of its low

Q value.) Specifically we find a probability of 0.22% that two charged particles go through just one bar in both the front and back planes. The thickness of the scintillation bars, the dimension along the beam direction, is set by the requirement that sufficient light be produced to meet the time resolution requirements, while at the same time minimizing the amount of material in front of the LGD.

Prototype Studies

Extensive prototype studies have been carried out to optimize the TOF system design. Data using scintillation bars of various dimensions and manufacture and various phototubes were collected using a cosmic ray test facility at Indiana University. Data were collected in several data runs with hadron beams at the Institute for High Energy Physics (IHEP) in Protvino, Russia. During the data runs we also explored the possibility of using Čerenkov light in Plexiglas (non-scintillating) bars to exploit prompt Čerenkov light to build a TOF system. Results of the IHEP tests have been presented at various instrumentation conferences and publications [51, 52, 53, 54]. Further beam tests at IHEP are planned using 2.5 m scintillator bars with four elements in each of two walls in early 2005.

Cosmic Ray Test Facility   Figure 6.61 shows part of the cosmic ray test facility. A large light-tight box was prepared to accommodate a 2-m long scintillator bar and a cosmic ray telescope consisting of two small scintillation counters that can be positioned along the bar. The scintillation bar under test is read out at both ends with Phillips XP2020 PMT's and their signals are read into separate channels of a TDC and ADC. Trigger electronics use signals from the telescope to define the passage of a cosmic ray particle and define the start signal for the TDC and gate for the ADC.

Figure 6.61: Part of the cosmic ray test facility showing a light-tight box inside of which is a 2-m long scintillator bar, read out at both ends, as well a trigger telescope with two small scintillation counters that can be positioned along the bar.

Measurements Made in a Hadron Beam at IHEP   Several data runs testing TOF prototype modules were made at the IHEP accelerator. The setup for these runs is shown in Figure 6.62. The two bars under test were coupled to PMTs T1 through T4 at their ends. The bars could be moved transverse to the beam. We define x as the position of the center of the long scintillator relative to the beam with x=0 at the center of the bar.
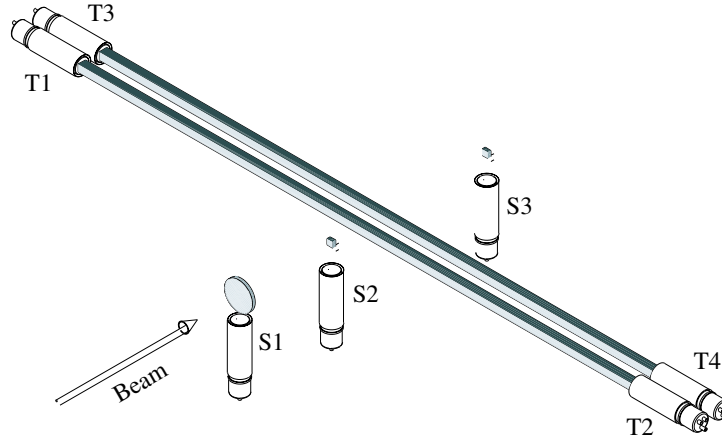
Figure 6.62: The setup for the beam tests at IHEP at Serpukhov.

Table 6.8: Time resolution for various phototubes.

Phototube	T_{av} Time Resolution (ps)
2.5 cm Bar	
XP2020	102
FEU 115	172
Hamamatsu R5506	167
Hamamatsu R5946	102
5.0 cm Bar	
XP2020	89
XP2020/UR	82

The beam defining counters shown in Figure 6.62 are S1, S2, and S3. The cross sectional size of the beam was large compared to the 2 cm by 2 cm size of S2 and S3. S2 and S3 were each 1.25 cm thick and both coupled to an XP2020 phototube with a 5 cm air gap. S1 was not used for timing purposes, nor to define the effective size of the beam.

The first data run at IHEP was used to test 2-m long counters with square cross sections of 2.5 $\times$ 2.5 cm^2 and 5.0 $\times$ 5.0 cm^2. The scintillator is type EJ-200, produced by the Eljen Corporation. This scintillator has a decay time of 2.1 ns, a bulk attenuation length of 4 m, an index of refraction of 1.58, a peak in the emission spectrum at 425 nm, and a light output equal to 64% of that of Anthracene. The surfaces of two of the four long sides of each bar were in contact with the casting form and had no other preparation. The other two long sides and the two ends of each bar were diamond fly-cut in order to minimize loses due to surface imperfections. A phototube was placed on each end of each bar. The two bars, with their phototubes, were placed in a light-tight box. The beam was a 3 to 40 GeV/c positive beam with variable energy.

Table 6.5.2 shows the results for average time resolution measured for various combinations of scintillation bars and PMTs. Figure 6.63 shows the variation of time resolution as a function of position of the beam along the bar (x=0 at the center) for the two types of bars.

In a later data run 2 m-long bars of cross sections 2.5 $\times$ 6.0 cm^2 were tested using a 5 GeV/c beam. A typical PMT pulse observed after a 40 m cable is shown in Figure 6.64. These
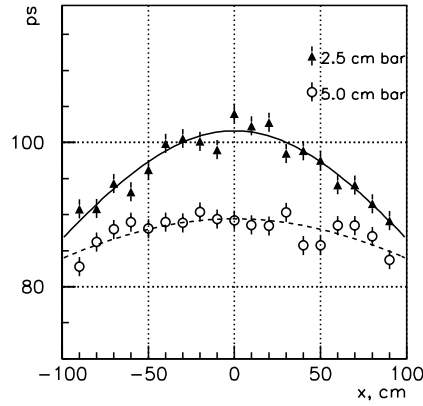
Figure 6.63: The average time resolution for a 2 m-long scintillation counter read out at both ends with Phillips XP2020 PMTs as a function of position of a charged particle beam along the bar (x=0 at the center of the bar). Bars of square cross section 2.5 × 2.5 cm^2 and 5.0 × 5.0 cm^2 were tested.

signals went to constant fraction discriminators (CFD) to eliminate time corrections associated with variations of signal amplitude. Measurements using leading edge discriminators (LED) and Analog to Digital Converters (ADC) were also made. In this case a time vs. amplitude correction was made using measured signal pulse heights. Custom made Time to Digital Converters (TDC) with 26.5 ps least count were used for time measurements. The S3 signal was used as the common start and signals from the other beam counters and the bars under test were used as stop signals. The intrinsic time resolution of the electronics was 18 ps (r.m.s.) as measured by using the S3 signal to both to start and to stop the TDC. The measured time resolution of S2 and S3 was 70 ps.
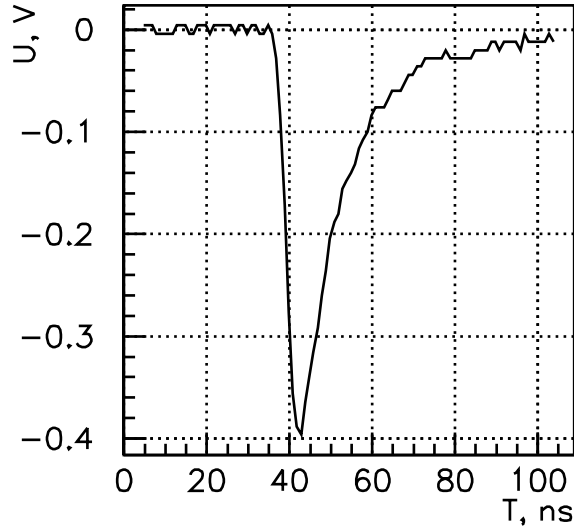
Figure 6.64: A typical pulse a Phillips XP2020 PMT attached to a 2 m long scintillation bar after the signal passed through a 40 m delay cable.

Figure 6.65 shows the average time resolution as a function of the position of the beam along the 2 m-long scintillator bar (x=0 at the center of the bar). In Figure 6.65a and figure 6.65b the open circles show resolution using a single bar and the closed circles show resolution using

information from both bars. In (a) the beam passed through 2.5 cm of scintillator and in (b) through 6.0 cm of scintillator. In (a) and (b) a constant fraction discriminator was used and in (c) pulse height information was used to do the time-walk correction for the case when the beam passed through 2.5 cm of scintillator.

Using constant fraction discriminators the time resolution for two bars was measured to be less than 40 and 60 ps when particle cross 6.0 cm and 2.5 cm of scintillator respectively. The results obtained with leading edge discriminators and corrected for time walk effect were similar to those measured with CFDs.
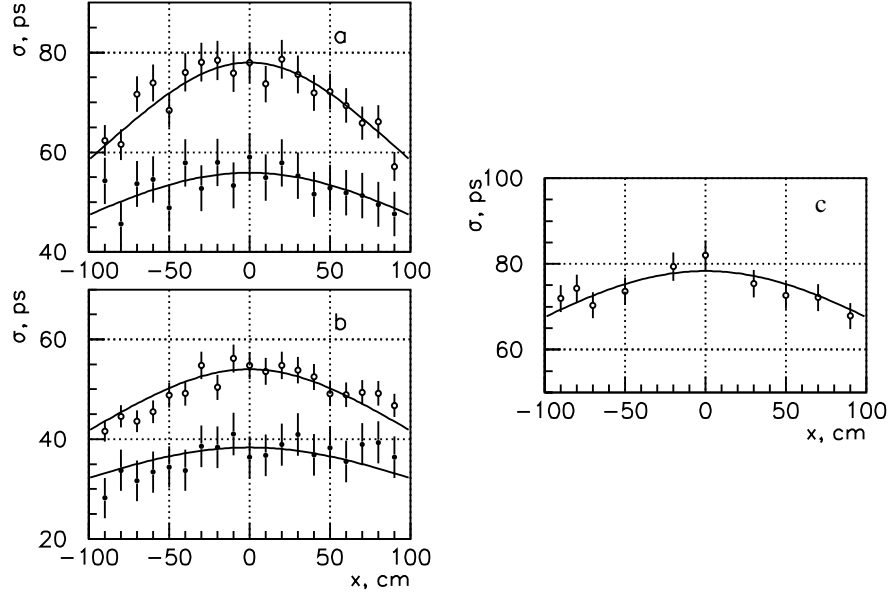
Figure 6.65: Average time resolution as a function of the position of the beam along the 2 m-long long scintillator bar (x=0 at the center of the bar). In (a) and (b) the open circles show resolution using a single bar and the closed circles show resolution using information from both bars. In (a) the beam passed through 2.5 cm of scintillator and in (b) through 6.0 cm of scintillator. In (a) and (b) a constant fraction discriminator was used and in (c) pulse height information was used to do the time-walk correction for the case when the beam passed through 2.5 cm of scintillator.

The tests described above in the hadron beam are described in more detail in references [51, 52]. In order to minimize the amount of material in front of the LGD bars of 1.25 cm thickness were tested and compared and those measurements were reported in reference [53].

Comparison of timing properties for the 1.25×6.0 cm^2 and 2.5×6.0 cm^2 bars shows that the time resolutions at the center of the bar are better by factor of ≈ 1.4 for the 2.5×6.0 cm^2 bar. But the time resolutions at the bar edges are the same in both cases indicating that near the PMT's the time resolution does not depend on photoelectron statistics.

Conclusions and remaining issues

Based on the results presented above, therefore, we have chosen the 1.25 cm thick, 6 cm wide bar for the TOF wall. As shown in Figure 6.65a, the time resolution for two bars of this size is 80 ps or less at all point on the bar – satisfying our design criterion.

In addition to optimizing the time resolution, a practical consideration in the choice of bar geometry is the ability to accommodate magnetic shielding for the approximately 200 G magnetic field in the vicinity of the XP2020s. For a 6 cm wide bar the phototubes can simply be attached
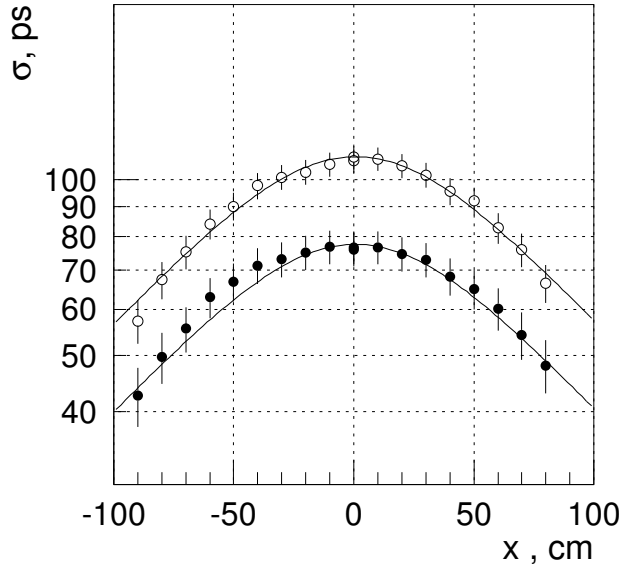
Figure 6.66: The time resolution for one (∘) and two (•) 1.25×6.0 cm^2 bars viewed by XP2020 PMT's.

to scintillator snouts and then surrounded by magnetic shielding; this cannot be done for bars less than 6 cm wide.

6.5.3 Čerenkov Counter

The Čerenkov detector for GluEX is unfortunately not as well defined as the rest of the equipment. This is due to the fact that the first group to express interest in this detector pulled out of GluEX because of the long time scales involved and detector became an *orphan* for several years. After the granting of CD0 to the JLab upgrade and GluEX in the spring of 2004, a pair of groups from Tennessee approached the collaboration about joining GluEX and taking on a large detector responsibility. The natural piece of hardware was the orphaned Čerenkov system.

Based on this interest, it was felt that a completely fresh look should be taken at the system. This should consider both the physics of GluEX and technological developments that have occurred over the last several years. The result of this effort is a proposal to build a DIRC detector rather than the gas Čerenkov system that had been proposed earlier. Because this proposal is so new, and the collaboration is still evaluating its implications, we have presented both the newer DIRC material and the older gas Čerenkov material here. A final decision on this clearly depends on many factors including physics, manpower, costs and timescales. The collaboration is currently evaluating these.

In the case of both Čerenkov designs, it is possible for the GluEX experiment to start taking quality data without this system in place. There is a very solid physics program with pions that does not need the Čerenkov. However, as the collaboration begins to study final states with both hidden and open strangeness, the Čerenkov system will be crucial. What follows are first a discssion of the DIRC option followed by the earlier work on the gas Čerenkov detector.

A DIRC Čerenkov Detector

The Cherenkov detector, DIRC, of the BABAR experiment at the PEP-II asymmetric B-factory of SLAC has proven to be a successful novel technique for pion and kaon identification [55] [56][57].

The DIRC (acronym for **D**etection of **I**nternally **R**eflected **C**herenkov (light)) is a ring imaging Cherenkov detector. It provides the identification of pions, kaons, and protons for momenta up to 4.5 GeV/c with high efficiency. This is needed to reconstruct CP violating B-decays and to provide B-meson flavor tagging for time-dependent asymmetry measurements. The DIRC radiators consist of long rectangular bars made of synthetic fused silica and the photon detector is a water tank equipped with an array of 10,752 conventional photo-multiplier tubes (PMT). By the summer 2004, BABAR had recorded about 227 million $\bar{B}B$ pairs, exceeding the design luminosity of $3 \cdot 10^{33}/cm^2s$. The observation of direct CP violation with more than 4 standard deviations in the decay $B^0 \to K^+\pi^-$ [58], which has to be distinguished from B^0 decays into $\pi^+\pi^-$ and K^+K^-, is a successful demonstration of the DIRC's capabilities.

Similar to the physics program of BABAR, the spectroscopy program of GlueX depends on the capability to identify charged kaons. We discuss the possibility to adapt the DIRC concept for the GlueX detector to complement the particle identification information of the tracking chambers and the time-of-flight (TOF) detector for momenta above 1.5 GeV/c.

The BABAR DIRC

The physics program of the BABAR [59] detector is to observe CP violation and to probe the Standard Model of Particle Physics by collecting enough B-meson decay channels to over-constrain predictions. The source of B mesons is the PEP-II asymmetric e^+e^- collider [60][61][62], where 9 GeV electrons strike 3.1 GeV positrons producing $\Upsilon(4S)$ resonances with a boost of $\gamma\beta \simeq 0.56$. The $\Upsilon(4S)$ resonance decays nearly exclusively in a pair of B and anti-B mesons. This allows precise measurements of time-dependent asymmetries in B meson decays which can be related to the CP violation phase in the Cabbibo-Kobayashi-Maskawa (CKM) matrix [63].
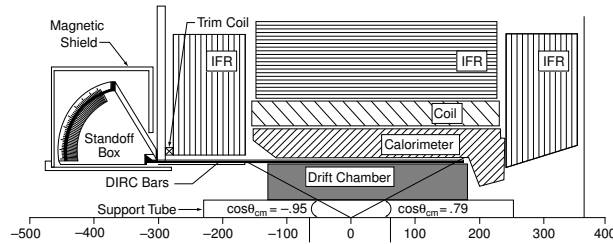
Figure 6.67: The side-view of the BABAR detector with the components of the DIRC indicated (units in cm).

BABAR is a typical collider detector but asymmetrically placed around the interaction point to ensure nearly full solid angle coverage in boost (forward) direction (see Fig. 6.67). The location of the particle identification system is radially between the drift chamber and a CsI(Tl) crystal calorimeter. Therefore, a small radiation length is preferred to avoid deterioration of the excellent energy resolution of the calorimeter. The DIRC minimizes the radial dimension and keeps the amount of required calorimeter material (cost) small. Up to a momentum of 700 MeV/c, the drift chamber can provide pion-kaon separation based on the dE/dX measurement. Only if pion-kaon separation up to 4.5 GeV/c particle momentum is available can one distinguish the channels $B^0 \to \pi^+\pi^-$ from $B^0 \to K^+\pi^-$ or $B^\pm \to \phi\pi^\pm$ from $B^\pm \to \phi K^\pm$, interesting for the measurement of indirect or direct CP violation. Moreover, the flavor content of the recoil $B(\bar{B})$ needs to be tagged by identifying kaons in its successive decays with momenta below 4 GeV/c. In addition, τ, charm-, and light-quark meson spectroscopy profit from kaon identification.

The difference in the Cherenkov angle between a pion and a kaon at 4.0 GeV/c momentum is 6.5 mrad. Therefore, a 3 standard deviation π/K separation requires resolution of the Cherenkov angle for given a track of 2.2 mrad or better (see Fig. 6.68). Finally, to operate successfully in the high-luminosity environment of PEP-II, the Cherenkov detector has to be radiation hard,
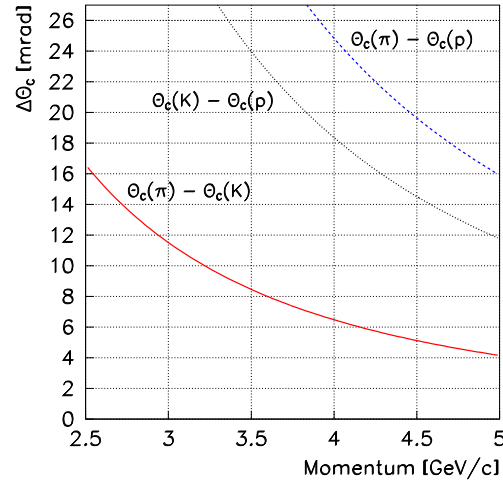
fast, and tolerant of background.

Figure 6.68: The difference in the Cherenkov angles between pions, kaons, and protons in synthetic quartz.

Principle of the BABAR DIRC

The DIRC uses thin, long rectangular bars made of synthetic fused silica (quartz) [64] (H × W × L = 17 mm × 35 mm × 4900 mm) both as Cherenkov radiators and light guides (refractive index $n_1 \approx 1.47$). Bars are glued together from four pieces, each 1225 mm long. All together, 144 bars are arranged in a 12-sided polygonal barrel with a radius of about 84 cm around the beam axis. The DIRC bars extend 178 cm forward from the interaction point of BABAR covering 87% of the polar solid angle in the center-of-mass frame. The azimuthal coverage is 93% , since there are gaps between the bars at the 12 sides of the radiator polygon. Every 12 bars are housed in a bar-box surrounded by nitrogen at STP (index $n_2 \approx 1$). The box is built mostly of aluminum honeycomb material. The radiation length (X_0) of the bars is 14%, and 19% for the full assembly at perpendicular incidence. A schematic view is presented in Fig. 6.69.
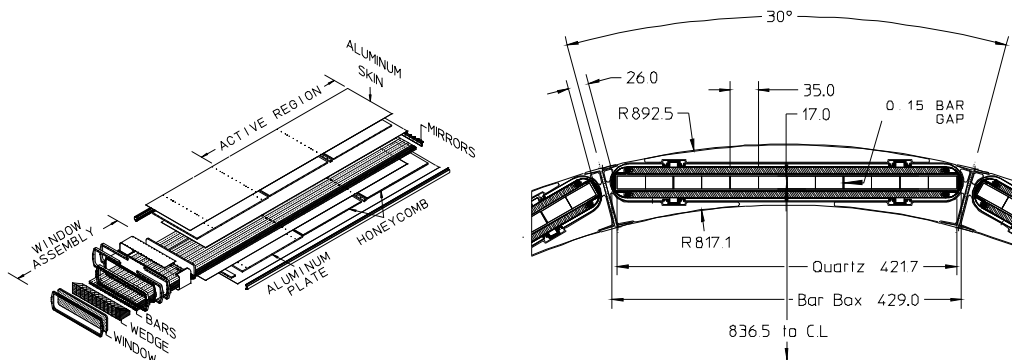
Figure 6.69: Left: View of a bar-box assembly. 12 bar-boxes surround the drift chamber. Right: Placement of the bar-box in the BABAR detector above the cylindrical drift chamber.

The principle of the DIRC is shown in Fig. 6.70. The DIRC imaging works like a pinhole focus camera with the bar cross section small compared to the imaging plane.
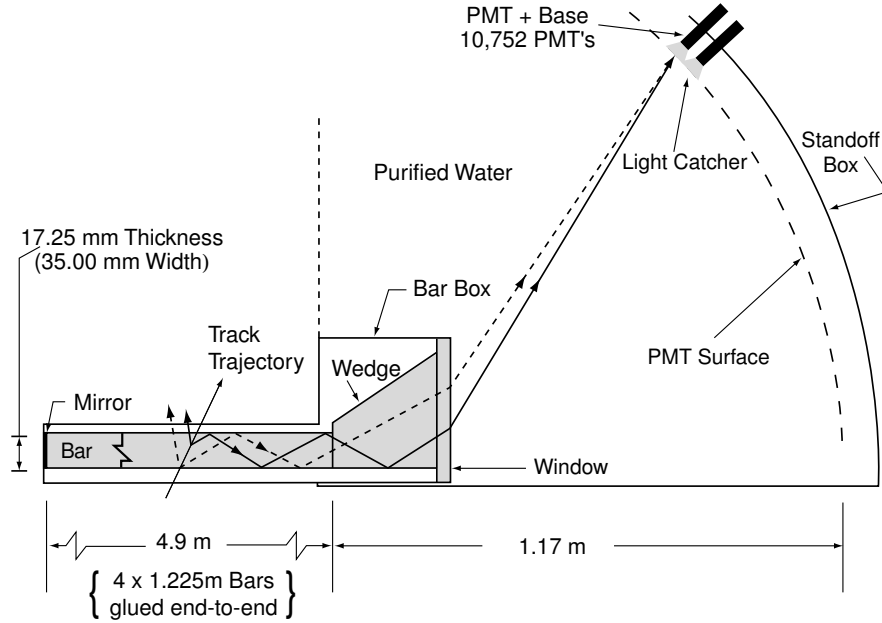
Figure 6.70: The principle of the BABAR DIRC.

Since the refractive index of the radiator bar n_1 is larger than $\sqrt{2}$, a certain fraction of the Cherenkov photons produced by a relativistic charged particle traversing the quartz bar will be totally internally reflected, regardless of the incidence angle of the track, and propagate along the length of the bar. Only one side is viewed by the PMT array and a mirror (reflectivity $\approx$ 92%) is placed perpendicular to the bar axis on the other end, where positrons enter the BABAR detector. Due to the boost of the $\Upsilon(4S)$ there is a higher density of charged tracks towards the mirror side and hence it is less preferable for the readout. Since the rectangular bar is of high optical precision (mean surface reflectivity $\approx$ 99.96% per bounce at 442 nm photon wavelength), the initial direction of the photon is preserved throughout its propagation, modulo left/right, up/down and forward/backward ambiguities. The latter is resolved by the measurement of the photon arrival time. The bars have very high light transmission (99.9% at 442 nm photon wavelength) required for the typical photons path-lengths of 6 to 20 m.

Photons exiting the bar in the downward direction, or with large exit angles with respect to the bar length axis, are partly recovered into the instrumented area by a prism (wedge). This optical element is 91 mm long and the top side has a 30° opening angle. The bottom side is slightly tilted upwards by 6 mrad. It reduces the required photon-sensitive area by more than a factor of two.

A thin (9 mm) quartz window separates the prism from the so called standoff box (SOB), a water tank filled with 6000 liters of purified water ($n_3 \approx 1.33$) in a toroidal shape. The backplane of the SOB is divided into 12 sectors, each equipped with 896 conventional photo-multiplier tubes [65] ($\approx$ 25% quantum efficiency at 400 nm wavelength, 250 nm – 650 nm spectral range), facing the wedge of a corresponding bar box. Hexagonal reflectors (light catchers) with water-resistant rhodium surfaces surround the PMT cathodes improving the detection efficiency by about 20%. The ratio of refractive indices n_1/n_3 is nearly wavelength independent. It reduces internal reflection at the bar-box wedge. Furthermore, the exit angle is magnified by this ratio, increasing the position resolution of the photons.

The detector provides a three dimensional measurement of the photon in the variables (α_x, α_y), the photon exit angles with respect to the bar axis, and the arrival time of the photon t_a. The spatial position of the bar through which the track passed and the particular PMT hit

within a certain readout time interval is used to reconstruct the photon vector pointing from the center of the bar end to the center of the tube. This vector is then extrapolated back into the quartz bar using Snell's law, where the photon exit angles (ϕ_C, θ_c) with respect to the track are calculated. Most of the photon phase space $(\alpha_x, \alpha_y, t_a)$ is mapped onto the Cherenkov angles (ϕ_C, θ_c) with less than a three-fold average ambiguity.

The timing information apart from the resolution of the forward-backward propagating photons, is not competitive with the position information, but it is crucial for suppression of beam background. The expected arrival time of the Cherenkov photon is a sum of the time-of-flight of the charged particle from its origin to the quartz bar (typically 2-3 ns), the photon propagation time in the quartz bar and the wedge along its reconstructed path, and the traveling time through the water before reaching the surface of the PMT. Applying the reconstructed mean arrival time of the photons in an event as correction for the uncertainty in the bunch-crossing time yields a precision of about 1.5 ns in the time between photon creation and photon arrival, which is close to the intrinsic time resolution of the PMTs. This allows restriction of the event time interval to 8 ns.

Particle identification uses likelihood ratios for different particle hypotheses based on the number of photons above and below threshold and the Cherenkov angle. Another way to use the information is to compare the ring pattern in the PMT plane with expected patterns for the different particle hypotheses.

Imaging with Synthetic Fused Silica

The Cherenkov angle separation between particle types is the Cherenkov angle difference in Fig. 6.68 divided by the Cherenkov angle resolution σ_C. This resolution, in turn, depends primarily on the precision of the track angle of incidence as provided by the tracking detectors, σ_t, and the single photon Cherenkov angle resolution in the DIRC, $\sigma_{C,\gamma}$, and the number of photo-electrons contributing to the measurement, N_γ, as follows:

$$\sigma_C = \sqrt{\sigma_t^2 + \sigma_{C,\gamma}^2/N_\gamma} \,. \tag{6.20}$$

The dominant contributions to the error of the single photon measurement are

chromatic	5.4 mr
imaging (bar size) and detection (PMT size)	7.5 mr
transport (through the bar)	1.0 mr .

These add in quadrature to $\sigma_{C,\gamma} = 9.3$ mr. The number of Cherenkov photons per track for di-muon events versus the track polar angle with respect to normal incidence is shown in Fig. 6.71 b). The number varies between 25 and 60 photons. Therefore, with negligible tracking resolution, σ_C decreases from 1.9 mr to 1.2 mr in the extreme forward direction where tracks have the highest momenta in BABAR due to the boost. The imaging and detection error can be improved by extending the distance between bar end and PMT plane. For instance, with a distance of 1.4 m we obtain a single photon angle resolution of about 8.3 mr. With a slightly increased bar thickness and shorter bars the minimum number of photons per track can be increased to 25 or higher.

Features of the BABAR DIRC

Here we summarize the main advantages of the BABAR DIRC type Cherenkov detector:

- The BABAR DIRC separates kaons from pions to better than 3 standard deviations below $4\,GeV/c$. It is an imaging device in the required momentum range with high photo-electron yield (25 or more). It also works as a threshold detector for different particle types with momenta below 0.92 times the particle's mass.

- Compact: The total thickness between tracking and calorimeter is less than 5 cm. The total radiation length (X_0) for a full assembly is 19%.
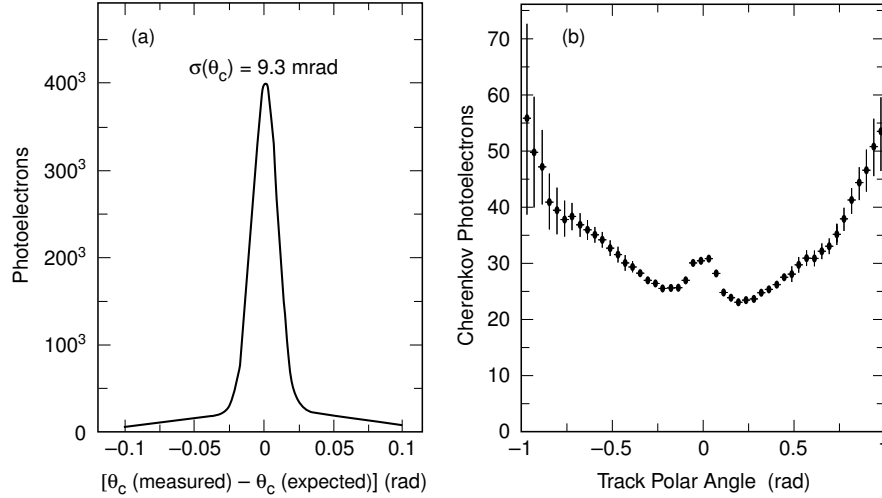
Figure 6.71: (a) The Cherenkov angle resolution for single photons associated with a particle track. (b) The number of Cherenkov photons per track versus the track polar angle with respect to normal incidence. The slightly lower efficiency in forward direction is due to the reflection in the mirror and the increased photon path-length in the bar.

- Radiation robust: It has been demonstrated that there is no efficiency loss in the wavelength regime above 280 nm after irradiation with 250 krad [66].

- Fast device: The photon collection time is less than 100 ns.

- Insensitive to background: The BABAR DIRC is a 3-dimensional device; the photon arrival time and the location of the PMT are correlated, allowing reconstruction of the true arrival time of the Cherenkov photons originating from the same track with a precision of 1.5 ns. Therefore, the event time interval can be smaller than 10 ns.

- Robust device: The radiator is passive and needs only to be kept in a dry atmosphere. Conventional photo-multiplier tubes are used which can be easily accessed. The DIRC is the subsystem within BABAR that requires the least maintenance.

Requirements for GlueX

In the previous design a gas-Cherenkov detector is placed behind 4 layers of FDCs and before the TOF system. It extends into the inner cylinder of the solenoid and has an effective length along the beam axis (z-axis) of 1.4 m. Instead of this detector a DIRC system can be positioned at some short distance behind the solenoid opening. To evaluate the situation with GEANT simulations [67] we place a virtual (xy) plane perpendicular to the beam direction at $z = 450$ cm, which is about 10 cm behind the solenoid opening. Without modification of the bar-imaging concept of the DIRC detector, the bars would line up along one axis in that plane and leave a gap for the beam to pass through.

Particle Momenta and Angle of Incidence   In a typical reaction $\gamma\, p \rightarrow$ (mesons) p with strangeness production, 50% of the pions and kaons (somewhat fewer protons) produced with momenta between 1 GeV/c and 5 GeV/c arrive at the Cherenkov detector plane. In many cases strangeness conservation can be used to recover the final state if the remaining particles are identified with high efficiency. Highly efficient and redundant kaon identification is required to access a large variety of final states and to reduce combinatorial background in the search for new signals. A particle identification coverage with constant efficiency and low mis-identification rate over the full momentum range is essential to perform angular analysis of their decays.

Figure 6.72 shows the momentum spectra for the pions, kaons, and protons which arrive at the Cherenkov-detector plane for the two reactions:

$$\gamma p \quad \rightarrow \quad K^{*0}(892)K^{*0}(892)p \tag{6.21}$$
$$\rightarrow K^+\pi^- K^-\pi^+ p$$
$$\gamma p \quad \rightarrow \quad K_1(1270)K^- p \tag{6.22}$$
$$\rightarrow K^{*-}\pi^+ K^- p$$
$$\rightarrow K^-\pi^0\pi^+ K^- p\,.$$

These are typical reactions with more than two final state pions and kaons. In these final states kaon-pion separation is required up to a momentum of 5 GeV/c. Based on dE/dX and TOF a 3 standard deviation separation is obtained up to 1.5 GeV/c momentum, while with the kaon threshold in a DIRC at 0.45 GeV/c enough photo-electrons are created for efficient Cherenkov imaging. The proton spectrum extends to 2 GeV/c and below 1 GeV/c a DIRC detector acts as a threshold Cherenkov detector for this particle type.
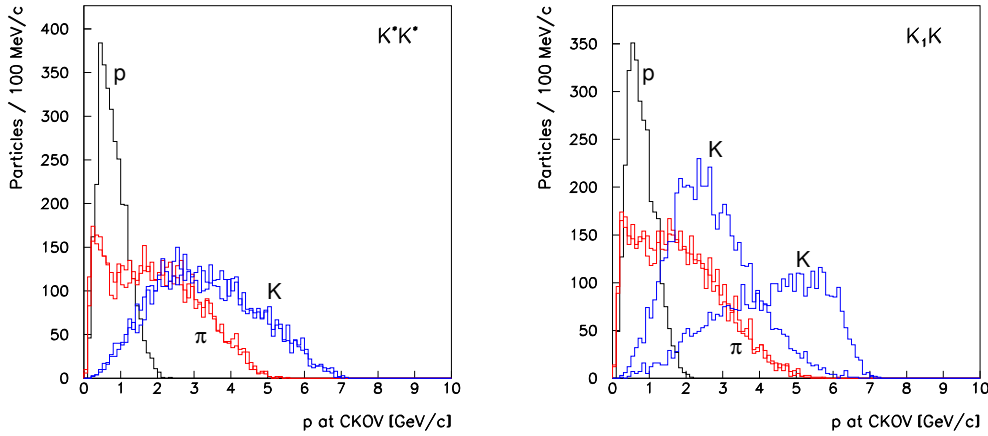
Figure 6.72: The particle momenta at the Cherenkov detector plane ($z = 450$ cm) for the two reactions described in the text (π:pions, K:kaons, p:protons).

Figure 6.73 shows the polar angle with respect to the z-axis for the charged final state particles in the reactions Eq. 6.21. This angle typically does not exceed 15 degrees. Pions with polar angles greater than 15 degrees typically have momenta below 1 GeV/c.

Beam Background We assume an electron beam current of 3 μA. This is the high-luminosity scenario for the Hall-D project. We use a full GEANT simulation of the GlueX detector [67] to track primary and secondary particles. The charged particle background which can create Cherenkov light consists mostly of electrons and positrons coming from upstream or from photon conversions in the Cherenkov detector.

Figure 6.74 shows the combined electron-positron rate along the y-axis in our virtual detector plane at $z = 450$ cm. We obtain rates below 100 kHz per cm (200 kHz per 2 cm) at distances of about 6 cm from the beam axis. The total rate integrated over all of x and from ±6 cm to ±65 cm (the hole radius) of y is at the most 900 kHz. The integration from ±10 cm to ±65 cm of y yields a total rate of 580 kHz.

Figure 6.75 shows the photon rate per cm along the y-axis integrated over all of x in the virtual detector plane at $z = 450$ cm. We expect 600 kHz/cm photons at distances near $y = 6$ cm. The total rate integrated over all of x and from ±6 cm to ±65 cm of y is 29.6 MHz; from ±10 cm to ±65 cm of y it is 24 MHz.
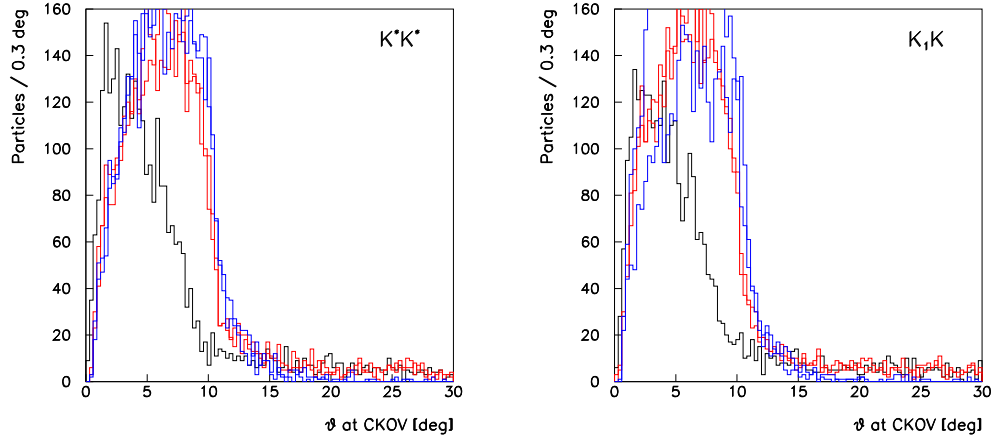
Figure 6.73: The polar angle with respect to the normal incidence at the Cherenkov detector plane ($z = 450$ cm) for pions, kaons, and protons in the two reactions described in the text.

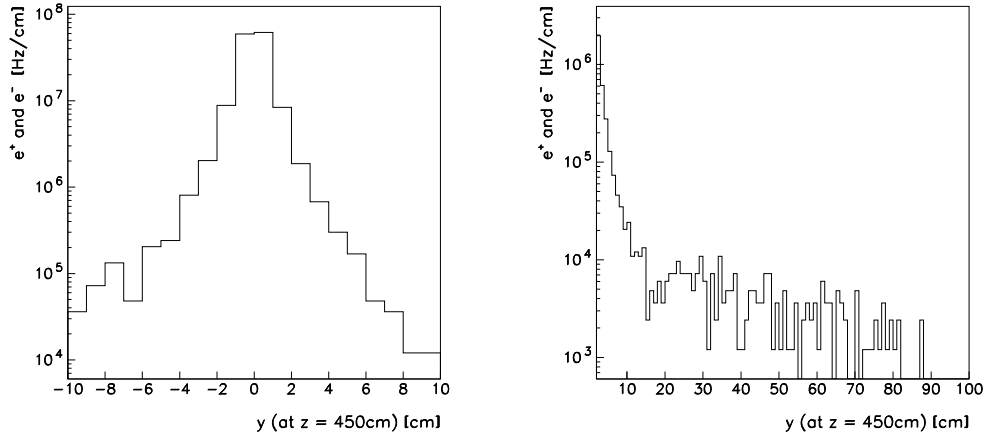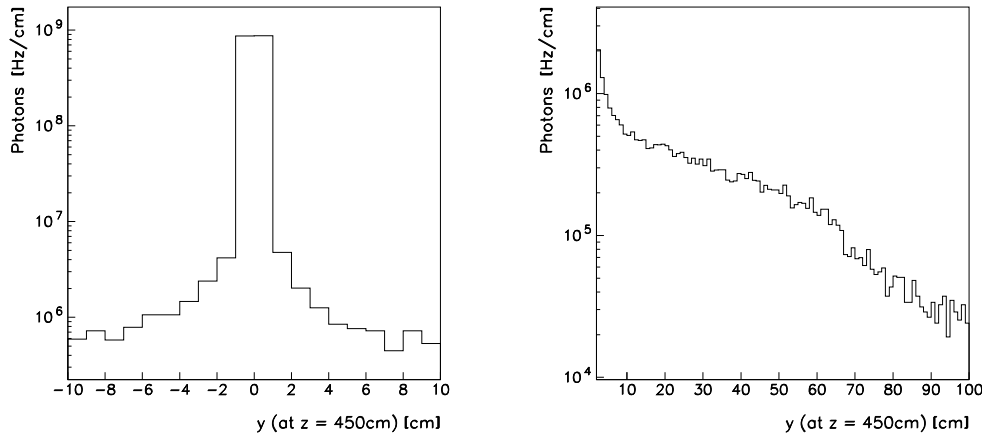
Figure 6.74: The rate of electrons and positrons per cm along the y-axis integrated over all of x at the location $z = 450$ cm. Left: rate/cm below ± 10 cm in y. Right: rate/cm versus y. The innermost 3 cm are omitted.

Each electron or positron potentially creates 30 detected photons in the struck bar. A beam photon converts with a probability of about 15% into a electron-positron pair somewhere inside the DIRC generating an average of 20 photons per lepton track. We estimate, that a DIRC placed at a distance of ± 6 cm away from the beam axis produces Cherenkov light into the readout tank at a rate of 210 MHz. If the DIRC has a central gap of ± 10 cm the total rate is 160 MHz. The time to collect photons out of the bars is less than the 100 ns for the long BABAR DIRC bars. We estimate the number of beam-background related Cherenkov-photons within 100 ns for a gap in the plane along the y-axis of ± 6 cm (± 10 cm) to be 21 (16). After reconstruction we can reduce the time window for the photon arrival to less than 10 ns, which reduces the background photons to 2, while we expect 25 or more signal Cherenkov photons in a limited region of the readout plane.

The hit rate in a single PMT depends also on the optics at the bar end (opening angle of the wedge) and the profile of the background shown in Fig. 6.74 and Fig. 6.75. Assuming that

Figure 6.75: The rate of photons per cm along the y axis integrated over all of x at the location $z = 450$ cm. Left: rate/cm below ± 10 cm; Right: rate/cm versus y. The innermost 3 cm are omitted.

typically 1000 PMTs are randomly hit, the rate per tube is 210 kHz. This is the average rate encountered by PMTs in the BABAR DIRC which tolerates up to 1 MHz.

Magnetic Field The solenoid has strong fringe fields. We simulate the situation with the TOSCA program [68]. At a distance of about 3 m left or right of the solenoid center the field strengths are below 100 Gauss. Efficient operation of conventional photo-multiplier tubes requires shielding. In BABAR a magnetic field strength transverse to the PMTs of less than 0.2 Gauss is achieved with metal shielding and bucking coils.

Irradiation From the penetration rate with charged particles we estimate the radiation dose per year. We assume that the dominant component is secondary electrons and positrons created upstream or in the bars by photon conversions. The flux versus radius is shown in Fig. 6.76. It stays below 100 kHz/cm^2 for radii greater than 3 cm. For a flux of 100 kHz/cm^2 and a minimum ionizing $dE/dx = 1.6$ MeVcm^2/g we estimate a yearly dose of 51 krad. This rate is well below the negligible dose of 250 krad tested with a ^{60}Co source [66].

Conceptual Design

At this point we discuss a geometry and imaging concept similar to that in the BABAR DIRC. In fact, we can even envision the use of four of the DIRC bar-boxes which would only need the design of a new support and a new shielded readout tank.

However, for a new design the bar dimensions can be optimized. Because azimuthal and polar angles of incidence are comparable and we expect a higher background rate per bar closer to the beam compared to BABAR , a width of 2 cm is more appropriate than 3.5 cm. The thickness can be increased from 1.7 cm to 2 cm to increase the photon yield and the structural stability. The modularity should be kept, with say, 14 bars in a box. Altogether four boxes provide a geometrical match. In principle, the bars could follow the circular boundary of the magnet opening. Also, the gap can be partly covered from the readout side. This would results in bars with different lengths.

The water tank should be placed on the side of the magnet, shielded, and away from secondary tracks which are produced in the forward direction in the central calorimeter or in the magnet yoke. This may also require that the bars be somewhat farther downstream (greater z). Hence, the length of the bars and their z position is a matter of further optimization. We
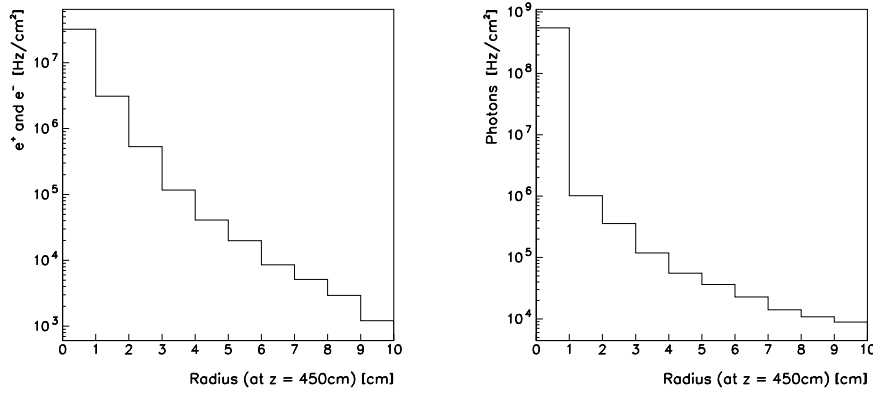
Figure 6.76: Left: The rate of electrons and positrons together per cm^2 versus radial distance from the beam axis in the virtual plane at $z = 450$ cm. Right: The same for photons.

explore the possibility that the purified water can be kept sealed in the tank for several years without maintenance.

In our first approach we allow the bars to extend into a region where there are no spatial restrictions and the transverse magnetic field [68] at the location of the PMTs is about 10 Gauss, while the longitudinal field drops below 45 Gauss. This corresponds to about 3 lengths of BABAR DIRC bars. Figure 6.77 shows the technical drawing of a first draft design of the bar arrangement with bars of 1.225 m length and a front area of 2×2 cm^2. We have not optimized the bar length to follow the circular shape of the hole. Each 14 bars are housed in a separate bar-box. Two bar-boxes are placed below and two above the center leaving a gap for the beam to pass through. The readout side is shown in Figure 6.78. The maximum upward opening angle at the readout is 52 degrees. The sides open up with an angle of 30 degrees. Each tube covers an angle of 2 degrees. In this scenario the number of photo-tubes is 1512. A three-dimensional view of the half open bar-boxes and the readout tank is presented in Fig. 6.79.
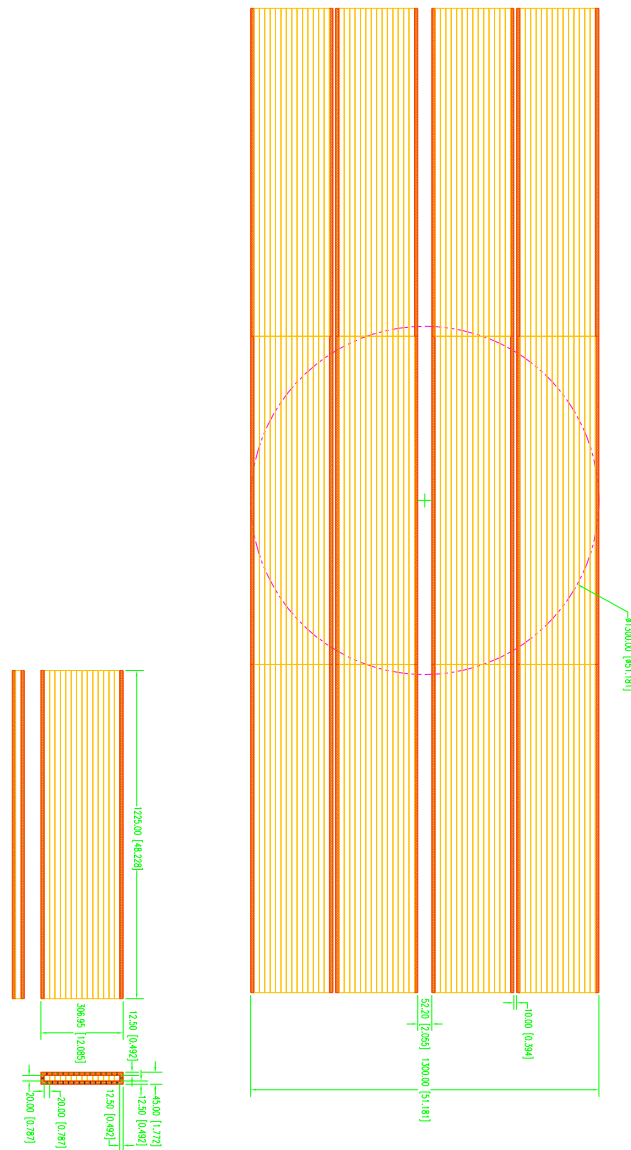
Figure 6.77: Arrangement of the bar-boxes in front of the solenoid. The circle indicates the size of the inner radius of the cylindrical calorimeter inside the solenoid. The bar-boxes will be placed asymmetrically with respect to that hole.
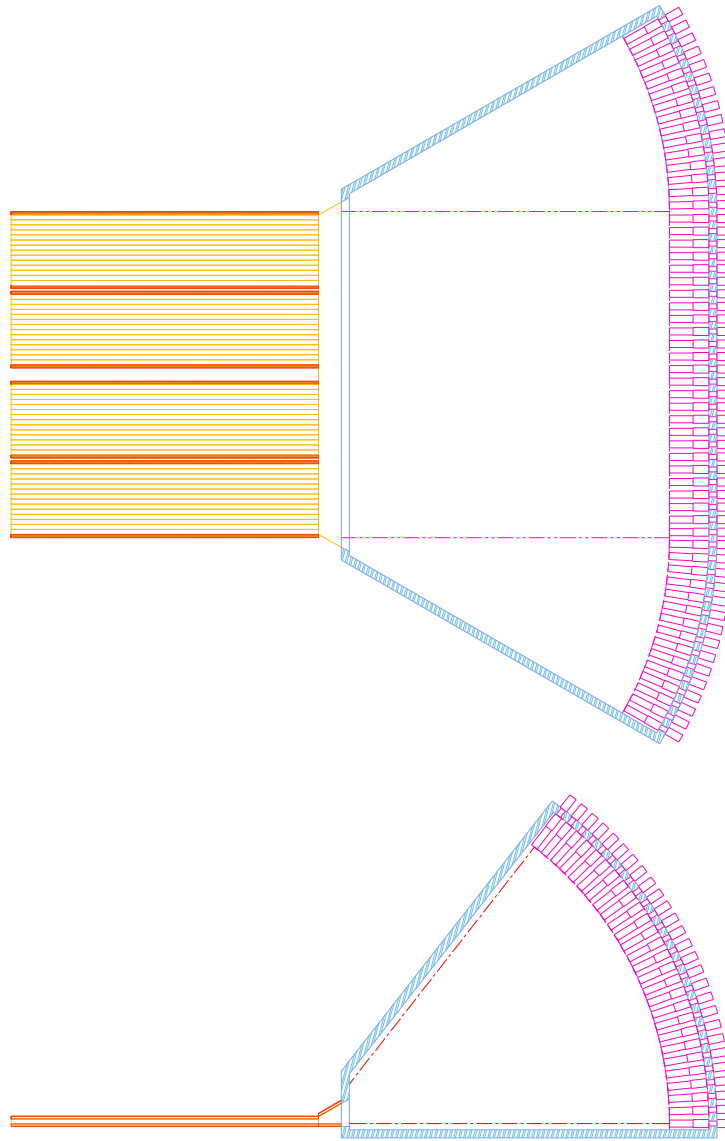
Figure 6.78: The readout side of the bars. The volume will be filled with water and the photomultiplier tubes will be immersed in the water as in the BABAR DIRC.
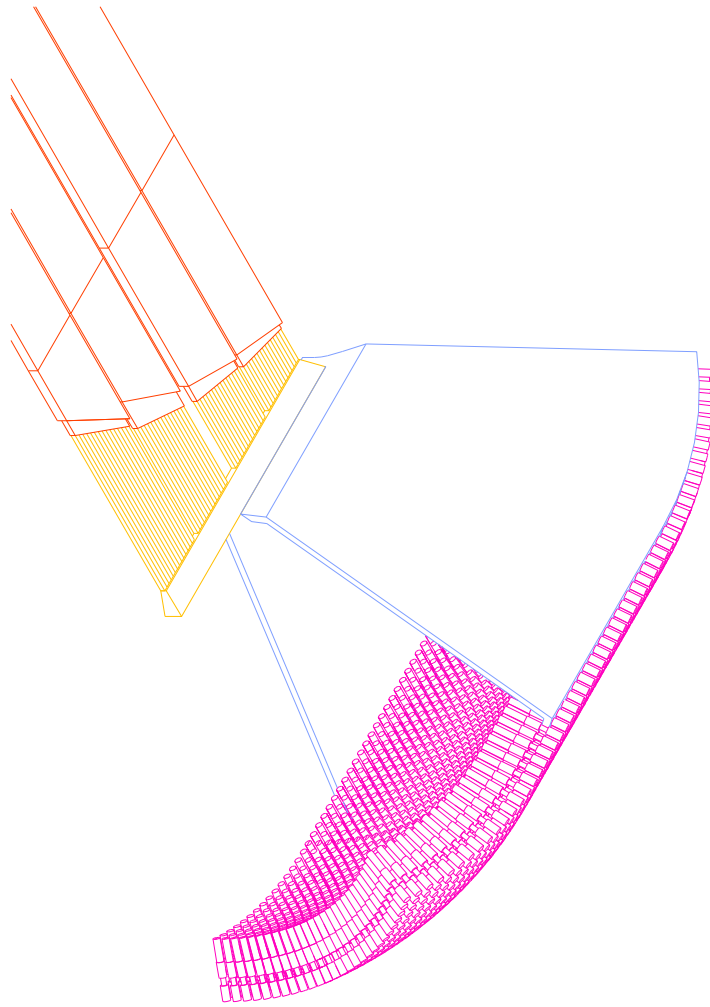
Figure 6.79: A 3-D view into the four half open bar-boxes and the readout tank.

The Gas Čerenkov Counter System

TOF measurements alone will not provide particle identification above 3 GeV/c, and thus TOF does not suffice for typical reactions of interest. Therefore a threshold Čerenkov detector has been included in the HALL D design. The primary function of this detector is to signal the presence of pions over a large part of the expected momentum range (see Figure 6.80).

Several radiator materials have been considered for the design. A pressurized gas radiator has the advantage of allowing one to match the index of refraction to the desired momentum range. A prototype of such a detector was developed for CLEO-III [69]. However this method requires the use of thick gas containers in the downstream detector region. This results in unwanted photon conversions and hadronic interactions, as well as safety concerns. Two atmospheric-pressure radiators were found to produce high acceptance rates: aerogel ($n = 1.008$), and C_4F_{10} gas ($n = 1.00153$). The C_4F_{10} gas radiator has been chosen for HALL D because it is has a threshold momentum of 2 GeV/c for pions, which complements the TOF system's useful range of 3 GeV/c and below. The kaon threshold of 9 GeV/c in this gas is nicely above the momenta that will be encountered in the experiment, overlapping less with the TOF system.
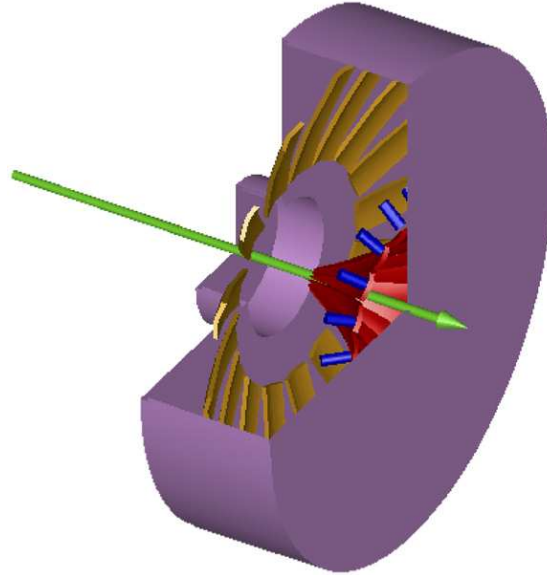
Figure 6.80: A schematic drawing of the HALL D Čerenkov detector system. The particles enter from the left into the gas volume in the center. The Čerenkov light is then reflected off the mirrors in the center (shown in dark) into the phototubes at the outer rim (shown as dark cylinders).

Gas-filled Čerenkov detectors have been used in many particle physics experiments. The original LASS spectrometer [37] used a freon radiator in a design similar to the one in HALL D. The primary changes we will make in the LASS design are the use of an environmentally friendly gas (freon is no longer available) and mirrors made of low-density carbon-fiber composite materials. The gas handling system will be patterned after a similar system now in use on the JLab CLAS spectrometer. The detector will be segmented into sixteen azimuthal regions, each housing a single mirror that focuses light onto its own photomultiplier tube. Light emitted into the region within 10 cm of the beam axis will not be collected in order to suppress accidental coincidences in the detector. A sketch of the optical design is shown in Figure 6.80. The minimum radiator thickness encountered by a particle traversing the detector is approximately 90 cm. The measured performance of the JLab CLAS Čerenkov detector was used to estimate the photoelectron yield of the HALL D design, adjusting for radiator length and the number of mirror reflections. This results in an expected average yield of 5.0 (3.3) photoelectrons for 5.0 (2.9) GeV/c pions.

Particles that traverse thicker regions of the detector will register proportionately larger signals.

The optical design of the detector (two ellipsoidal mirrors) was chosen to produce a strong focus at the photomultiplier tubes. This produces small linear magnification and allows good light collection from the wide range of particle trajectories exiting the solenoid. Prototype mirrors were constructed and tested for their focal properties. These were found to be mechanically and optically stable after cutting to shape. Having two mirrors in the design also offers flexibility as to the placement of the photomultipliers. This freedom was used to place the axis of the tubes perpendicular to the ambient magnetic field. This was done to optimize the effectiveness of the passive magnetic shields surrounding the photomultipliers.

A finite-element analysis of the shielding requirements was performed with the FLUX-3D computer code. A four-layer shield with axial symmetry was found to produce adequate reduction in the magnetic field. The predicted transverse field at the photocathode is less than 0.1 gauss. Burle 8854 photomultipliers were chosen for their high detection efficiency and low noise level.

A Monte Carlo simulation of the Čerenkov detector efficiency was made for the events in the following reaction:

$$\gamma p \to X p \to K^* \bar{K}^* p \to K^+ \pi^- K^- \pi^+ p \tag{6.23}$$

The geometry, mirror reflectivity, kinematics and photomultiplier response were modeled in the simulation, which yielded the detector efficiency as a function of pion momentum (see Figure 6.81).
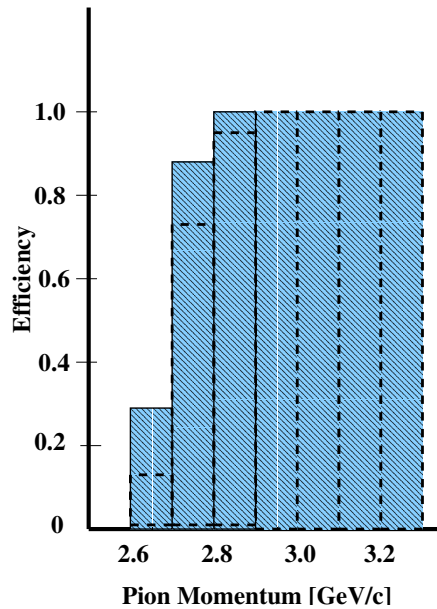
Figure 6.81: Predicted pion detection efficiency as a function of average pion momentum. The solid histogram is for a one-photoelectron detection threshold and the dashed line is for a two-photoelectron threshold.

6.5.4 Acceptance of The Particle Identification System

Since each of the particle identification subsystems works most effectively in different regions of momentum and different regions of particle production, and since no subsystem alone can provide particle identification for all the events necessary for GLUEX analyses, it is crucial to integrate the information from the different subsystems in the most effective way possible. An algorithm based on assigning likelihoods to different particle hypotheses using information from all the relevant subsystems is one natural and straightforward way to proceed.

Given a track with a measured momentum, the basic idea is to use information from the different particle identification elements (dE/dx from the CDC, times from the BCAL and forward TOF, and Cerenkov photoelectrons or Cerenkov opening angle) to assign this track a set of likelihoods, each likelihood corresponding to a different particle hypothesis. For example, $L(\pi)$ and $L(K)$ are the likelihoods a given track is a pion or a kaon, respectively. Once these likelihoods are known, a statistical test can be performed to discriminate between hypotheses. One of the most convenient tests, the likelihood ratio test, works by forming the χ^2 statistic $R(i)$ for each particle hypothesis i ($i = \pi, K, p$):

$$R(i) = -2\ln\frac{L(i)}{L(\pi) + L(K) + L(p)}. \tag{6.24}$$

Making the requirement

$$R(i) > 2.7 \tag{6.25}$$

rejects hypothesis i at the 90% confidence level.

This method lends itself well to the GlueX environment since separate likelihoods can be calculated for each subdetector individually and then combined into overall likelihoods. For example, the likelihood a given track is a kaon is computed from individual detector likelihoods as:

$$L(K) = L^{CDC}(K)L^{BCAL}(K)L^{CKOV}(K)L^{TOF}(K). \tag{6.26}$$

To illustrate how likelihoods are calculated for specific detector elements, consider the forward TOF system. Start with a track with measured momentum p. The expected time required for this particle to traverse a distance L from the target to the TOF wall can be calculated under different assumptions for the particle mass:

$$t_i = \frac{L}{c}\left(\frac{m_i^2}{p^2} + 1\right)^{\frac{1}{2}}, \tag{6.27}$$

where $i = \pi, K, p$. This time will have an associated error σ_i, which can be obtained by combining the inherent resolution of the scintillator and electronics ($\approx$ 70 ps) with the effects of momentum resolution and the uncertainty in the path length. Assuming the time measurement follows a gaussian distribution, the likelihood for hypothesis i is then:

$$L^{TOF}(i) = \frac{1}{\sigma_i\sqrt{2\pi}}\exp\frac{-(t - t_i)^2}{2\sigma_i^2}, \tag{6.28}$$

where t is the measured time the particle spent between the target and the TOF wall. The closer the measured time t is to a calculated expected value t_i the more likely the particle being considered is of type i. Likelihoods for the other detectors are calculated in a similar way, using predicted and measured dE/dx for the CDC, predicted and measured time at the BCAL, and the expected and observed numbers of photoelectrons in the gas Cerenkov (or the predicted and measured Cerenkov angle in a DIRC detector).

A simulation of the integrated GlueX particle identification system using the likelihood methodology was carried out for $\gamma p \rightarrow K^*\bar{K}^*p$ events. The properties of these events have already been described at the beginning of this chapter (see figures 6.57 to 6.60). The generated events were sent through a full GEANT simulation and hits were recorded at each of the subdetectors associated with particle identification.

Relevant track measurements were smeared at each subdetector according to their expected resolutions. The dE/dx measurement of the CDC was smeared by 10%; the time of flight at the BCAL by 250 ps; and the time of flight at the forward TOF wall by 70 ps. In addition, the momentum and path length of each track was perturbed randomly by 1% to simulate uncertainties in the tracking. For the simulation using the Gas Cerenkov option (CKOV), the generated number of photoelectrons were distributed according to a Poisson distribution with an 80 cm C_4F_{10} radiator length with index of refraction $n = 1.0015$ and efficiency $N_0 = 90\text{cm}^{-1}$ (see equation 6.17). The Cerenkov opening angle of the DIRC option was smeared by its estimated
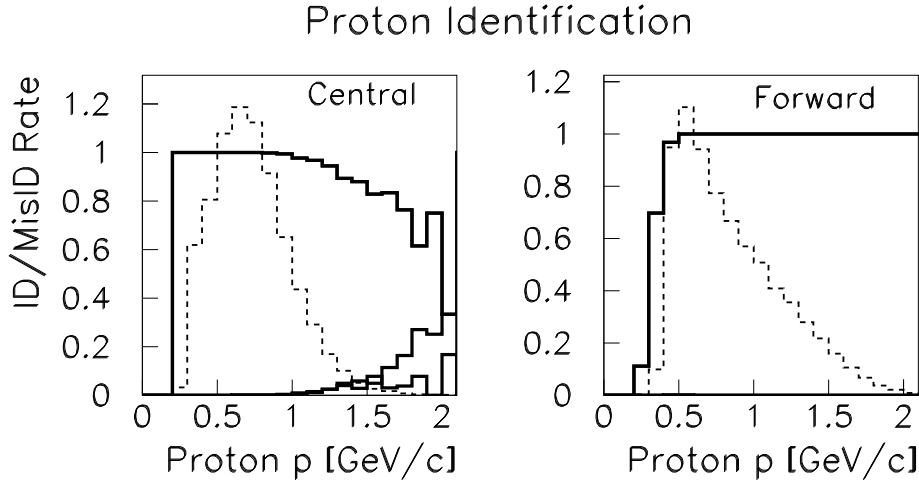
Proton Identification

Figure 6.82: The acceptance of proton tracks in the reaction $\gamma p \to K^* \bar{K}^* p$. The left plot shows central tracks and the right plot shows forward tracks. The top curve is the correct identification rate; the bottom is the misID rate. The starting momentum spectra for proton tracks in the central or forward regions are shown in the background.

resolution, 2.1 mrad. The particle separations in numbers of sigma versus momentum using these parameters were shown previously (figures 6.58 to 6.60).

Likelihoods were then calculated for each track at each detector and combined into total likelihoods according to the method described above. Particles were identified by rejecting hypotheses at the 90% confidence level, as prescribed in equation 6.24. A particle is called a pion if the kaon hypothesis is rejected and the pion hypothesis is not rejected:

$$R(K) > 2.7, \ R(\pi) < 2.7.$$

Similarly, a particle is identified as a kaon if:

$$R(\pi) > 2.7, \ R(K) < 2.7.$$

Finally, to find protons, both the pion and kaon hypotheses must be rejected, but the proton hypothesis is not rejected:

$$R(\pi) > 2.7, \ R(K) > 2.7, \ R(p) < 2.7.$$

This is perhaps the most basic algorithm possible for this situation. Certainly improvements could be made, such as incorporating strangeness conservation.

The results of this exercise can now be studied in several different pieces. Case 1(CDC) and case 2(CDC,BCAL) tracks are referred to as "central" (see figure 6.57); case 6(CKOV,TOF) and case 7(CDC,CKOV,TOF) tracks are "forward."

First consider proton identification. Figure 6.82 shows a nearly perfect proton identification rate for both the central region and the forward region; there is a drop in efficiency for central tracks above 1 GeV/c, but it has little effect on the overall identification rate. In addition, only a small fraction of tracks are misidentified.

Next, pion and kaon identification rates in the central region of the decector are shown in figure 6.83. Tracks less than 1 GeV/c are identified reliably; above that the efficiency drops to around 60%. Higher momentum central tracks are relying entirely on dE/dx information from the CDC in the relativistic rise region. With a dE/dx resolution of 10% this should be achievable
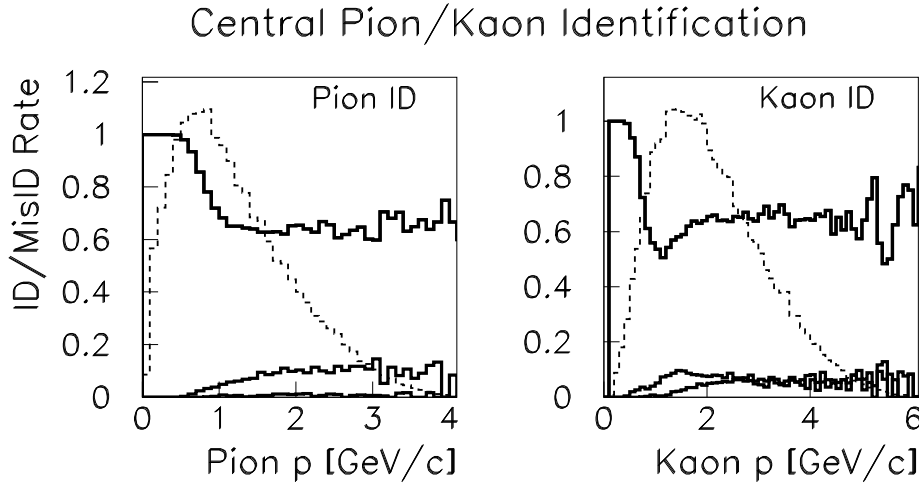
Figure 6.83: The acceptance of pions and kaons in the central region of the detector. The left plot is for pions; the right for kaons. The histograms in the background are the starting momentum spectra for pions and kaons in the central region. Each plot shows the identification and misidentification rates.

	π	K	p
Starting Number	50368	43665	62581
ID Rate	76.4%	64.0%	99.2%
MisID Rate	5.6%	10.1%	0.6%

Table 6.9: Particle identification in the central region for $\gamma p \rightarrow K^* \bar{K}^* p$ events. The statistics are for case 1(CDC) and case 2(CDC,BCAL) tracks. The starting number is the number of π, K, or p in the central region out of 100,000 total events generated.

at the 2 σ level (also see figure 6.59). Table 6.9 tabulates all the particle id results for central tracks.

Results for tracks in the forward region of the detctor are shown in figure 6.84. The top two plots use the gas Cerenkov option. Notice the drop in efficiency between 2 and 3 GeV/c where the momentum is too high for the TOF wall to be effective, but still not high enough to reliably measure photoelectrons from pions in the Cerenkov detector. The DIRC option solves this problem; its results are shown in the bottom two plots. Table 6.10 summarizes the efficiency numbers of forward tracks under the two different Cerenkov options. Finally, the central and forward cases are combined into overall pion and kaon identification rates in figure 6.85. The overall rates are tabulated in table 6.11.

	Gas Option			DIRC Option		
	π	K	p	π	K	p
Starting Number	38793	38789	30267	38793	38789	30267
ID Rate	94.4%	91.4%	99.1%	98.6%	90.3%	99.2%
MisID Rate	1.5%	4.8%	0.02%	0.3%	2.0%	0.8%

Table 6.10: Particle identification in the forward region for $\gamma p \rightarrow K^* \bar{K}^* p$ events. The statistics are for case 6(CKOV,TOF) and case 7(CDC,CKOV,TOF) tracks. The starting number is the number of π, K, or p in the forward region out of 100,000 total events generated.

Forward Pion/Kaon Identification
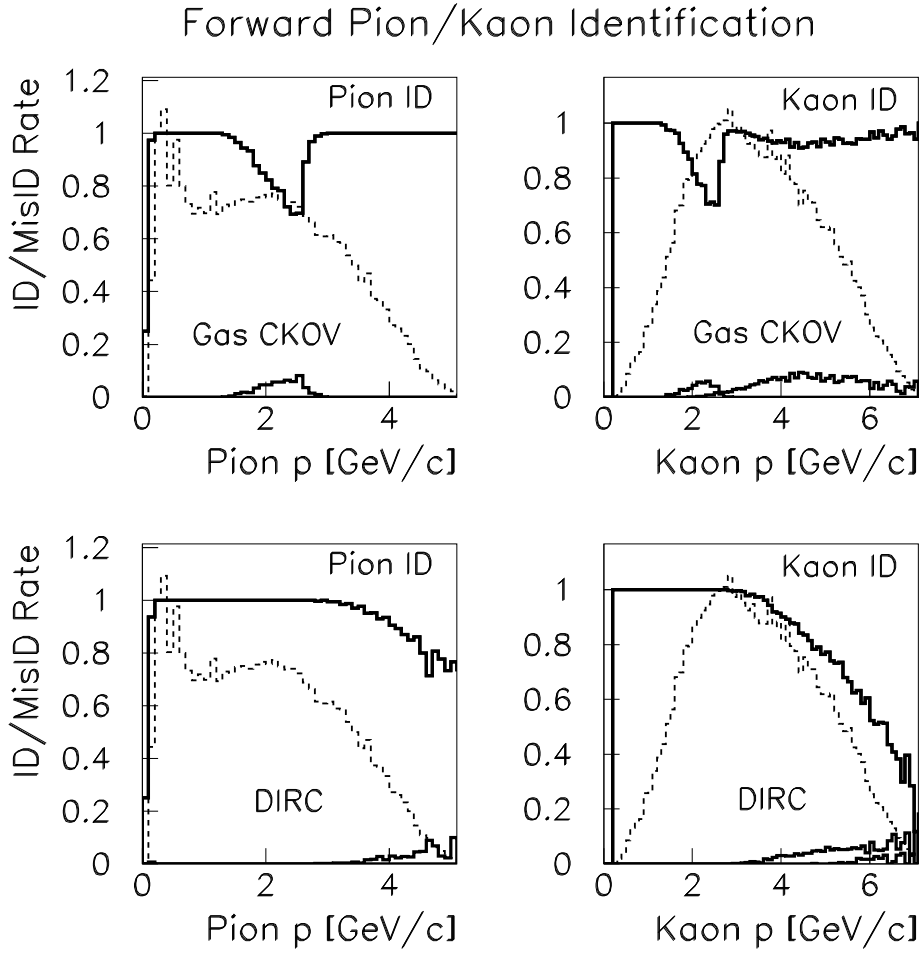
Figure 6.84: The acceptance of pions and kaons in the forward region of the detector. The top two plots are for the gas Cerenkov option; the bottom two are for the DIRC option. The left plots show pions; the right kaons. The histograms in the background are the starting momentum spectra for pions and kaons in the forward region. The curves in each plot represent the identification and misidentification rates.

	Gas Option			DIRC Option		
	π	K	p	π	K	p
Starting Number	100000	100000	100000	100000	100000	100000
ID Rate	80.4%	71.2%	94.3%	82.9%	71.9%	94.7%
MisID Rate	3.5%	6.8%	0.4%	2.9%	5.3%	0.8%

Table 6.11: Overall particle identification for the reaction $\gamma p \to K^* \bar{K}^* p$. The statistics are for all track cases.

It should be remembered that one of the crucial design parameters of the GLUEX experiment – in addition to, and perhaps more important than, the total efficiency numbers – is the uniformity of acceptances in the angles that will be used in Partial Wave Analyses. Efficiencies based on identification rates for the Gottfried-Jackson $\cos\theta$ angle of the $K^*\bar{K}^*$ system are shown in figure 6.86. This acceptance rises at $\cos\theta \approx \pm 1$ and falls at $\cos\theta \approx 0$ for the gas Cerenkov

Overall Pion/Kaon Identification
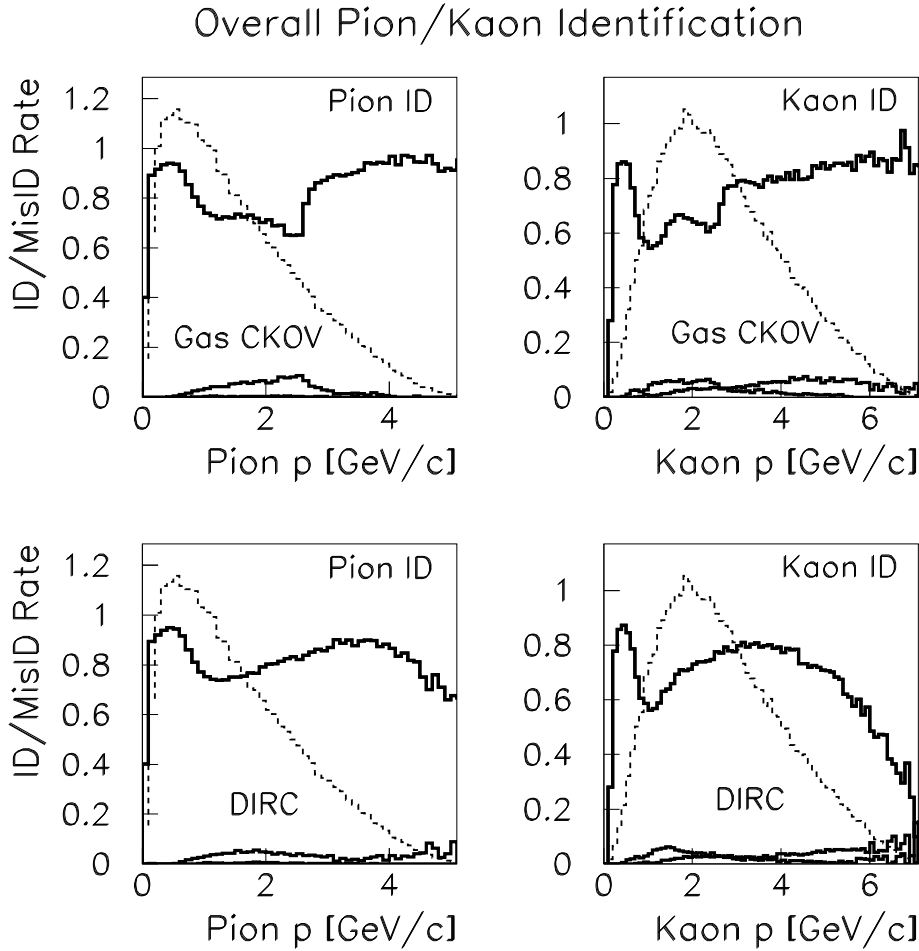
Figure 6.85: The overall acceptance of pions and kaons in all regions of the detector in the reaction $\gamma p \to K^* \bar{K}^* p$. The top two plots are for the gas Cerenkov option; the bottom two are for the DIRC option. The left plots show pions; the right kaons. The histograms in the background are the overall starting momentum spectra for pions and kaons. Each plot shows the identification and misidentification rates.

option for the following reason. When $\cos\theta$ is near its extremes, the final state particles are typically divided into high momentum (along the decaying resonance direction) and low momentum (against the decaying resonance direction) cases. The high momentum tracks are above pion threshold and are identified by the gas Cerenkov system; the low momentum tracks are effectively identified by the TOF wall. On the other hand, when $\cos\theta$ is near zero, final state tracks tend to fall in the momentum region where neither the TOF nor the gas Cerenkov is effective.

The DIRC option avoids this problem. Consequently, the $\cos\theta$ acceptance of the second plot of figure 6.86 is significantly more uniform.
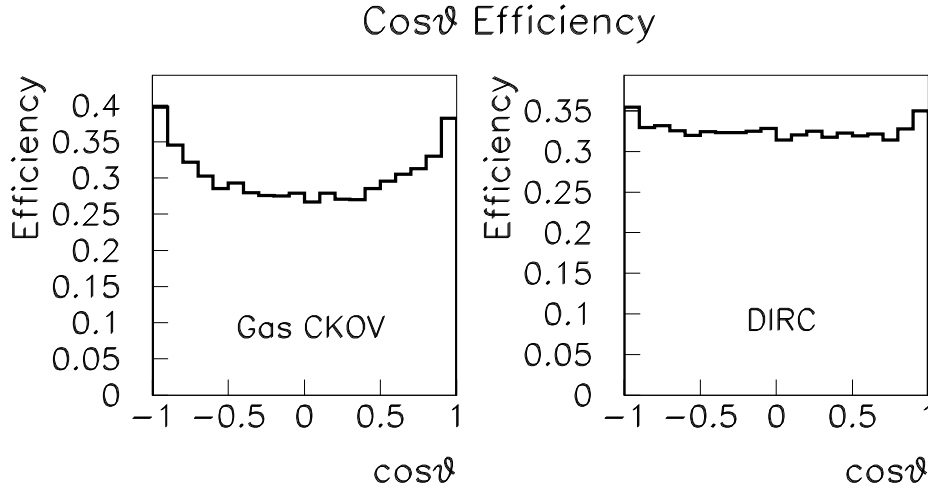
Figure 6.86: Angular efficiencies for $\cos\theta$ in the Gottfried-Jackson coordinate system for $\gamma p \rightarrow K^*\bar{K}^*p$ events. The left plot is for the Cerenkov option, the right for the DIRC option.

6.6 Detector Integration

The assembly and integration of each of the detector subsystems into the GLUEX detector requires careful coordination and attention to many diverse issues. The magnetic field configuration outside the magnet dictates the location and orientation of standard PMTs and/or use of high field devices such as HPMTs and SiPMs. The field distribution can be affected by magnetic materials used for support structures such as iron and, therefore, care must be taken in choosing common materials for the various support systems. The magnetic field in the vicinity of the Čerenkov counter is estimated to be approximately over 1 kG at the location of the readout devices and between 0.300 kG and 0.160 kG at the position of the PMTs for the forward LGD. The mounting and assembly of detectors must allow for the delivery of services required for their
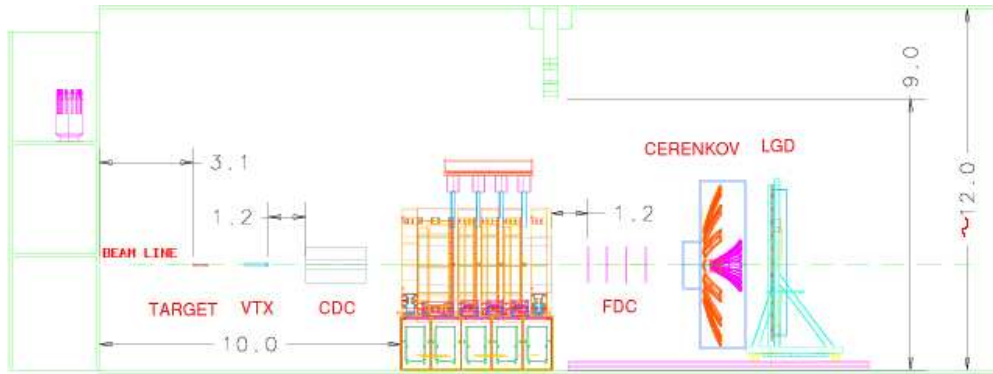
Figure 6.87: Exploded view of detector showing the detector subsystems in their extracted positions. The magnet does not move and detectors are inserted both from upstream and downstream into their nominal positions for normal operation.

operation, including cryogenics, cooling, electrical power, ventilation, gas connections, high voltage and signal and monitoring cables for all detectors. Moreover, access to each sub-system must be facilitated for purposes of maintenance or repair.

The detector sub-systems are shown in Figure 6.1 while the general layout of HALL D with all detectors extracted is shown in Figure 6.87. As the detector will need to be in its extracted position for both installation and servicing, it is important that its layout in the HALL D building accommodate access to the detector. Figure 6.88 shows a sketch of the detector in HALL D. The cryogenic connections to the solenoidal magnet are brought in from the north-west corner of the building, opposite the ramp used for truck access. This permits a large staging area in front of the door and minimal blocking of crane movement by the cryogenic lines. These lines can also be used to feed other cryogenic systems such as the liquid hydrogen target and potentially VLPCs used in the start counter. Gas lines from external mixing systems can also be run along this common path to minimize obstructions for crane and assembly operations.
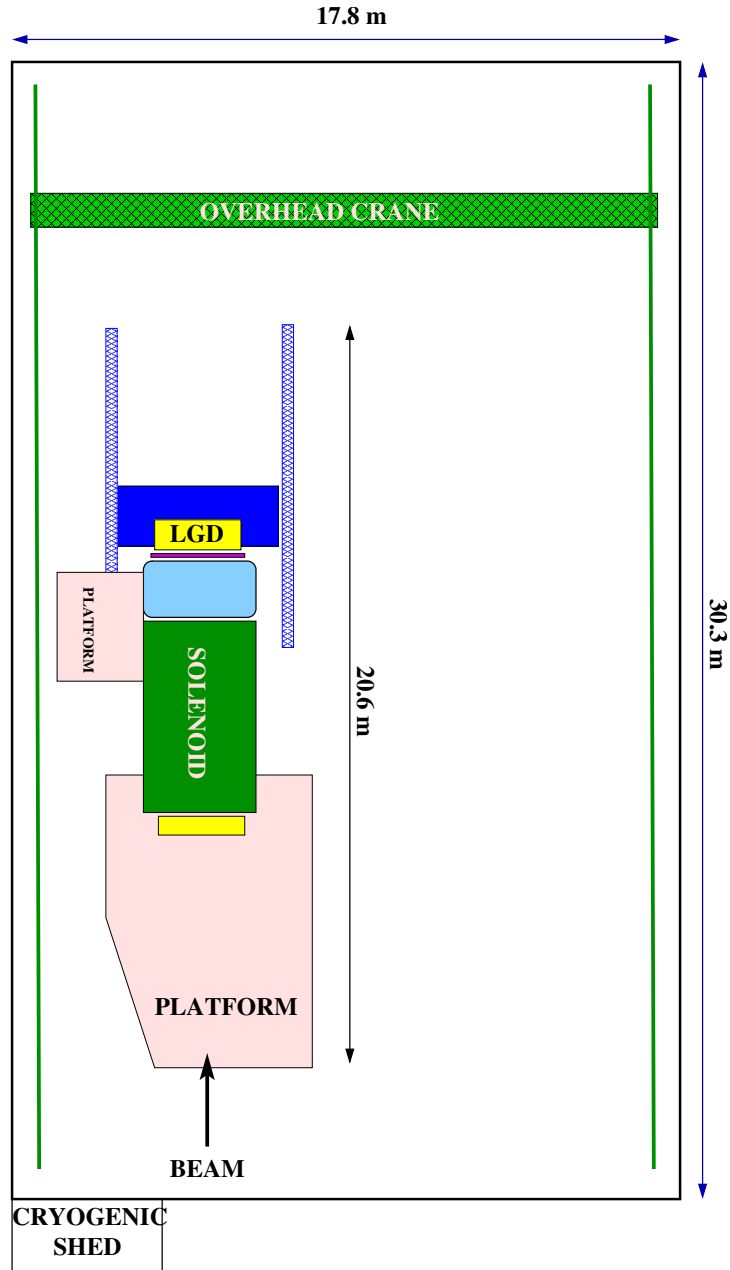
Figure 6.88: Plan view of the GLUEX experiment in HALL D.

Electrical power will be most likely delivered in trenches in the floor from breaker panels located on the north wall of the building. Clean power will be provided to detector electronics using isolation transformers as close to the detector as possible. As an example, the estimated power consumption of the forward calorimeter is 30 KW. All detector frames will be connected to the building ground network both for safety and to minimize electrical noise.

In terms of installation, most of the detector is fairly open and can be quickly accessed with minimal disruption of operations. However, the limited space inside the solenoidal magnet deserves special attention. This space contains the BCAL and its support structure, the Straw-tube Chamber, CDC, the Forward Drift Chambers, FDC, and the structures which both align and support these chambers as well as the mechanisms for extracting them. Finally, inside the CDC is space for the liquid hydrogen target, the beam pipe and the Start counter. Space allocation also needs to be made to assure that signals cables can be brought out from the detectors, while voltage and monitoring cables as well as gas, cryogenics and cooling lines can be brought to the appropriate detectors. Table 6.12 shows the radial space allocation inside the solenoid. The spaces labeled *keep out* are reserved for support, installation structures, signal and power cables, and other necessary services to the detectors such as gas and cooling.

Detector Name	r_{min}	r_{max}
Solenoid	$92.7\,cm$	
Keep Out	$90\,cm$	$92.7\,cm$
Barrel Calorimeter	$65\,cm$	$90\,cm$
Keep Out	$59\,cm$	$65\,cm$
Straw Tube Chamber	$13\,cm$	$59\,cm$
Forward Drift Chambers		$59\,cm$
Keep Out		$12\,cm$

Table 6.12: A radial space allocation map for the space inside the GLUEX solenoid.

6.6.1 Assembly and Mounting

As much of the GLUEX detector will need to be assembled in HALL D, the construction of the building is critical to any time line of the experiment. It is absolutely necessary that JLab do everything possible to guarantee early construction of this building. Once the building can be occupied, the assembly of the detector can begin. The first item will be the solenoidal magnet. It is transported in sections and will need to be re-assembled inside HALL D. It is also expected that both the BCAL and the LGD calorimeters will be assembled in HALL D. The assembled LGD will not fit through the door. It is also possible that parts of other detectors would be assembled in the HALL D building as well.

Of all the in-hall assemblies, the BCAL is likely to be another time line bottle neck. The time from start of construction until delivery at JLab is estimated at three years, but it is likely that the detector would arrive in several shipments spread out over the 3-year time frame. There are currently two possible assembly scenarios. The first follows what was done with the KLOE detector. This would have the BCAL being assembled inside the solenoid. The draw back to this plan is that the assembly of th BCAL cannot begin until the solenoid is fully installed. A second scenario would be to assemble the BCAL in a vertical orientation outside the solenoid, and then rotate it to horizontal and roll it into the solenoid as a single unit. This latter scenario both allows assembly to proceed in parallel with the solenoid and requires less service space between the outside of the BCAL and the inside of the solenoid. In both scenarios, the BCAL would be held in place with bolts that come through ring girders in the gaps between the magnet coils. These would connect to the 2.5 *cm* thick Aluminum backing plates on the BCAL modules as shown in Figure 6.89. In both installation scenarios, an assembly and installation jig will need to be designed and built. These options are currently under study by the engineering staff at JLab.
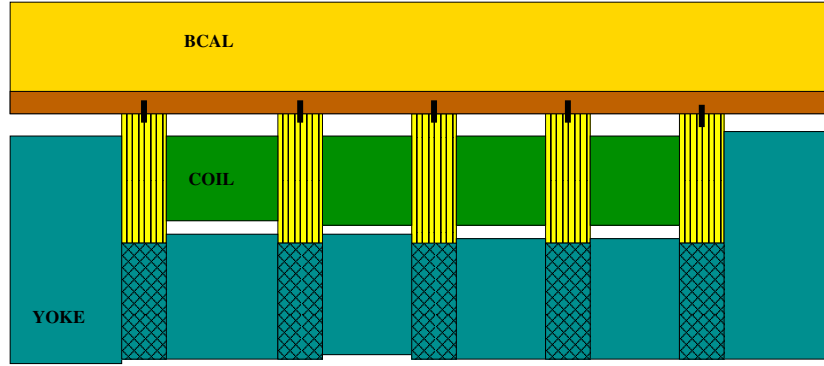
Figure 6.89: The Barrel Calorimeter bolted to the inside of the solenoid.

Once the BCAL has been mounted on the inside of the magnet, only the readout electronics will be accessible. Because of its design, it is anticipated that once it has been installed, it will not be removed. If for some reason it became crucial to replace a modules, a fairly extensive down time would need to be scheduled. However, given that there is nothing that can be serviced except for the readout electronics, such an event is considered highly unlikely over the lifetime of the experiment. Finally, to facilitate the installation of the tracking devices inside the solenoid, we anticipate placing a protective cover over the inner face of the BCAL. This will both protect the calorimeter and provide a surface to which the chamber supports can be mounted.

After the BCAL has been mounted in the solenoid, it will be necessary to install a pair of rails along the length of the detector. These rails will be used to support the CDC and FDC packages. Extensions can be added to allow for installation and extraction of the chambers. There is some possibility of the lead in the barrel calorimeter settling slightly over time. While we are currently investigating this, we also recognize that the rails will need to be fitted with bearings that have some play to prevent things from locking up due to small shifts in the *bed rock*. Both because of the difficulty of maintaining precision alignment between two rails over the 4 m length of the magnet and the possibility of settling in the BCAL, we anticipate no more than one precision rail, with the 2'nd rail being used for load bearing.

The CDC will be inserted from the up-stream end of the magnet, while FDC will be inserted from down-stream end. On the down-stream end, the Čerenkov, TOF and LGD detectors will be rolled back to make room for the FDC packages. One the up-stream end, the UPV will need to be put in place after the CDC has been installed. Then the START counter and target will be inserted into the CDC from the upstream end. They will be mounted on an independent cantilever system.

The Čerenkov counter and forward calorimeter will be mounted on independently movable support frames which can be moved in and out of their nominal location for access to the FDC. The TOF detectors will be mounted on the frame for the forward calorimeter. Each support structure will be self-contained, including electrical power and the appropriate readout electronics. Access platforms will be provided to allow easy access to the PMTs and readout electronics.

6.6.2 Survey and Alignment

In order to achieve the physics goals of the experiment, a system must be devised that can measure and maintain at least $100\,\mu m$ relative alignment of all of the tracking packages inserted into the magnet. The locations of the drift chamber wires relative to each other and the magnetic field are the most critical alignment tasks for the experiment. In addition, for ease of maintenance, the positions of the chambers should be either reproducible at that level, or a system needs to be established that can easily survey them into position at this accuracy. It will also be important to have an on-line monitoring system in place to dynamically correct for time dependent shifts in alignment. Such shifts might arise due to settling of the BCAL, thermal expansion and contracting of the chambers themselves, or accidental moving of the chambers when other detectors are being serviced. The collaboration is currently exploring the use of a system used by ATLAS for maintaining alignment.

As the CDC and FDC are inserted from opposite ends of the magnet, the mating and initial alignment are blind. The z positions of these chambers can be accurately registered at a single point by surveying in stops along the guide rail. We will also need a remote adjustment system that allows for correction of possible *pitch*, *roll* and *yaw* of the chamber packages.
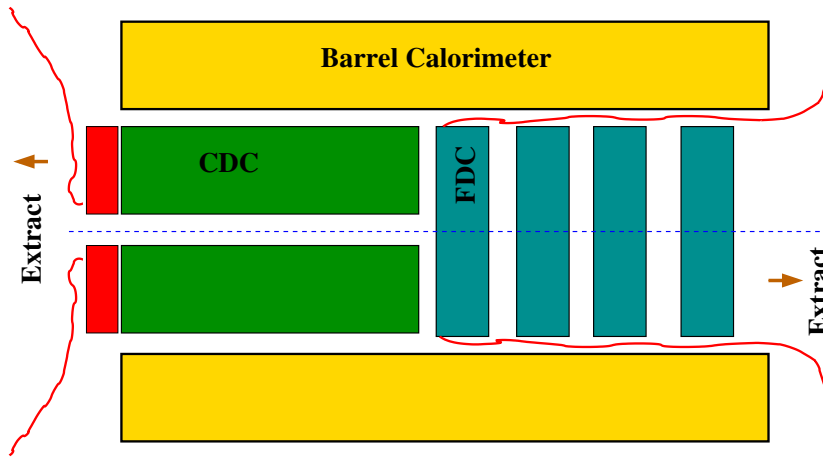
Figure 6.90: The insertion of the Central and Forward Tracking chambers inside the Barrel Calorimeter.

6.6.3 Access

Ease of access to the detector for maintenance ensures short commissioning and debugging times. Our goal is to allow maintenance of all detector components in less than one day. In order to maintain or check the upstream BCAL readout, the UPV will have to be removed and the service platform must be designed in a way to allow access to readout both above and below the horizontal scattering plane of the detector. To service the CDC, the UPV, the target and START detectors must be moved out of the way. All serviceable elements are located on the up-stream end of the CDC To access the FDC and/or the downstream BCAL readout, the Čerenkov and forward calorimeter must be moved on their rail systems, as shown in the exploded view in Figure 6.87. Service to the FDC is likely to be the most involved operation. Once the downstream detector packages are moved out of the way, a support structure will need to be craned in, and the chambers extracted from the solenoid.

The readout electronics for all the systems will be accessible without having to move any detector component. The PMTs for the Čerenkov, TOF and LGD will be accessible by at most moving the forward calorimeter carriage. Access to the LGD enclosure will in principle be easy, but radiation levels must be measured and deemed to be at a safe level prior to any access.
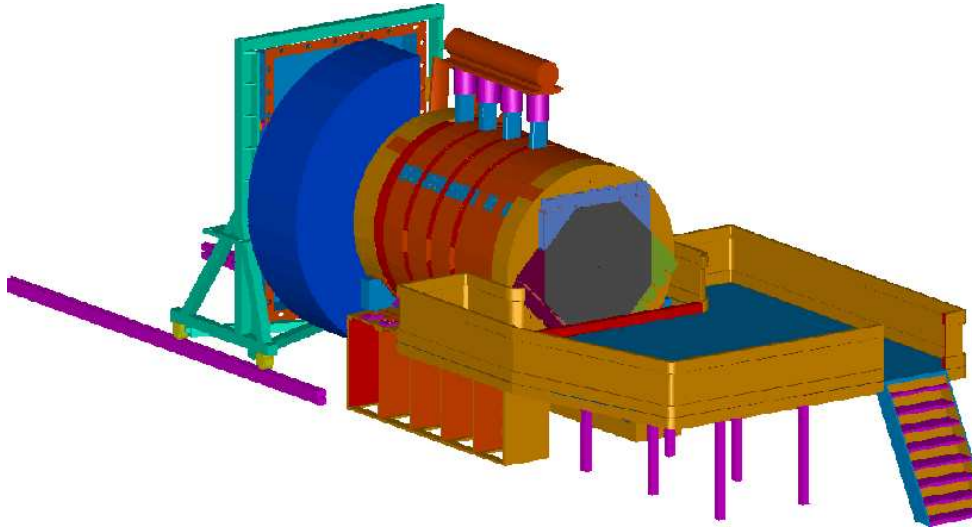
Figure 6.91: Detector and upstream platform for service of the inner detector packages.

6.6.4 Interaction Between Subsystems

The detectors in the forward direction (Čerenkov, TOF and LGD) are relatively isolated mechanically and operate independently of other systems. The detectors inside the magnet, however, are in close proximity and mounted on the same mechanical frames that are anchored on the BCAL and/or the solenoid. Therefore, cabling, power consumption, and access for maintenance must be coordinated carefully.

6.6.5 Cabling

All detector electronics will be located near the detector itself. This will minimize cable lengths and eliminate the need for large cable runs from the detector to electronic racks far from the detector. The racks of electronics servicing the inner detectors will be located on a platform upstream of the magnet with ample space for access. A possible *Access Platform* is shown in Fig.6.91 with the primary aim being that detectors can be operated both inside and outside the solenoid without making any disconnections. This implies that either the cabling for START detector, CDC and FDC will have enough slack so that they can be moved in or out of the magnet without any disconnections, or that the electronics will themselves move along with the detector elements. It is crucial that the detectors can be operated in the extracted position for testing and the installed position during normal operation without wiring changes.

List of Figures

List of Tables

Bibliography

[1] A. Brunner *et al.* A Cockcroft-Walton base for the FEU84-3 photomultiplier tube. *Nuclear Inst. and Meth.*, A**414**:446, 1998.

[2] B. B. Brabson *et al.* A study of two prototype lead glass electromagnetic calorimeters. *Nuclear Inst. and Meth.*, A**332**:419–443, 1993.

[3] R. R. Crittenden *et al.* A 3000 element lead-glass calorimeter. *Nuclear Inst. and Meth.*, A**387**:377–394, 1997.

[4] R. Jones *et al.* The Radphi detector. *submitted to Nucl. Instrum. Meth.*, 2004.

[5] C. P. Steffen. PhD thesis, Indiana University, 2001.

[6] J. Gunter. An analysis of the reaction $\pi^- p \rightarrow \pi^0 \pi^0 n$ at 18 GeV/c. Ph. D. Thesis - Indiana University, 1997.

[7] J. Gunter *et al.* A partial wave analysis of the $\pi^0 \pi^0$ system produced in $\pi^- p$ charge exchange collisions. *Phys. Rev.*, D**64**:072003, 2001. hep-ex/0001038.

[8] R. Lindenbusch. *An analysis of the reaction $\pi^- p \rightarrow \eta \pi^0 n$ at 18 GeV/c*. PhD thesis, Indiana University, 1997.

[9] M. Swat. *Analysis of the $\eta \pi$ system*. PhD thesis, Indiana University, 2003.

[10] A.R. Dzierba *et al.* A study of the $\eta \pi^0$ sprectrum and search for a $J^{PC} = 1^{-+}$ exotic meson. *Phys. Rev.*, D**67**, 2003. hep-ex/0304002.

[11] S. Teige *et. al. Phys. Rev.*, D**59**:012001, 1999.

[12] J. Manak *et. al. Phys. Rev.*, D**62**:012003, 2000.

[13] P. Eugenio *et. al. Phys. Lett.*, B**497**:190, 2001.

[14] M. Nozer *et. al. Phys. Lett.*, B**541**:35, 2002.

[15] J. Kuhn *et. al. Phys. Lett.*, B**595**:109, 2004.

[16] R. Fruhwirth et al. *Data Analysis Techniques for High-Energy Physics*. Cambridge University Press, 2000.

[17] R. Wingman. *International Series of Monographs on Physics*, volume 107. Oxford University Press, 2000.

[18] R. T. Jones and M. Kornicer. LGD Shower resolution. Technical report, 2003.

[19] Graham McNicoll. A study of photon sensitivity in the Hall D detector. Technical Report GlueX-doc-**36**, Carnegie Mellon University, 2000. `http://portal.gluex.org/`.

[20] Joachim Kuhn and Curtis A. Meyer. Acceptance Study for the GlueX detector system. Technical Report GlueX-doc-**264**, 2004. `http://portal.gluex.org/`.

[21] C. A. Meyer. A study of timing resolutions on particle identification in the HALL Ddectector at jefferson lab. Technical Report GlueX-doc-**14**, Carnegie Mellon University, 1999. http://portal.gluex.org/.

[22] C. A. Meyer and P. Eugenio. A Study of Compined $K-\pi$ Separation using Time–of–Flight Counters and a Gas Čerenkov Detector. Technical Report GlueX-doc-**15**, Carnegie Mellon University, 1998. http://portal.gluex.org/.

[23] The GlueX Collaboration. Hall D Design Report, Version 4. Technical Report GlueX-doc-**58**, 2002. http://portal.gluex.org/.

[24] D.W. Hertzog *et al. Nuclear Inst. and Meth.*, A**294**:446, 1990.

[25] A. Antonelli *et al. Nuclear Inst. and Meth.*, A**370**:367, 1996.

[26] M. Adinolfi *et al. Nuclear Inst. and Meth.*, A**494**:326, 2002.

[27] Brian Klein *et. al.* B-CAL Progress and Construction Report. Technical Report GlueX Technical Note **333**, 2004. http://portal.gluex.org/.

[28] Brian Klein *et. al.* B-CAL Progress and Construction Report. Technical Report GlueX Technical Note **333**, 2004. http://portal.gluex.org/.

[29] Z. Papandreou, E.J. Brash, G.M. Huber, V.D. Kovaltchouk, S. Li, G.J. Lolos, L. Snook and S. Vidakovic. Attenuation Length and Timing Resolution of Scintillating Fibers for Hall D. Technical Report GlueX-doc-**50**, University of Regina, October 2001. http://portal.gluex.org/.

[30] A. Antonelli *et al. Nuclear Inst. and Meth.*, A**354**:352, 1995.

[31] B. Jasper and R. Filby. Degradation of Fibers with UV Exposure and Construction Aspects of the 4m Calorimeter Module. Technical Report GlueX-doc-**331**, University of Regina, April 2004. http://portal.gluex.org/.

[32] B. Dolgoshein. *Nuclear Inst. and Meth.*, **494**:48, 2003.

[33] D. Renker. Avalanche photodiodies now and possible developments. In *Vienna Conference on Instrumentation*, 2004. February 16-21 2004, conference web site: http://vci.oeaw.ac.at/.

[34] V. Saliev. Private Communication.

[35] T. Okusawa. *Nuclear Inst. and Meth.*, **459**:440, 2001.

[36] P. Eugenio. *Genr8*: A general monte carlo event generator. Technical report, Carnegie Mellon University, 1998.

[37] D. Aston *et al.* The LASS spectrometer. Technical Report SLAC-Report-298, 1987. Copies available from the SLAC publications office, at http://www.slac.stanford.edu/pubs/.

[38] C. A. Meyer. Tracking Resolution Requirements in the Meson Spectroscopy Facility at Jefferson Lab. Technical Report GlueX-doc-**7**, Carnegie Mellon University, 1998. http://portal.gluex.org/.

[39] Rob Veenhof. *The GARFIELD Program, Simulation of Gaseous Detectors*. CERN, 1984. http://garfield.web.cern.ch/garfield/.

[40] H. Wirth. Particle Identification with the JETSET Straw Chambers. *Nuclear Inst. and Meth.*, A**367**:248–251, 1995. Prepared for 7th International Wire Chamber Conference (WCC 95): Recent Trends and Alternative Techniques, Vienna, Austria, 13-17 Feb 1995.

[41] Zebulun Krahn and Mike Williams. Gas Composition Study for the Straw Tube Chamber in the GlueX Detector at Jefferson Lab. Technical Report GlueX-doc-**62**, 2003. `http://portal.gluex.org/`.

[42] D. Barton, *et al.* (The EVA Collaboration). Color Transparency with EVA, October 1994. BNL-PROPOSAL-850.

[43] Mike Williams, Zebulun Krahn and Curtis A. Meyer. A Study of the Straw Tube Detector for the GlueX Detector at Jefferson Lab. Technical Report GlueX-doc-**54**, Carnegie Mellon University, July 2002. `http://portal.gluex.org/`.

[44] Curtis A. Meyer. Accuracy Measurements of the straw-tube chamber end plates. Technical Report GlueX-doc-**61**, 2003. `http://portal.gluex.org/`.

[45] Curtis A. Meyer and Zebulan Krahn. A Summary of Straw-tube Chamber Tests. Technical Report GlueX-doc-**280**, 2004. `http://portal.gluex.org/`.

[46] H. Fenker *et al. Nuclear Inst. and Meth.*, A**367**:285, 1999.

[47] *ATLAS Collaboration.* ATLAS Technical Design Report, Chapter 6, June 1997.

[48] *PHENIX Collaboration.* PHENIX Internal Note PN125.

[49] D. Aston *et al. (The LASS Collaboration).* SLAC Internal Note SLAC-298.

[50] A. Antonelli *et al.* A Pb SciFi EM calorimeter for an experiment on CP violation at DAPHNE. Technical Report LNF-91-073-P, Frascati, 1991.

[51] S. Denisov *et al.* Timing charactersitics of scintillation counters. *Nuclear Inst. and Meth.*, A**478**:440–443, 2002.

[52] S. Denisov *et. al.* Characteristics of the TOF Counters for the GlueX Experiment. *Nuclear Inst. and Meth.*, A**494**:495–499, 2002.

[53] S. Denisov *et al.* Systematic studies of timing characteristics for 2-m long scintillation counters. *Nuclear Inst. and Meth.*, A**525**:183, 2004.

[54] S. Denisov *et al.* Studies of magnetic shielding for phototubes. *Nuclear Inst. and Meth.*, article in press, 2004.

[55] I. Adam *et al.* The DIRC Particle Identification System for the BaBar Experiment. 2004. accepted for publication.

[56] P. Coyle *et al. Nuclear Inst. and Meth.*, A**343**, 1994.

[57] B. Ratcliff. Technical report, 1992 and 1993. SLAC-PUB-5946 and SLAC-PUB-6047.

[58] B. Aubert *et al.* Observation of Direct CP Violation in $B^0 \rightarrow K^+\pi^-$ Decays. 2004. hep-ex/0407057.

[59] B. Aubert *et al.* The BABAR Detector. *Nuclear Inst. and Meth.*, A**479**, 2002.

[60] *Status of the PEP-II B Factory.* talk given at the 14th Advanced ICFA Beam Dynamics Workshop: Beam Dynamics Issues for e^+e^- Factories " (ICFA 97), Frascati, Italy, 1997.

[61] E. Bloom *et al.* The PEP-II Asymmetric B Factory:Design Details and R&D Results. Technical Report SLAC-PUB-6564, 1994.

[62] E. Bloom *et al.* PEP-II: An Asymmetric B Factory. Conceptual Design Report. Technical Report SLAC-R-418, 1993.

[63] The BABAR Collaboration. The BABAR Physics Book. Technical Report SLAC Report 504, 1998.

[64] The provider of fused silica: TSL Group PCL,
P.O. Box 6, Wallsend, Tyne & Wear, NE28 6DG, England.
Quartz Products Co., 1600 W. Lee St., Louisville, Kentucky 40201.
Manufacturer of quartz bars: Boeing, Rockedyne Division, 2511 C Broadbent Parkway NE, Albuquerque, New Mexico 87107.

[65] Manufacturer of photo-tubes: Electron Tubes Limited, (formerly: Thorn EMI Electron Tubes), Bury Street, Ruislip, Middlesex HA47TA, U.K.

[66] J. Cohen-Tanugi *et al. Nuclear Inst. and Meth.*, A**515**, 2003.

[67] R. Brun *et al.*, 1986. GEANT3, CERN-DD/EE/84-1.

[68] TOSCA 3D, software for electromagnetic design, Vector Fields Inc., Aurora, Il 60505, USA.

[69] M. Sivertz *et al.* A compact gas Čerenkov detector with novel optics. *Nuclear Inst. and Meth.*, A**385**:37, 1997. hep-ex/9607013.